Bacteriorhodopsin-based assemblies and their enhanced photoelectric and bioelectric properties

Li, Rui

2010

BACTERIORHODOPSIN-BASED ASSEMBLIES AND THEIR ENHANCED PHOTOELECTRIC AND BIOELECTRIC PROPERTIES

LI RUI

School of Chemical and Biomedical Engineering

A thesis submitted to the Nanyang Technological University
in partial fulfillment of the requirement for the degree of
Doctor of Philosophy

2010

Acknowledgement

First, and foremost, I would like to express my sincere gratitude to my supervisor, Professor Li Chang Ming. His strong enthusiasm for academic research, great curiosity in science, combined with a general amount of patience, and enormous encouragement, have been always a source of inspiration, throughout my graduate career in the School of Chemical and Biomedical Engineering in Nanyang Technological University. Professor Li never hesitates to impart his professional knowledge and expertise all the way through my work from not only general research directions but also technical details, especially in times of difficulties. Without his guidance and motivations, it would not be possible for me to overcome the setbacks and obstacles encountered all through the time. The four-year academic experience with Professor Li is my life treasure which will continue motivating me to face scientific challenges in the future.

I am grateful to my co-supervisor, Prof. Chen Peng for his valuable suggestions and inspiring discussions.

All past and present members of Professor Li's group have provided immeasurable support for my work. Many acknowledgements are extended to these great people and friends, especially those who collaborated with me, thank you very much for your stimulating discussion, fruitful collaboration and warm-hearted friendship.

Finally, this dissertation would not have been fulfilled without contribution from my family. I would like to express my sincere appreciation to my parents, who have been always standing by me despite understanding little of what I do. They have instilled in me since my childhood the importance of pulling out all stops at whatever I do. Without their unconditional love, support and dedication, I would never be the person that I am today. I will never be able to repay them. I would also thank both my sisters for their efforts on taking care of my old parents while I am not around. I could never thank my beloved husband enough for always being there for me when I need him. The dissertation is for them.

Table of contents

List of figures

List of tables

Summary

During three decades of research since its discovery, bacteriorhodopsin (bR) has become one of the most attractive biomaterials with great potentials for various bioelectronic applications. However, further improvement of its photoelectric and bioelectric properties for practical applications still remains a great challenge. This PhD research project investigates novel bR-based assemblies, constructed with functional materials including nanomaterials and polymers, to obtain enhanced photoelectric and bioelectric properties for potential bioelectronic applications and explore the fundamental insights in bioelectronics.

A poly-L-lysine (PLL)/bR-embedded purple membrane (bR-PM) multilayer film was fabricated by the layer-by-layer (LbL) assembly technique. It was the first time to use PLL as the assembler in LbL construction of bR-based film. Various methods were employed to investigate the multilayer construction process and the photocurrent generated from the PLL/bR-PM film, showing that PLL is a better assembler in bR-based LbL assembly for enhanced photoelectric performance in comparison to other polycations utilized as assemblers previously. The enhancement mechanism was proposed.

Integration of a bR film with a multilayered $WO_3 \cdot H_2O$ nanocrystals/polyvinyl alcohol (PVA) membrane was used to improve the photoelectric response of bR. The photocurrent was significantly augmented with

the WO$_3$•H$_2$O/PVA membrane by about six fold than bR alone. The mechanism for enhancement of the photoelectric response is very likely to be the spillover effect of WO$_3$•H$_2$O nanoparticles that build a stronger local electric field.

The photocurrent of bR was changed from capacitive to stationary pattern for the first time by construction of a hybrid bR/quantum dot (QD) bionanocomposite. QDs in the bionanocomposite were discovered as nanoscaled light sources embedded in the hybrid system to create a modified photocycle for bR to generate the unusual stationary photocurrent. This study opens a new horizon to employ bR bioelectronic properties for a possible bio solar cell application.

The bio-originated dipole moment in bR was discovered to play an indispensible role in bidirectional mediation of the electric transport in the bottom-contact TiO$_2$ nanowires field effect transistor (FET) to significantly improve the hole mobility by a factor of 2. The normalized ΔI_D was shown to decrease as the layer number of bR-PM modified on the FET increased, suggesting the mediation of the additional electric field generated by the dipole moment in bR-PM actually boosts the performance of the TiO$_2$ nanowires FET.

In a brief, this research project provides various engineering approaches to improve the bR bioelectronic performance as well as investigates the mechanisms to explore their scientific insights. The successful construction of a number of novel bR-based assemblies demonstrates that smart bR biofilms can

be created by proper incorporation of functional polymers and/or nanomaterials to obtain enhanced photoelectric and bioelectric properties for various bR bioelectronic applications. The mechanisms proposed for improved properties of different bR-based biofilms also fundamentally reveal the interactions between biomolecules and other materials.

Chapter 1 Introduction

As a fast blooming research area with a focus on the construction of functional devices integrated by biomolecules and electronic elements (1), bioelectronics has advanced to the frontiers of biology, chemistry, physics, electronics and material science (2). In bioelectronics, various biological elements involve enzymes (3-4), receptors (5-6), antibodies or antigens (6-9), oligonucleotides or DNA fragments (7-8), some cofactors (molecules with low molecular weight and high affinity to biomaterials) such as $NAD(P)^+$ (9), biotin (10), etc., while the broad range of electronic elements used include electrodes (11-14), field-effect transistors (15-16), piezoelectric crystal (17-20), and others (21-26). As shown in Figure 1-1, the bidirectional interactions of biomaterials and electronic elements can lead to a variety of important applications.

In nature, many different biological processes are activated by light signals. The representative light-controlled biological mechanisms are photosynthesis (27-28) and vision (29-30). Other important light-triggered processes include: i) photomovement at different biological levels (31), such as, development of plant tissues, motion of motile organisms; ii) photomorphogenesis (32-33), such as, seed germination, flowering induction and chlorophyll synthesis; and iii) conversion of light energy into chemical energy (34-35), such as, ATP synthesis, ion-transport, and proton pumps. The common characteristic of all these systems is the involvement of a chromophore, which acts as a photosensor

or photoreceptor to trigger sequential chemical transformations upon photon absorption in the membrane or protein surrounding the chromophore (36).
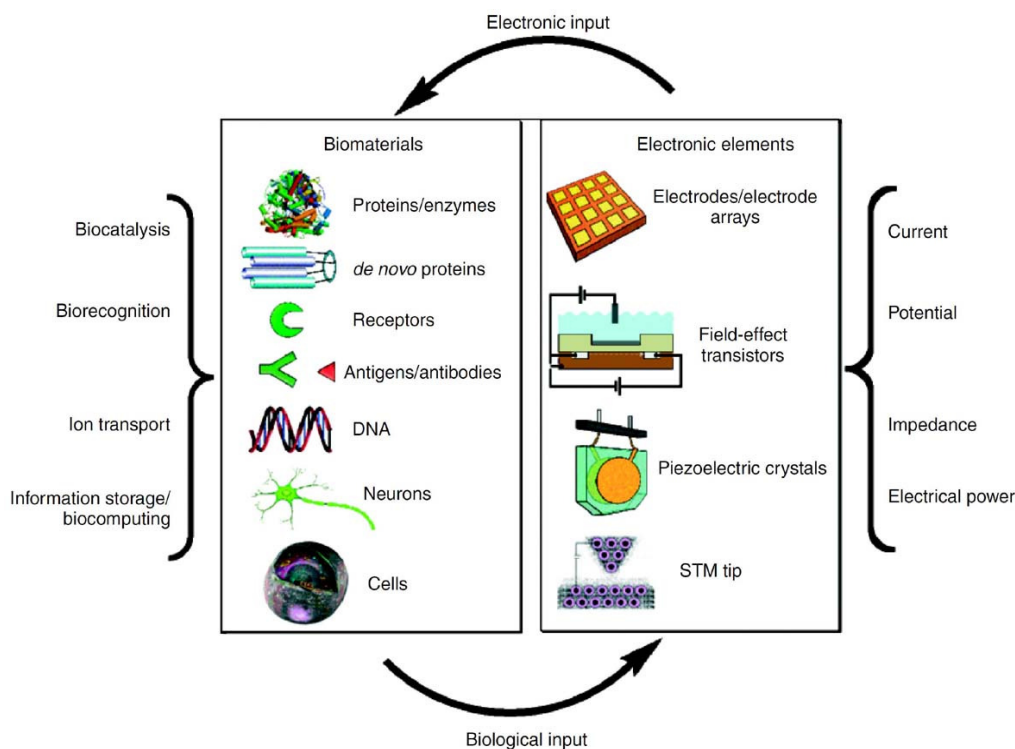
Figure 1-1 Integrated systems of biomaterials and electronic elements for bioelectronic applications (1).

Bacteriorhodopsin (bR), a retinal-containing protein in *Halobacterium halobium,* is a representative biomaterial containing chromophore (37). The 11-*trans*-retinal chromophore of bR is embedded in the cell membrane of the bacterium, and upon absorption of photons it starts to pump protons from the cytoplasmic (CP) to the extracellular (EC) side of the membrane, resulting in a potential gradient to activate the membrane-bound ATPase for ATP synthesis and thus converting light energy into chemical energy *in vivo*; moreover, the potential gradient arisen from the proton pumping can be converted into electric energy as a type of capacitive photocurrent *in vitro*. Due to its capability of

converting light energy into electric energy *in vitro* and the inherent dipole moment, bR plays important role in not only photoelectrics, but also bioelectrics, which are two important research areas in bioelectronics.

1.2 Motivations

Although bR has become one of the most attractive biomaterials for bioelectronic applications over the past thirty years, there still exists a gap between the viable bR applications and its photoelectric and bioelectric properties. Particularly, although its optical sensing application has aroused much interest, both the small amplitude and the monotonous pattern of bR photoelectric response greatly limit us to fabricate practical devices. Therefore this PhD project is mainly motivated by exploring solutions to significantly improve bR photoelectric performance or to use bR unique bioelectric properties to enhance the performance of some electronic device.

To generate *in vitro* photoelectric current, the immobilization of bR on a solid substrate is essential because both the orientation to favor the proton pumping and the contact to render good electric transport between the substrate and bR can affect its photoelectric response greatly. Layer-by-layer (LbL) has been employed to immobilize bR previously but the output photoelectric signals still do not satisfy the requirement from the practical applications with polycations that used as assemblers previously. Accordingly, there is a great

need to utilize a novel polycationic assembler that could enhance the photoelectric responses for the bR LbL assembly.

Besides the improvement in bR immobilization technique, composing functional components with bR may be efficient approach to ameliorate bR properties. Protein bR and its inherent dipole moment are of nanometric sizes, comparable to the dimension of nanoparticles or nanowires. Since nanomaterials are known to possess unique optical and electronic properties, to compose some specific nanostructured materials with bR may possibly result in positive impact on bR bioelectronic responses.

Investigation of the enhancement mechanisms in different bR-based bioelectronic assemblies is very important. Understanding of the mechanisms can not only direct the future efforts in further improvement of bR photoelectric and bioelectric properties for broad practical applications, but also enrich the fundamental knowledge and scientific insights into bioelectronics.

1.3 Objectives

The objective of this research is to investigate bR-based assemblies and their unique bioelectronic properties for possible applications. Particularly, the project focuses on using a novel assembler to LbL construct bR-based multilayer film for improved photoelectric performance, integrating a unique nanostructured film to boost bR proton pumping capability, composing

bionanocomposite to change bR photoelectric response pattern, utilizing dipole in bR to modify nanomaterial for an enhanced electronic device performance, and exploring the enhancement mechanisms of the bR bioelectronic properties in different composed systems.

1.3.1 To Apply Unique Functional Assembler to LbL Construct bR-Based Film for Improved Photoelectric Performance

To boost the bR photoelectric performance, LbL assembly technique is applied to construct bR-based multilayer film, in which a good assembler is very critical. Up to date, the assemblers used to construct bR-based films have improved the bR bioelectric responses, but new assembler needs to be explored for more efficient loading capability of bR in the film for further performance improvement. Thus the biocompatible polycation poly-L-lysine (PLL) is employed as the assembler in this work and the photoelectric performance of the bR-based assembly is investigated.

1.3.2 To Fabricate Different bR-Nanomaterial Assemblies for Enhancement of the Bioelectronic Performance

One important task in this project is to utilize functional nanostructured material to improve the photoelectric and bioelectric properties of bR-based assemblies. Various inorganic nanomaterials are known to have unique physicochemical properties resulted from their small sizes and unique

nanostructures. By proper composing or assembling technique, specific nanomaterials are used to integrate with bR for significant improvement of the bioelectronic properties. Regarding this concern, $WO_3 \bullet H_2O$ nanocrystals, CdTe quantum dots (QDs) and TiO_2 nanowires are used to construct bR-based assemblies and their bioelectronic properties are investigated.

1.3.3 To Study the Bioelectronic Enhancement Mechanisms of bR-Based Assemblies

To ultimately fulfill viable bioelectronic applications of bR, it is important to explore the mechanisms for enhancement in various bR-based assemblies, which can provide scientific insights of bR role in bioelectronics while guide the future works in important bR applications.

1.4. Organization

This dissertation investigates the improvement of photoelectric and bioelectric properties of novel bR-based assemblies and the mechanisms of the performance enhancement. Chapter 1 introduces the topic and provides an overview of the motivation and objective of this PhD research. Chapter 2 reviews the research pertinent to the bioelectronic properties of bR, including its unique structure, biological function, bioelectronic applications and the proposed mechanisms. Chapter 3 describes the experimental approaches, materials, and instruments used in this study in detail. Chapter 4 presents the

LbL fabrication of bR multilayer film using PLL as novel assembler and the improved photoelectric response. Chapter 5 introduces a unique integrated bR/WO$_3 \cdot$H$_2$O nanocrystals/poly vinyl alcohol (PVA) membrane and the enhanced photoelectric performances. Chapter 6 discusses the novel hybrid bR/QDs bionanosystem and the generation of the unusual stationary photocurrent. Chapter 7 describes the bidirectional mediation by the dipole in bR on the performance of TiO$_2$ nanowires FET. Finally, Chapter 8 provides a general conclusion and proposes some perspectives on possible future research.

Chapter 2 Literature Review

2.1 Overview of bR

bR was first discovered by Oesterhelt and Stoeckenius over three decades ago (38) in the plasma membrane of *Halobacterium salinarum* (*H. salinarum*, formerly termed *Halobacterium halobium* and *Halobacterium salinarium*). *H. salinarum* is actually not a bacterium but rather a model organism for the halophilic branch of the Domain Archaea. Breeding halobacteria such as *H. salinarum* are responsible for the intense purple color of the saltern basin (37) shown in Figure 2-1.

Figure 2-1 Salt lakes in Australia appear purple due to the presence of numerous halobacteria (39).

H. salinarum flourish in salterns and salt lakes exposed to bright sunlight, in which the concentration of NaCl can be as high as 5 M, more than 8 times that of seawater (~ 0.6 M) (40), while the oxygen tension is rather low. Over millions of years, *H. salinarum* have adapted to this "autosterile" environmental niche in which almost no other species can survive. The fresh seawater occasionally propelled into salterns brings organic substances with relatively low salt concentrations that are used as sources for nourishment and propagation by *H. salinarum* living under oxidative conditions. Once the limited supply of oxygen is exhausted, *H. salinarum* must depend on the alternative mechanism of phototrophy, which it developed while surviving in specific living conditions during its evolution to utilize sunlight as an energy source. In the photosynthetic capability of *H. salinarum*, bR plays a key role.

2.2 Structure and Biological Function of bR

2.2.1 Comparison of bR and Rhodopsin

Oesterhelt and Stoeckenius named the purple protein that they discovered in halobacteria bR because it contains the chromophore retinal, which is also found in rhodopsin (Rh), the visual pigment in retinal rod cells from eukaryotes (41).

Findlay's research (42) into the structure of the polypeptide chains in both bR and Rh led to the discovery that each molecule consists of seven transmembrane α-helices. A Schiff base is utilized to connect covalently with the retinal through a lysine residue located approximately in the center of the seventh helix. In addition, for both molecules, regarding the CP interior, the amino-terminus is outside as the carboxy-terminus inside. Lanyi et al.'s research (43) into aligning and superimposing the stereo conformational structure further confirmed that bR and Rh molecules share similar folding pattern in the transmembrane region.

Whereas these resemblances in bR and Rh topography are unassailable, further research has revealed that even though bR and Rh were once closely related, they have diverged greatly during their evolution. Indeed, from structure to function, there are substantial differences between these two seemingly alike molecules. First, regarding overall polypeptide length, bR is composed of 248 residues while Rh is composed of 348 residues (42). Second, investigation of retinal conformation has revealed that when it is light adapted, bR holds all-*trans* retinal, which is later isomerized to 13-*cis* retinal during its photocycle. In contrast, the dark-adapted 11-*cis* retinal form in Rh is converted to all-*trans* retinal once exposed to light. Furthermore, bR is rather simple in function, acting as a light-driven proton pump (44), while Rh, a member of the G-protein coupled receptor family, is responsible for both the formation of the photoreceptor cells and the first events in the perception of light (29, 45). Thus,

whereas Rh is only one among several necessary components needed to perform a particular physiological function, bR can perform a similar physiological function independently.

2.2.2 Structure and Properties of bR at Ground State

bR is the only protein component in the plasma membrane of the *H. salinarum*. Lipids and bR at a molar ratio of approximately 10:1 together constitute patches known as *purple membrane* (PM), which occupy up to 80% of the cell surface of the *H. salinarum* (46). Corresponding to this molar ratio, bR comprises 75% of the mass of PM patches, which are irregular in shape, with lateral dimensions that range from several hundred nanometers to 5 μm, while the thickness of PM sheets is rather constant at ~5 nm (37). PM patches are produced naturally in the cell membrane under proper environmental conditions in the form of repeating elements of the hexagonal two-dimensional crystalline lattice, which is composed of three identical bR protein chains, each rotated by 120 degrees relative to the others (47). This unique crystalline nature not only distinguishes bR from all other retinal proteins that also bearing a seven transmembrane helix configuration but also makes it possible to determine the molecular structure of bR at ultra-low temperatures using electron diffraction (48).

Since the discovery of bR 30 years ago, continuous efforts have been made to determine its structure at its unilluminated "ground" state and the structure of

any attached molecules related to its function at high resolution, which requires a level of accuracy equivalent to that achieved for optimum protein structures. In the process of ascertaining the structure of bR, cryo-electron microscopy, electron diffraction, and X-ray crystallography have provided many valuable data, compared with other means of characterization.

The first three-dimensional structure (Fig. 2-2) of bR at a resolution of 7.0 Å, which was determined by Henderson and Unwin using electron microscopy in 1975 (49-50), revealed that it contained seven rod-shaped densities assumed to be α-helices. As its resolution being improved over the following years, this model served as the starting point of all studies of the proton transport mechanism of bR (51). Different crystal forms of PM were then investigated to ascribe the molecular boundaries. Research of both the orthorhombic form at 6.5 Å resolution (52-53)(52-53)(52-53)(52-53)(52-53) and a contracted trigonal form at 6.0 Å resolution (54-55) identified the most important characteristics of the native p3 molecule and revealed the lipid molecules enclosing the bR molecules to be highly ordered (54). Subsequently, with the data obtained from two-dimensional cryo-electron diffraction analysis, Henderson's group demonstrated the first interpretable three-dimensional map of PM patches with a resolution of 3.5 Å parallel and 7.8 Å perpendicular of the membrane plane (Fig. 2-3a), not only substantiating the seven-helix structure of bR suggested by Henderson and Unwin in 1975 (49), but also clearly resolving density peaks for major aromatic side-chains. By revealing the chemical details of bR for the
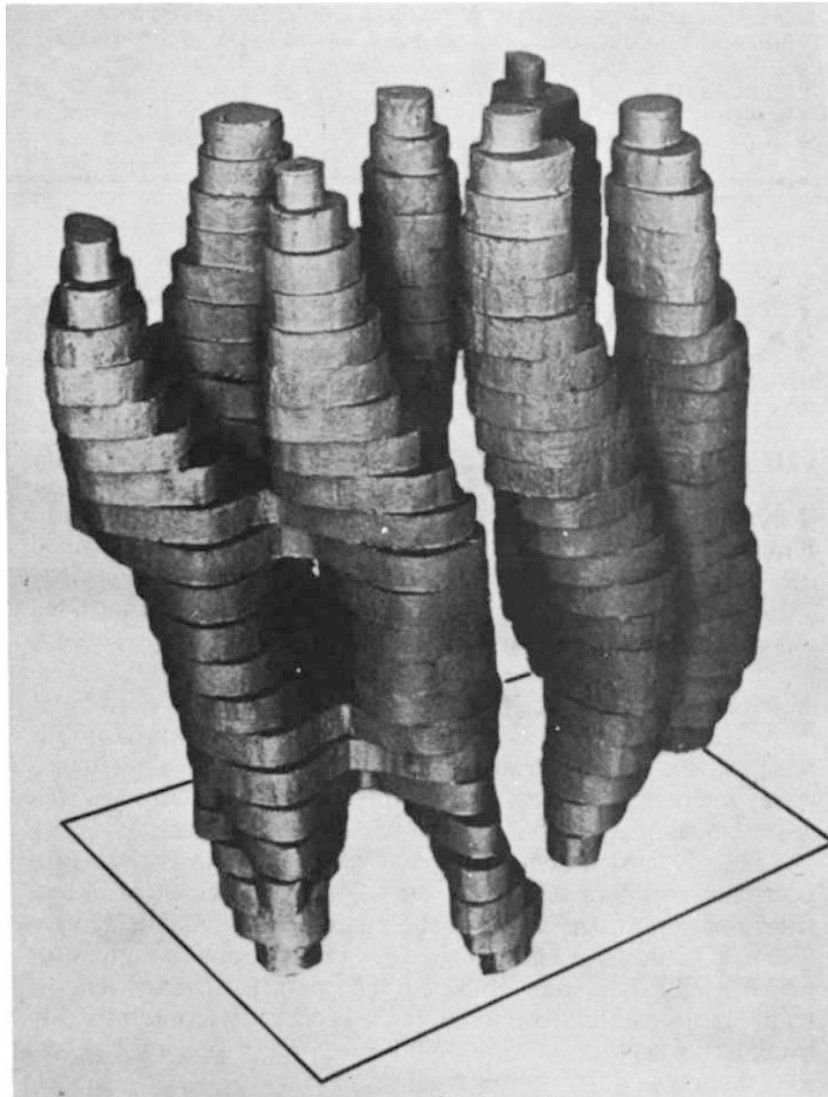
Figure 2-2 The first model of a single bR molecule in a PM, viewed roughly parallel to the plane of the membrane. The top and bottom of the model correspond to the parts of the protein in contact with the solvent, the remainder being in contact with lipid. The most strongly tilted α helices are in the foreground (49).

first time, this map made it possible to interpret the structure of bR comprehensively in terms of the amino acid sequence of the protein via showing chemical details of bR (56-57), allowing the attribution of the intrahelical loops as well as many of the important intramembrane residues that had been poorly resolved in previous structures (58-59). Throughout the 1970s, the structure of bR at higher resolution had remained unclear, mainly due to the

use of inadequate techniques. During 1980s and 1990s, technique improvements in conducting the X-ray crystallography of bR led to remarkable progress in not only preparation of the protein sample into well-ordered three-dimensional crystals, a requirement for high-resolution X-ray crystallography (53, 60-62), but also the enhanced resolution of two-dimensional bR crystals acquired by electron crystallography (52, 55, 63). Consequently, a more precise three-dimensional structural model at an atomic resolution (2.5 Å; Fig. 2-3b) was obtained (64), providing detailed information on the sites of the water molecules in the membrane protein essential for bR biological functioning as well as more precise reconstruction of most of the side chains that had been previously observed.

A subsequent major breakthrough in crystallizing bR via three-dimensional crystal growth using the cubic lipid-phase method (65-66) led to significant increase in the resolution of three-dimensional crystals studied by X-ray crystallography. Specifically, the structure of bR and the lipid matrix surrounding it were defined by X-ray diffraction to much improved resolution (67-68) - as high as 1.43 Å (69) - providing extraordinarily extensive data on the membrane protein and its functioning, including definite determination of the side-chain positions and more comprehensible recognition on the sites of bound water and their hydrogen bonding.
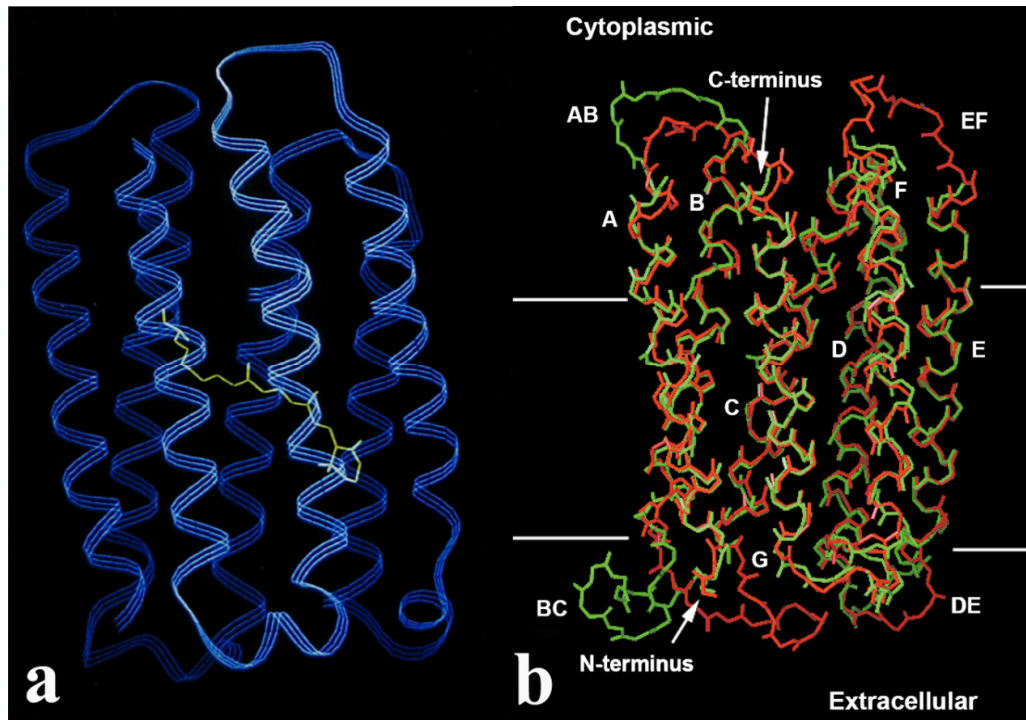
Figure 2-3 (a) A rough atomic model of the overall chain trace of bR in a ribbon diagram at a resolution of 3.5 Å following the backbone of the polypeptide. Helix A, on the left, is connected to helix B at the top; helix B to helix C at the bottom; helix C to helix D at the top; helix D to helix E at the bottom; helix E to helix F at the top; and helix F to helix G at the bottom. The N terminus (nt) is at the bottom at the EC surface; the C terminus (ct) is at the top at the CP surface. Both diagrams show the retinal and its connection to Lys216(59); (b) 2.5 Å view of the a helices of a bR monomer perpendicular to the membrane plane. The model derived from X-ray analysis is shown in green; the earlier model from EM (58) is represented in red. The retinal is not shown. The overall structure of bR is composed of seven helices [values in parentheses are from the EM model (58)]: A, residues 10 to 30 (9 to 31); B, residues 39 to 62 (39 to 62); C, residues 77 to 101 (77 to 100); D, residues 105 to 127 (105 to 127); E, residues 134 to 156 (134 to 157); F, residues 169 to 191 (166 to 190); and G, residues 202 to 224 (202 to 226). The backbones superimpose very well in the helical transmembrane regions, but distinct differences are revealed in loops AB (upper left) and BC (lower left). N-terminal residues 1 to 6 and C-terminal residues 225 to 248, as well as loop EF (residues 157 to 166, upper right), are absent in the X-ray structure and the EM model. Helices C and G deviate from standard a-helical geometry at residues 89 and 216, respectively. In the EM model, deviations (kinks) are observed in helices B, C, and F for residues 46 to 49, 87 to 90, and 182 to 185, respectively, but not in helix G. The horizontal lines delimit the hydrophobic core of bR (64).

15

2.2.3 Proton Pumping and bR Photocycle

As previously discussed, bR plays a key role in the photosynthesis of halobacteria (48, 70). When compared with the chlorophyll-based photosynthetic systems mainly employed by plants, bR photosynthesis is very simple, as bR is the only protein needed to convert light energy into chemical energy in the photosynthetic system of halobacteria. The indispensability of bR as the energy converter in this process originates from its function as a light-driven proton pump that operates by proceeding through a series of conformational changes involving both the protein and the retinal chromophore (71-75). The primary reaction of bR upon the absorption of light (568±70nm) is its alteration from a dark-adapted form (containing 13-*cis* retinal) to a light-adapted form (containing all-*trans* retinal). Absorption of light by the latter allows bR to undergo a series of intermediates identified mainly by their absorption maxima (76-79).

In tandem with this intermediate transfer process, which is called the *photocycle* (Fig. 2-4), protons are pumped across the membrane from the CP side to the EC side, resulting in a pH gradient (ΔpH=0.2) to generate a driving force that is then employed by the halobacteria in the synthesis of ATP from ADP and inorganic phosphate (34). For the proper operation of any membrane pump, three conditions regarding three specific features must be satisfied (80):
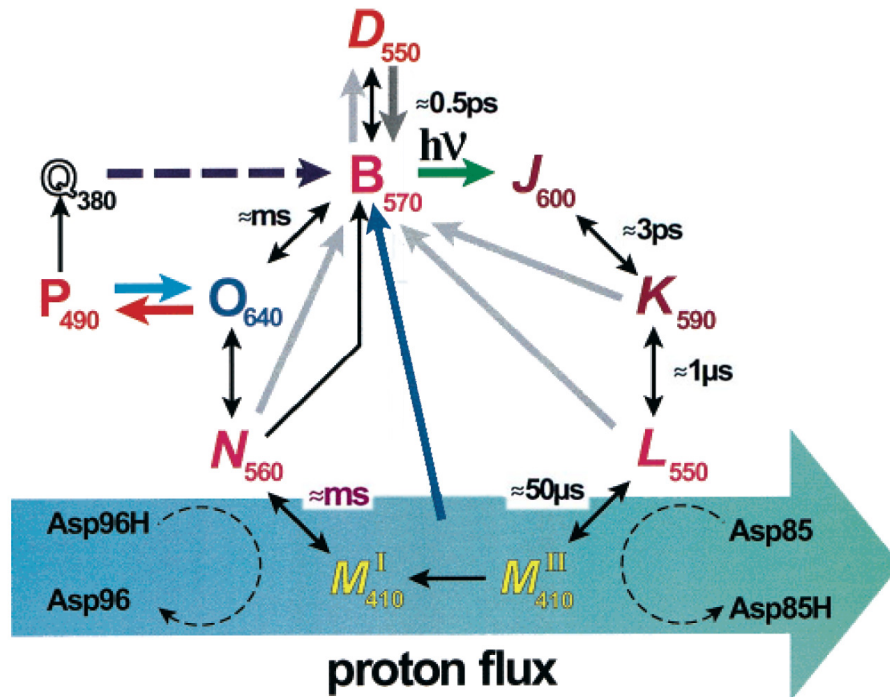
Figure 2-4 The bR photocycle. The different intermediates of the bR photocycle are represented by their common single-letter abbreviations with their absorption maxima as subscripts. Upright letters represent all-trans-retinal and slanted letters 13-cis-retinal containing states. During the L→M transition, the Schiff base is deprotonated and Asp85 becomes protonated. From there the proton moves toward the outer side of the EC part of the proton channel. During the M→N transition the Schiff base is reprotonated, with aspartic acid 96 serving as a proton donor for this step. Asp96 is reprotonated through the cytoplasmatic proton half-channel (37).

(1) There must be a hollow space (binding site) sufficiently large on the inside of the membrane to accommodate the species to be transported.

(2) There must be two different conformations for the pump so that the binding site for transported species is accessible from different sides in different conformations.

(3) Corresponding to the two different conformations, the affinity of the binding site to the transported species must be different.

These features must be interpreted by the conformational changes observed in order to study the bR proton-pumping mechanism.

To obtain comprehensive understanding of bR biological functioning, simply obtaining structural data regarding the "ground" state of bR is insufficient. Over the years, kinetic models (48, 81-82) for the photocycle, which is directly related to the proton pumping, have been generated from numerous data obtained by diverse means of static and time-resolved spectroscopy, such as resonance Raman and Fourier-transform infrared (FTIR), as well as studies of site-specific mutants of bR. With the help of these experimental results, molecular events underlying the interconversions of the intermediates termed B, K, L, M, N, and O with dissimilar spectroscopical properties have been identified (83).

In the bR monomer, the "proton-transport channel" is characterized by several important amino acids. The retinal molecule forms the covalent link to a lysine residue roughly in the center of the seventh α-helix via a Schiff base dividing the "channel" into a CP half and an EC half that are distinguished by Asp96 and Asp85, respectively, which are two amino acids essential for the efficient proton transport of bR. There are several features involved in the adaptation of the maximum absorption of bR to its physiological function, including the configuration of the retinal; the protonation form of the Schiff base; and the delicate electrostatic interactions between the Schiff base and

charges approximately from the dipoles and Asp85, Asp212, and Arg82 in the bR molecule.

It is commonly accepted that the photocycle can be divided into six steps related to isomerization, ion transport, and accessibility change or switch. First, the retinal configuration isomerizes from all-*trans* to 13-*cis* upon illumination, followed by proton transportation from the Schiff base to the proton acceptor Asp85. Subsequently, a proton is released to the peripheral environment. It is supposed that the proton-release group is composed of Glu194, Glu204, and structural waters, although there is still no clear evidence (84-85). In order to make the vectorial transport of the proton (Fig. 2-5) possible, the accessibility of the Schiff base must change from extracellular to intracellular before reprotonation occurs from Asp96 in the CP channel. After the reprotonation occurs, a thermal reisomerization occurs to the retinal, and then the accessibility of the Schiff base switches back to extracellular. This description sketches the minimal number of steps responsible for the vectorial transport of protons in wild-type bR (48).

Regarding the intermediates in the photocycle, the "primary event" is ascribed to the phototransformation of bR to K. As the primary photoproduct, K is important in the photoisomerization of the protonated Schiff base from all-*trans* to 13-*cis* (86-91). Although it has a known precursor called J, K has been identified as the primary photoproduct because J is extremely unstable. A controversial hypothesis regarding J posits that J might be a combination of

species from both the ground state and trapped excited state (92). M is regarded as the most crucial thermal intermediate in the bR photocycle because its formation corresponds to the proton pumping (76, 93-99). Many experimental investigations included Resonance Raman (98, 100-109) and FTIR (97, 110-116) have confirmed that the Schiff base is protonated in all intermediates but M (34). De- and reprotonation of the Schiff base must occur from different sides of the membrane to allow vectorial proton transport. Consequently, at least two M intermediates with different means of accessibility to the Schiff base must exist, and are interconverted in a step termed the "switch," in which Mec (M^{I})→Mcp (M^{II}), where ec and cp represent EC and CP accessibility, respectively. It is important to note that while all other transitions between the intermediates are reversible, the conversion of M^{I} to M^{II} is an irreversible step (117-118) in the photocycle. During this conversion, the accessibility of the nitrogen in the Schiff base group changes from the EC to the CP half of the proton channel (48), guaranteeing a switch in accessibility to the retinal, making the subsequent reprotonation of the Schiff base from Asp96 on the CP side possible (119), which corresponds spectrally to the M^{II} to N transition. Consecutively, Asp96 is reprotonated from the CP side, and the absorption peak is further red-shifted as the thermal reisomerization of the retinal back to the all-$trans$ configuration occurs. Finally, when a proton is transferred from Asp85 to the assumed release group on the EC side via Arg82 (120), the ground state is recovered.
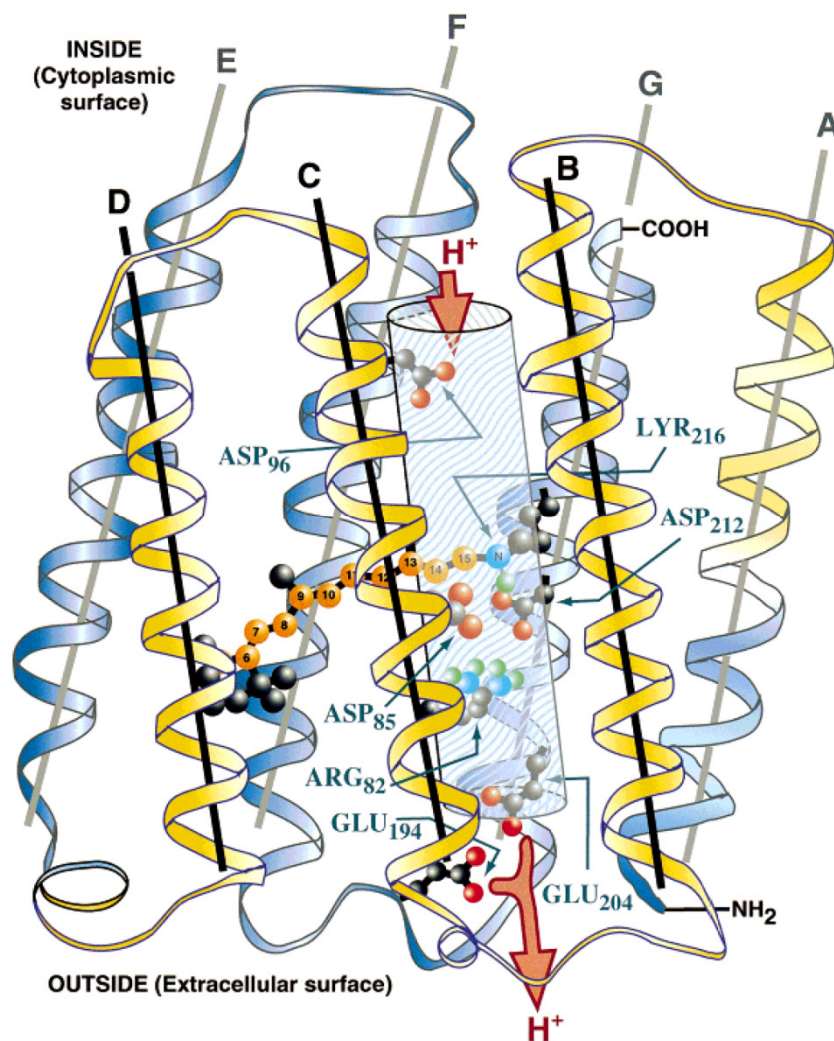
Figure 2-5 Simplified structure of the protein (a) and the key intermediates in the primary and branched photocycle (b) of bR. Wavelength maxima (in parentheses, nm) and lifetimes apply to the wild-type only and are approximate (121).

Since the discovery of bR 30 years ago, a number of biophysical methods have been used to clarify the precise nature of not only bR at its ground state but also changes in each step of the photocycle and their relationship to proton-transport function. Table 2-1 summarizes the essential properties of bR and PM.

Table 2-1 Properties of PM and bR (122)

Purple membranes	Bacteriorhodopsin
contains lipids and bR only	molecular weight = 26,784 Da
two-dimensional, hexagonal crystalline lattice of bR trimers	248 amino acids and 1 retinal (attached to the lysine-216)
buoyant density = 1.18 g/cm^3	isoelectric point = 4-5
refractive index = 1.45-1.55	quantum efficiency $\Phi_{B\rightarrow J} \geq 64\%$
thickness = 5 nm	no refractory period of the photocycle
shape irregular	after light absorption occurs
stable towards	- all-trans→13-cis isomerization
- exposure to sunlight for years	- de-/reprotonation of Schiff base
- temperatures up to 140 °C (dry)	- conformational switch of nitrogen accessibility from extracellular to intracellular
- pH values = 0-12	
sensitive to polar organic solvents	

2.3 Bioelectronic Applications of bR

Grown in an extreme ecological niche, bR is rather different from other proteins that also play a key role in photosynthesis and visual perception. It is remarkably stable to illumination, oxygen, and environmental factors over a wide range of pH levels (0-12), temperatures (-196 to 70 ℃), and concentrations of salt (123) due to its natural occurrence as a two-dimensional crystal, which renders it both suitable for device applications and amenable to optimization. Among the few pioneering bR researchers, Russian scientist Vsevolodov and his colleagues (124) introduced the use of bR as an advanced functional material in their construction of "biochrom film," an imaging device using chemically modified bR.

2.3.1 Potential Bioelectronic Applications of bR

An attractive characteristic of bR compared to those of other proteins, and even some conventional inorganic or organic materials used in bioelectronic applications, is that the photosensitivity and cyclicity to illumination of its biological proton pump are far beyond that of synthetic materials (37). This *in vivo* light-driven proton pumping property is a basis for construction of *in vitro* photoelectric devices. In these applications, bR can be modified to a large extent to serve as a platform for an entirely new class of materials.

Potential applications of bR are determined directly by its basic biological functions. To illuminate this relationship, Figure 2-6 schematically describes the basic biological functions of bR and the corresponding physical effects. The photon excitation of the light-driven proton pump causes a concomitant charge separation, which accounts for the photoelectric properties of bR. Almost simultaneously, proton transport through the bR molecule, which relies on the deprotonation and reprotonation process of the Schiff base linkage in the photochromic group, causes a substantial blue shift in the bR maximum absorption of more than 150 nm, and thus distinctly differentiates the M intermediate from the ground state B. The distinct optical characteristics of the B and M states allow for bR to be utilized in photochromic applications Moreover, the simulation of the native function of bR in the photosynthesis of halobacteria also raises the probability of its conversion of light into chemical
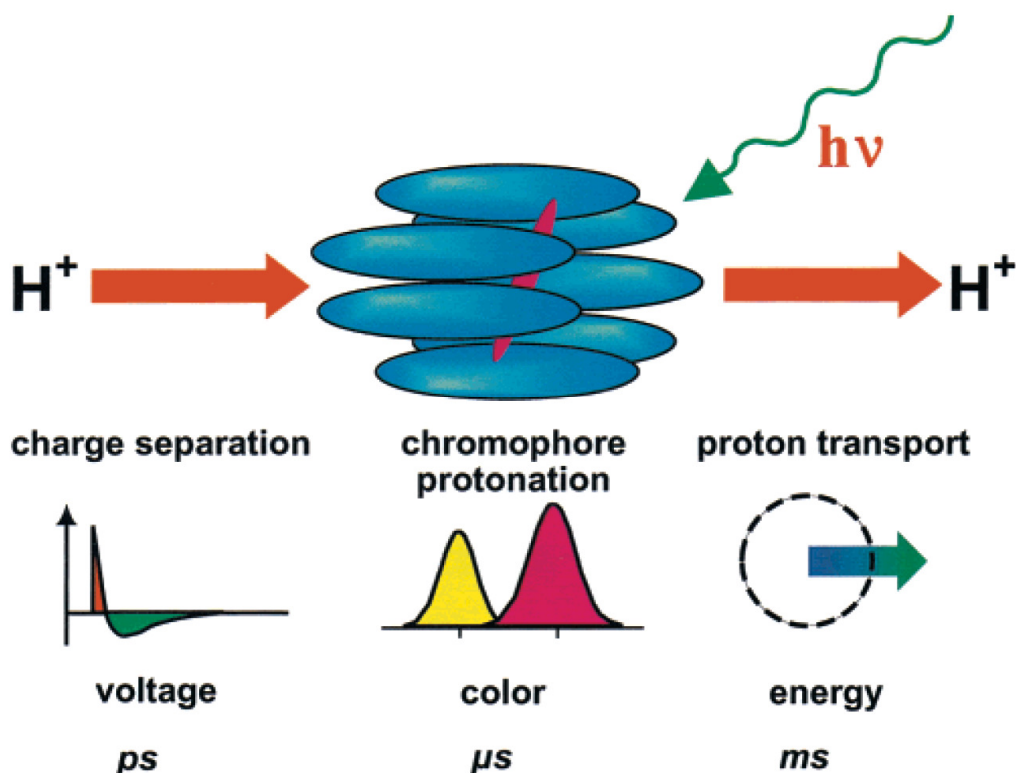
Figure 2-6 Basic molecular functions of bR. Proton transport is initialized by photon absorption and a charge separation step on the picosecond time scale. After approximately 50 μs, the deprotonation of the Schiff base leads to the main photochromic shift during the photocycle. After approximately 10 ms, the proton transport is completed (37).

energy on a macroscopic scale (125). The proposed technical applications of bR are classified in Table 2-2 (122).

As universal indicators of commercial potential, patents are more likely to reflect the practical value of new materials and techniques than their fundamental importance. bR-related patents proposed until 2009 are summarized in Figure 2-7, in which Figure 2-7a displays the number of patents during different time spans and Figure 2-7b provides statistics on the patents ascribed to different categories of the bR technical applications listed in Table 2-2. As shown in Figure 2-7a, the number of patents filed for bR-based

materials, devices, and applications from the early 1980s to the present has been continuously increasing, with the greatest rate between 1990 and 1999.

Table 2-2 Technical Applications Suggested for bR (37).

Production	Photochromic
mutant generation	information storage
cost effective production	2-D storage
Proton transport	3-D storage
ATP generation in reactors	holographic storage
desalination of seawater	associative memories
conversion of sunlight into electricity	information processing
Photoelectric	optical bistability/light switching
ultrafast light detection	optical filtering
artificial retinas	signal conditioning
motion detection	neural networks
Miscellaneous	spatial light modulators
2nd harmonic generation	phaseconjugation
radiation detection	pattern recognition
biosensor applications	interferometry
synthetic biology etc.	

Although it is still too early to conclude which category of bR applications will which the most patents have been filed, is likely to be the first (Fig. 2-7b). Regardless of the nature of its first applications, it appears that this biomaterial first become commercialized, the category of photochromic applications, in

possessing peculiar properties will be of technological as well as commercial importance in the near future.
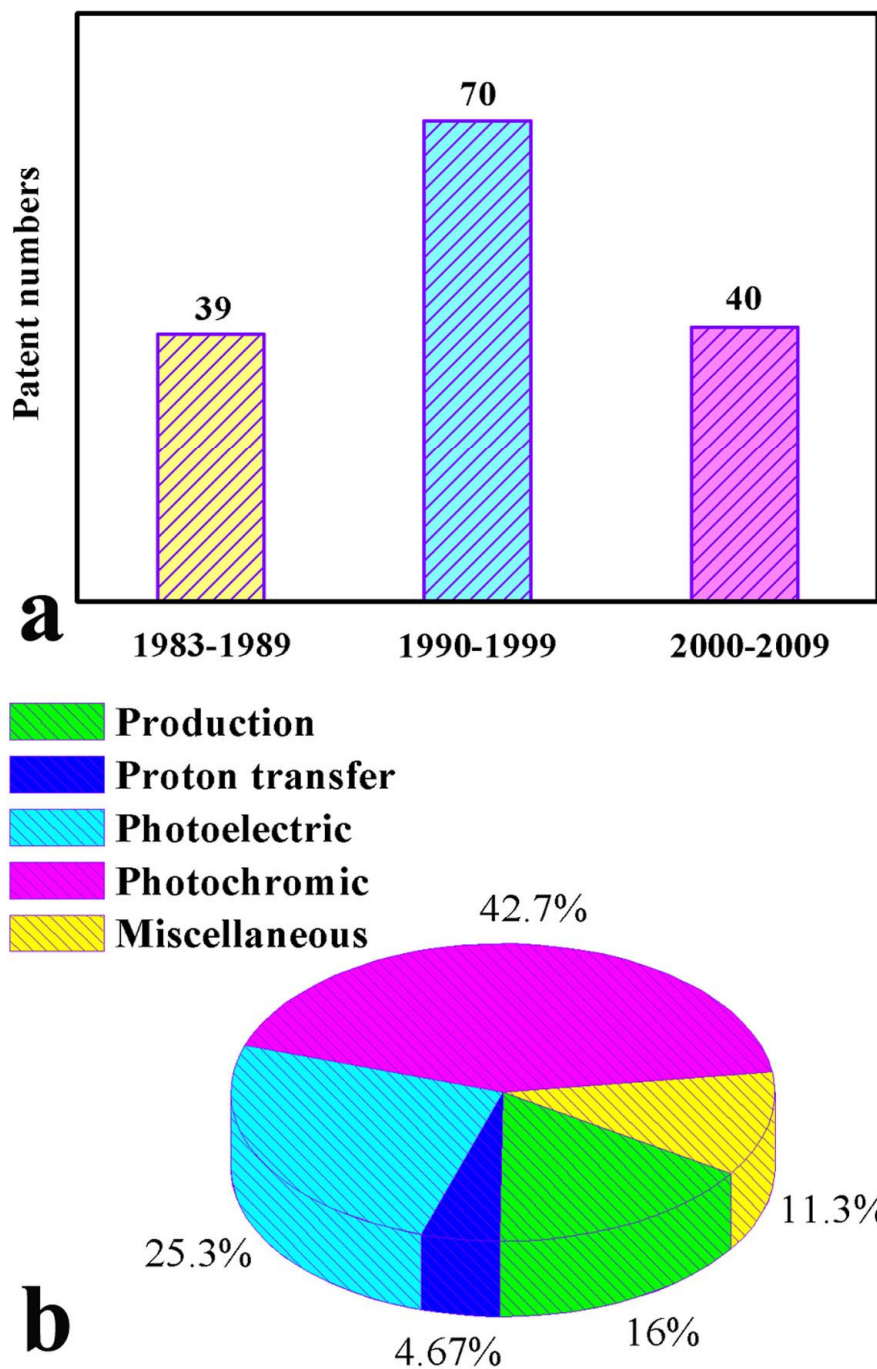
Figure 2-7 Statistics on bR-related patents according to records available from the patent searching database (http://www.freepatentsonline.com) from United States, Europe, and Japan until 2009 (national patents from European countries, Canada, Russia, China, etc. have not been included); (a) shows statistics according to year span and (b) shows statistics according to application category.

The complexity of the related devices and the demands on the biological components vary greatly among different bR applications. To obtain the best performance from bR-integrated technical systems, two issues must be considered: the structural requirements of the bR in the system and the interface of bR with the remainder of the integrated system (refer to Table 2-3).

Table 2-3 Main groups of bR applications, their differing microstructural demands, and the type of interface to the technical system required (37).

microstructural demands	photochromic	photoelectric	proton transport
orientation of PMs	**none**	**high**	**very high**
porosity of the PM layer	**not relevant**	**low**	**very low**
thickness of the PM layer	**not relevant monolayer**	**few layers**	**monolayer**
interface	**optical**	**electrical**	**chemical**

2.3.1.1 Photoelectrics

For photoelectric bR applications, it is required to attain the maximal electric signal with per photon absorbed, thus the key concern is the degree of the orientation of the PM patches (37). For light-dependent proton motive-force generation, at least one of the electrodes should be transparent in a bR-based photoelectric system. In addition, a liquid electrolyte or an embedded electrolyte-containing layer (126-127) is also needed to support the transition of the bR proton motive force into the electromotive force of a photoelectric cell. Applications based on photoelectric effects of bR include high-speed photodiodes and memories (128-129), artificial neural network (130), motion detector (127) and color discriminator (131). Although only super-fast

photodetection (132) were initially investigated, since then much more complex

bR-based motion detection systems (133), and even artificial retinas (128, 134),

have been constructed.

2.3.1.2 Photochromics

Among all bR applications, the technical level for both the structure

requirement of bR in the system and the interface of bR with the rest of the

integrated system is the lowest for photochromic applications (37), which may

be the reason why the greatest number of patents have been filed for optical

processing and optical storage based on the photochromic property of bR.

Orientation of PM patches is no longer a concern here, as just homogeneous

distribution of PM patches in an optically inert matrix material fulfills the

needs. Because the interface needed is an optical one, it is easy to protect the

bR media, which can be completely sealed between protective glass layers. For

these reasons, most of the successful technical applications reported or

patented, which range from methods of long-term data storage to optical and

holographic processors, are based on the photochromic properties of bR (135-

139).

2.3.1.3 Energy Conversion

The natural function of bR as a simple yet integral photosynthesis reaction

center in the *H. salinarium* that transforms light energy into electrochemical

energy led to initial suggestions that bR be used in technical applications (37). However, as of the time of this writing, it has been proven difficult to realize any practical applications (140-141). Theoretically, bR applications would require a large PM patch of approximately several square meters large containing unidirectional embedded bR molecules in a dense arrangement without any pores or holes that could lead to passive proton flux. However, such a perfect membrane could hardly be prepared in such large a dimension. Another challenge is that even if such a membrane were successfully constructed, any damage to it might cause a short circuit.

2.3.1.4 Other Applications

Besides those discussed above, other bR applications include biosensors used for anesthetics (142-143) and enzymic reaction analysis (144).

2.3.2 Photoelectric Properties of bR

The *photoelectric effect*, the general term used to describe the electricity generated in pigment-containing membranes by the absorption of light, was first discovered by Tien (145) in an artificial black lipid membrane formed from an extract of spinach leaves. As a pigment-containing membrane, bR maintains charge asymmetry on two sides of the membrane, thus generating an electric potential across the membrane or an electric current through the membrane in

response to light activation. The photoelectric properties of bR are utilized in some of its most interesting bioelectronic applications.

2.3.2.1 Underlying Mechanism of bR Photoelectric Properties

It is known that the photoelectric response of bR is related to its light-induced proton transport, the so-called *proton-motive force* (122). Two physical phenomena may result from the bR light-driven proton release and subsequent proton uptake on the CP side, either of which could result in an electrical signal: 1) A charge displacement accompanying the translocation of protons across the membrane may cause an electric potential difference across the membrane and/or 2) the release and uptake of protons may lower and raise, respectively, the pH on the CP side, producing a pH change at the interface of the membrane and the electrode. Accordingly, until now, there is no consensus regarding the molecular mechanism that accounts for the transient photocurrent generation.

Two groups of researchers have suggested that the bR transient photocurrent is due to a pH change at the interface of the membrane and the electrode (146-148). When Robertson and Lukashev examined bR photocurrent responses from the wild-type and a D96N mutant (146) with a nonprotonable asparagine replaced the protonable aspartate at position 96, they found that the substitution of D96N greatly reduced the rate of proton uptake. Specifically, they found that the photocurrent that resulted from the D96N mutant by turning

the light off was very low in amplitude and very slow in decay, probably because the low proton concentration change near the electrode decreased the proton-uptake rate. When El-Sayed's group observed the photoelectric responses of bR on indium tin oxide (ITO) electrodes under both pulsed and continuous light excitations (147-148), they found that the polarity of the differential photocurrents by continuous illumination was reversed at a low pH. They rationalized this phenomenon was aroused by invoking the proton release/uptake sequence in the bR photocycle, based on the assumption that the photocurrent originates in the pH response of the oxide electrode (149-150) due to proton release and uptake of bR.

In contrast, two other groups of researchers argue that the response mechanism of bR photocurrent does not relate to electron transfer but is generated electrostatically through charge displacement within the bR molecules (151-152). Koyama's group studied the transient photocurrent generated by randomly oriented patches of wild-type PM (126-127, 153) and transients produced by highly oriented patches of wild-type PM (151). They proposed that the bR photoelectric response corresponds to the displacement of positive charges to the electrode, which is in a direction opposite to that of the proton translocation. Even after conducting an intensive investigation of bR photoelectric behavior, Hong's group concluded that they could not prove that their explanation based on light-induced rapid charge displacement is universal (134, 154-164). They argued that although the charge-displacement model had

been demonstrated to be consistent in their own laboratory and that of many other researchers, one model alone could not account for the same set of data (165). However, Hong insisted that the pH change model proposed by Robertson and Lukashev was less viable as a general explanation of the differential responsivity of the photocurrent observed in many bR-based systems lacking an ITO electrode. Nevertheless, Hong commented that the model could still serve as a minor and complementary model for supplementary contribution to the transient photoelectric signal because the two mechanisms are not mutually exclusive when used to explain Robertson's data alone.

The pH change model was later substantiated by Koyama's group in its exploitation of bR photocurrent generation on gold electrodes (166). Koyama compromised by admitting that the two models could interpret two types of photoelectric responses reflecting different information regarding bR proton-translocating processes. Other studies of bR photoelectric responses using LbL as the immobilization technique (167-170) provided additional evidence of the feasibility of the pH change model. Although there is still no consensus regarding the mechanism of the bR photoelectric response, bR photoelectric applications remain very promising. Even data processing steps like those known from the retina can be realized if the bR interface to electrodes is well designed (122).

2.3.2.2 Immobilization of bR for Photoelectric Applications

Principles of bR Immobilization

The quality of biomaterials after they are immobilized onto solid supports for bioelectronic applications must be the same as their quality before immobilization. In other words, the native structure as well as the inherent properties of the biomaterials must be properly preserved during immobilization. To date, the methods used to immobilize bR film onto solid supports or into solid form have included Langmuir-Blodgett (LB) deposition (126, 171-173), electrophoretic sedimentation (EPS) (174), self-assembly (175-176), LbL adsorption (167-170), antigen-antibody molecular recognition (151, 177), sol-gel encapsulation (178-179), and the application of polymers as immobilizing matrices (180-181). These assembly methods have been proved successful in retaining the intrinsic structure of bR during immobilization due to the extraordinary stability of bR, which results from its particular crystalline structure.

Many of these assembly methods have also been able to render favorable bR arrangements and bR customization to fulfill the requirements needed for various applications arising from different bR properties. For example, photoelectric conversion by a bR-based device could only be efficient when bR molecules in the film are uniformly oriented because the proton pumping of bR occurs unidirectionally from the CP to the EC side (151). Thus, for bR-based

photoelectric applications, the LB, EPS, and LbL methods of immobilization could be used to realize the bR orientation necessary in the final assembly (182).

The following sections describe several important bR immobilization methods used in its photoelectric applications.

LB Deposition

Discovered by Langmuir in 1918, LB deposition is a nanofabrication technique used to create ultrathin films at the molecular level (183). It has been employed for multilayer deposition since 1934, when Blodgett found that the LB deposition process could be reproduced. The LB monolayer is usually formed by polar molecules containing a hydrophilic head and a hydrophobic tail. In the fabrication process, amphiphilic molecules are spread on an air-water interface, compressed and oriented, and then deposited into multilayer assemblies (184). The LB film forms from the deposition of the surface of a liquid onto a solid by immersing (or emersing) the solid substrate into (or from) the liquid. During each step, a monolayer is left, leading to the development of one large film with the desired thickness after repetition of the appropriate number of steps. As the thickness of each monolayer is known, the total thickness of an LB film can determined by simple addition.

Since its discovery, the LB technique has been the preferred technique for the molecularly controlled fabrication of nanostructured films (185). However,

this technique is still quite limited in that it only generally applicable to amphiphilic and water-insoluble molecules (185). Other types of molecules, especially those comprising water-soluble proteins, cannot be processed into ordered multilayers using this technique. Hwang et al. made the first attempt using this technique to fabricate oriented PM films in 1977 (186). For more sensitive PM fragments composed of protein and lipids, which are known to denature easily in most organic solvents, the LB technique must be more finely tuned. In order to reduce the loss in the film formation, mixed solvent systems of hexane/dimethylformamide and water have been used to retain PM biological activity and extraneous lipids such as soya-phospholipid added to improve the homogeneity of the films (127, 171-173).

Because the CP side of the PM was found more hydrophilic than the EC side at the air/water interface (187), the CP side was expected to face the subphase during LB monolayer formation (see Fig. 2-8). Early studies reported that almost 85% of the PM fragments in the LB films were arranged in the same direction (186). However, further detailed investigations using immunogold labeling and electron microscopy revealed that the PM orientation is considerably random in LB films (188).

In 1994, Koyama and his colleagues improved the orientation of the PM in LB films by applying biospecific antibodies with different antigen-binding sites for both a phospholipid hapten and a specific side of the bR (151, 177). They found that by using the phospholipid hapten as a monolayer template at the air-

water interface, over 85% bR orientation could be obtained. The highly ordered PM films could be prepared by the antigen/antibody molecular interaction and subsequently transferred onto solid supports using the LB method. The resulting photoelectric cells fabricated from these types of films demonstrated significantly improved photoelectric responses, further confirming that improved orientation of the PM had been achieved (151, 177).

Over the past 30 years, numerous studies have proven that it is possible to prepare LB films with high degree of bR orientation as well as a good photoelectric response. However, the preparation of thick LB films for PM, whose monolayer thickness is only 5 nm (37), is a rather time-consuming
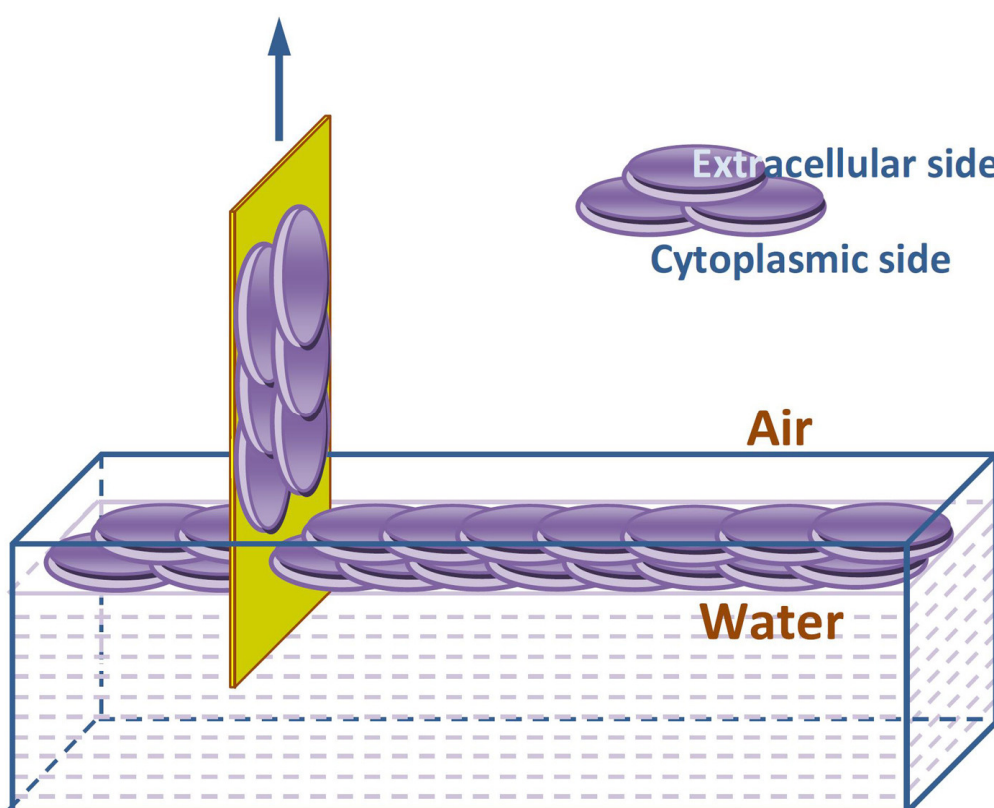
Figure 2-8 Schematic drawing of the preparation of PM film using the LB technique.

process that requires special equipment (185). Moreover, the prerequisite to achieve an ideal bR orientation in the LB film requires elaborate adjustments of the technique, which further decreases the feasibility of fabricating practical devices using the LB technique.

EPS Method

As biological membranes, PM fragments have a net negative charge on both their sides that result from the amino acid residues on the bR surface and the C-terminal and N-terminal of the polypeptide chain, as well as the intrinsically acidic lipids surrounding the bR molecules (189). However, due to uncertainty regarding the distribution of the lipids surrounding the bR molecules as well as the possible presence of cationic effects with a local pH, it is generally difficult to precisely determine the surface charge density of PM fragments. Although several different methods based on Gouy-Chapman theory have been investigated to measure the PM surface charge density, the results have been inconsistent, spanning a range from 0.5 to 9 negative charges per bR (190). The current consensus is that the PM is always negatively charged, and the CP side is more negative than the EC side when the pH is greater than 5 and vice versa when the pH is less than 5 (190). A permanent dipole moment directed from the CP side to the EC side results from this PM charge asymmetry (191).

E=20-30V/cm
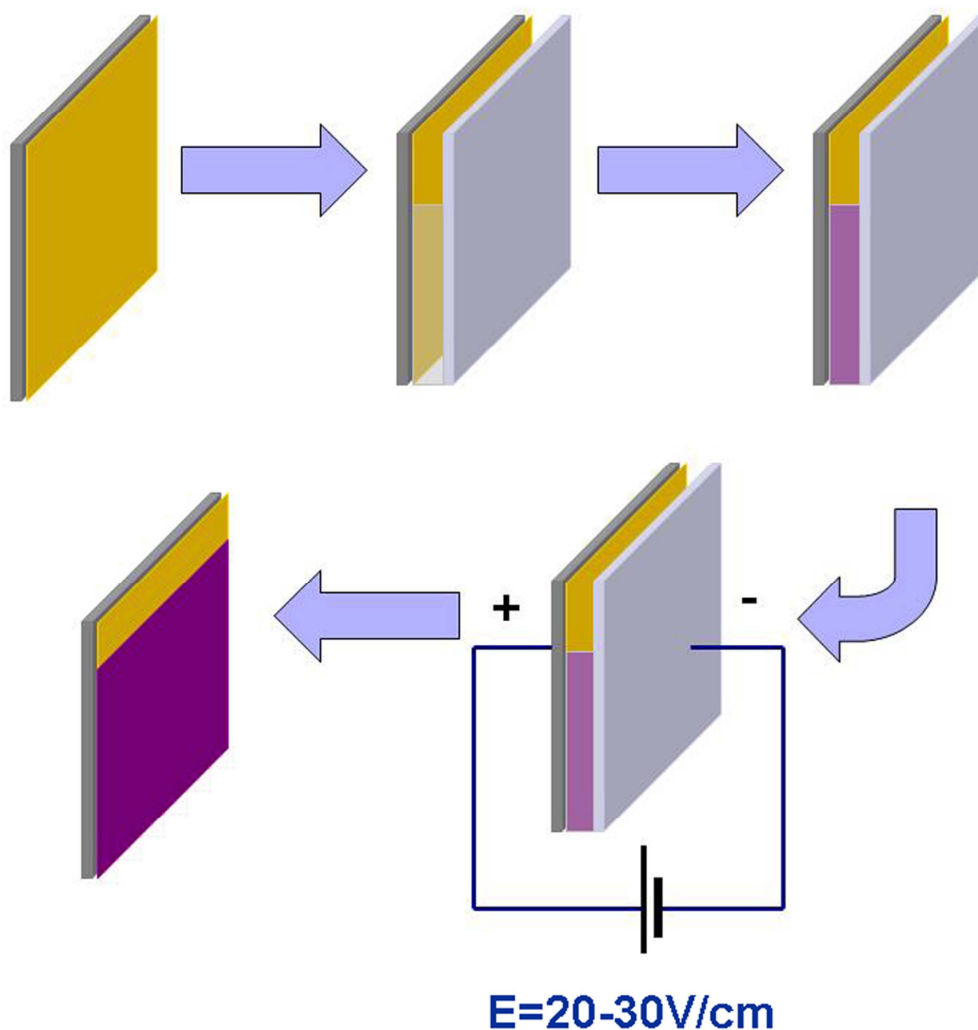
Figure 2-9 Setup for the fabrication of oriented PM films using the EPS method.

Because of the net electric dipole moment existing in PM, when an external electric field is applied to an aqueous PM solution, the PM fragments will arrange themselves in the direction of the external electric field. Moreover, when two electrodes are inserted into a PM suspension and an electric field of 20 to 30 V/cm is applied, the PM fragments will electrophoretically move and deposit onto the cathode, forming an oriented PM film (174). Fabrication of oriented PM films using the EPS method is simple, rapid, and effective, and allows for control of the side of the PM (EC or CP) that faces the cathode

(substrate) by simple adjustment of the pH of the PM suspension used (147-148). Moreover, within the same immobilization parameters, such as electric field intensity and time applied, the thickness of the PM film can be altered by applying different concentrations of the PM suspension. Figure 2-9 illustrates the standard setup for preparing an oriented PM film using the EPS technique.

LbL Technique

The electrostatic LbL approach, which is based on the strong electrostatic interaction between oppositely charged polyelectrolytes, was first employed by Decher and co-workers (192) for the alternate layering of oppositely charged polyelectrolytes and by Rubner (193-194) for the electrostatic layering of conducting polymers. In LbL assembly, spontaneous sequential adsorption of polycations and polyanions is performed by placing charged surfaces into dilute aqueous solutions. Typically, a charged solid support is immersed into an oppositely charged polyion solution, which results in an electrostatic attraction between the charged surface and the molecules with an opposite charge in solution. When the concentration of polyions reaches a certain level, adsorption occurs until there is a complete charge reversal at the solid support surface. After being rinsed in water, the support is then exposed to a solution of the oppositely charged polyion and the process repeated until the desired number of layers is achieved. When using this adsorption technique, the main concern is ensuring that complete charge reversal occurs after each deposition into the

polymer solutions in order to obtain continuous and homogeneous multilayer film formation. This technique is extremely simple, flexible, and effective for the assembly of oppositely charged species onto solid supports (185) as well as extremely versatile, as the structure, components, and thickness of the films can be controlled through the judicious choice of electrolytes and processing conditions.

The LbL method has been extended to a wide variety of other charged materials, including dendrimers, azo polymers, poly (p-phenylenevinylene) (a polymer used in light-emitting diodes) (195-198), metal and semiconductor nanoparticles, organic microcrystals (199-201), and inorganic and organic materials (202-203). The LbL method has even proven effective for the layering of biomaterials such as proteins, enzymes, DNA, and viruses (204-208). The LbL method is desirable largely because of its versatility: it can be used to produce layers of virtually any charged material under the proper conditions. In the case of biomaterials, the LbL method is also advantageous because the conditions of deposition may be altered to specifically protect the biofunctionality of the material of interest.

As previously discussed, PM fragments have an asymmetrical, negatively charged surface on which the CP side contains more negative charges than the EC side at pH values above 5 (190, 209), a property that makes PM very suitable for layering using the LbL method. It appears that the asymmetry of PM also provides for a high degree of PM orientation, similar to that obtained

using the EPS method (169-170). Since neither an external electric field nor any organic solvent is required, LbL deposition is a milder method for the fabrication of oriented PM assemblies. In addition, the versatility offered by this technique can integrate bR with other interesting systems to either enhance bR properties or add additional functionality to the final assemblies for a host of potential optoelectronic applications.

2.3.3 Development of bR Photoelectric Applications

The most demanding bR-based photoelectric device structure uses the unidirectional, photocycle-related electric response, which can be obtained only if the bR in the device has a net orientation. Maintaining a sound environment beneficial for bR proton translocation, which might be provided by other functional materials incorporated into the bR, can also aid in the enhancement of bR photoelectric performance.

2.3.3.1 Improvement of bR Orientation Techniques

Since the uniform orientation of bR onto a solid support ensures a unidirectional proton translocation across the membrane, thus rendering the maximum photoelectric response, it has attracted the attention of many scientists. Among these researchers, Choi's group spared no effort in trying to determine the optimal conditions for different bR immobilization techniques, including EPS (210-212), self assembly (213-215) and LB deposition (216-217).

He et al.'s initial introduction of the electrostatic LbL technique to the immobilization of bR (169-170, 218) by employing poly(dimethyldiallylammonium chloride) (PDAC) as the polycationic assembler was followed by other researchers' work using poly(allylamine hydrochloride) (PAH) (168) and poly(ethylenimine) (PEI) (168) as the assemblers. Since the LbL technique requires direct contact between the positively charged assembler and bR, the properties of the assembler must be taken into account for the enhanced photoelectric performance of the bR-based multilayer structure, providing prospective for more work to be conducted on screening more efficient assemblers.

2.3.3.2 Functional Material Integration with bR

Jin et al. claimed that the bR monolayer orientation can be significantly improved by electrostatic adsorption using vesicle fusion tactics (219-220) or acetylation of the bR lysines (221). Both processes are consistent with the concept that modified biological molecules are preferred to native molecules as possible active elements in bioelectronic devices because the modification may help to overcome several inherent weaknesses of pure biomolecules, such as susceptibility to environmental influences.

When Horn et al. (222) attempted to adsorb bR onto nano-black lipid membrane, they obtained a steady-state photocurrent following a capacitive spike, indicating that the pattern as well as the amplitude of the photoelectric

response could be adjusted by external modification of a bR-based system. When Bromley et al. (223) subsequently composed bio-functional mesolamellar nanocomposites based on inorganic/polymer intercalation in bR films, they achieved integrated a bR-based system with improved photoelectric performance, further proving it is possible to integrate functional materials into bR to obtain better performance in bioelectronic applications.

2.4 Perspectives on Bioelectronic Application of bR-Based Assemblies

Over 30 years since the discovery of bR, tremendous efforts have been made to thoroughly study the amazing biomaterial of its detailed structure, photocycle and almost every intermediate, biological function and immobilization techniques. Due to the significance of bR photoelectric properties that rendering it the ability to convert light energy into electrical energy, investigation of the possible underlying mechanism has been paid special attention to, although there is still much debate on this issue.

The unclear mechanism, however, has not hampered attempts to enhance the photoelectric response of bR. In recent years, the improvement of bR orientation techniques as well as functional material integration with bR has become attractive strategies to improve bR photoelectric performance and great progress has been made by several groups working on bR, as discussed in

section 2.3.3. Nevertheless, achievement obtained to date is still far from the requirement of viable applications.

Fortunately, the prosperity in the field of material science, especially the emerging of novel nanomaterial one after another has brought numerous chances for original integrations of bR and nanomaterials with specific physicochemical properties that could result in advances in the development of bR photoelectric application as well as other bioelectronic applications.

Chapter 3 Experimental Approaches

3.1 Materials and Equipment

3.1.1 Reagents and Chemicals

Unless otherwise indicated, all reagents and chemicals described below were used in this study's experiments without further purification. All H_2O used in the study was ultrapure H_2O provided by the MilliQ water purification system (Q-Grad 1, Millipore, USA).

3.1.1.1 Biological Reagents and Kits

bR (being isolated from the *H. salinarum* strain S9 as PMs, used as a control) and bovine serum albumin (BSA) were purchased from Sigma-Aldrich Co., USA. DNase I was purchased from Roche, Germany. Precision Plus Protein All Blue Standards was purchased from Bio-Rad, USA. Color Silver Stain Kit was purchased from Pierce, USA.

3.1.1.2 Chemicals

NaCl; Na_2TeO_3; $CdCl_2$; L-cysteine; $NaBH_4$; tungsten powder (12 micron, 99.9%); 2-propanol (IPA); H_2SO_4, HCl (36.5-38.0%); NaOH; PVA (MW 89,000-98,000, 99% hydrolyzed); PLL (MW 70,000-150,000); 11-mercaptoundecanoic acid (11-MUA); ethanol; acetone; tetraethyl orthosilicate (TEOS, $Si(OC_2H_5)_4$); $NH_3 \cdot H_2O$, H_2O_2 (30%); phosphate buffered saline (PBS,

10×); amonium persulfate (APS); and N, N, N,' and N'-tetramethylethylene (TEMED) were purchased from Sigma-Aldrich Co., USA. Trisodium citrate• $2H_2O$ was purchased from Merck, Germany. KCl and $MgSO_4•7H_2O$ were purchased from Fisher, UK. Bacteriological peptone was purchased from Oxoid, UK. Acrylamide mix (30%), tris base, and sodium dodecyl sulfate (SDS) were purchased from Bio-Rad, USA. TiO_2 granules (P25, containing crystalline phases of anatase and rutile with the ratio of 6:4) were purchased from Degussa, Singapore. Photoresist (AZ7220) was purchased from Clariant, Singapore.

3.1.1.3 Buffers and Medium

Halobacteria Culture Medium

250 g NaCl, 20 g $MgSO_4•7H_2O$, 3 g trisodium citrate• $2H_2O$, 2 g KCl, and 10 g bacteriological peptone were contained in 1 liter of the culture medium. The pH of the medium was self-adjusted to 7.0 with this recipe before autoclaving.

Basal Salt Medium

250 g NaCl, 6.56 g $MgSO_4•7H_2O$, 3 g trisodium citrate• $2H_2O$, and 2 g KCl, were contained in 1 liter of the medium.

Buffers for SDS- Polyacrylamide gel electrophoresis (PAGE)

- 5x loading buffer

10% w/v	SDS
10 mM	Dithiothreitol, or beta-mercapto-ethanol
20 % v/v	Glycerol
0.2 M	Tris-HCl, pH 6.8
0.05% w/v	Bromophenol blue

- 1x running buffer

25 mM	Tris-HCl
200 mM	Glycine
0.1% (w/v)	SDS

- 1x stacking gel solution

H_2O	2.1 ml
Acrylamide/Bis-acrylamide (30%/0.8% w/v)	500 μl
1.0 M Tris-HCl, pH 6.8	380 μl
10% (w/v) SDS	30 μl
10% (w/v) APS	30 μl
TEMED	3 μl

- 1x separating gel solution (12%)

H_2O	3.3 ml
Acrylamide/Bis-acrylamide (30%/0.8% w/v)	4.0 ml
1.5 M Tris-HCl, pH 8.8	2.5 ml
10% (w/v) SDS	100 μl
10% (w/v) APS	100 μl
TEMED	4 μl

3.1.2 Other Consumables

3.5K MWCO SnakeSkin Pleated Dialysis Tubing was purchased from Pierce, USA. A gold-coated glass sensor disk for surface plasmon resonance (SPR) was purchased from Echo Chemie B.V., Netherlands. A Pt electrode was purchased from CH instruments, USA. A silicon tip for atomic force microscope (AFM) was purchased from Veeco, USA.

3.1.3 Equipment

The bacterial inoculation and initial bR isolation processes were conducted in a biological safety cabinet (BH class II series, Gelman, Singapore).

All sterilization was performed by autoclave (HICLAVE^{TM} HV-50, HIRAYAMA, Japan).

All bacterial cultures were prepared in the orbital shaking incubator (S300, Firstek Scientific, Singapore).

Nanomaterial synthesis was partly completed in the universal oven (UNB500, Memmert, Germany).

The solvent remove was completed using a rotary evaporator (LABOROTA 4000, Heidolph, Germany).

The bR purity was examined by SDS-PAGE (Powerpac^{TM} power supply and electrophoresis cell, Bio-Rad, USA).

The topology was characterized by atomic force microscopy (SPM 3100, Veeco Instruments Inc., USA).

The surface morphology was examined by field-effect scanning electron microscopy (FESEM, JEOL JSM-6700F FESEM, Japan).

The distribution of specific elements was detected by energy dispersive X-ray spectroscopy (JEOL EX-23000BU EDX Thermal Analyzer, Japan).

The microstructure was investigated by high-resolution transmission electron microscopy (HRTEM, JEM-2100F, Japan).

The crystal structure was characterized by X-ray powder diffraction (XRD, Bruker AXS X-ray diffractometer, Germany).

The thermal properties were determined by thermogravimetric analysis (TGA, Perkin Elmer Pyris Diamond thermogravimetric analyzer, USA).

The ultraviolet-visible spectroscopy (UV-Vis) was conducted using the U-

2800 spectrophotometer (HITACHI, Japan).

The fluorescence of thin film was scanned and recorded by a 2-D proteomic imaging system (ProXPRESS, Perkin Elmer, USA).

The photoluminescence intensity was determined using a spectrofluorimeter (HORIBA Fluolog-3, UK) with a xeon lamp as the light source and a photoncounting photomultiplier tube detector luminescence spectrometer (Aminco Bowman II, Thermo Electron, USA).

The light sources for the photoelectric investigation were an LD-pumped 532 nm laser (Fengyuan Optoelectronics Co. Ltd.) and the Polychrome V system (Till photonics, Germany).

The SPR spectrometry was obtained using the Autolab SPRINGLE system (Echo Chemie B.V., Netherlands), in which the light source was produced by a monochromatic p-polarized laser (λ=670 nm) and directed through a hemicylindrical glass prism (n_d=1.518 at 25 °C) onto the gold film. The incidence angle (θ_{SPR}) was obtained by measuring the intensity of reflected light with a photodiode detector among a dynamic range of 4000 m° (4°) at a frequency of 1 Hz.

All electrochemical measurements were made using an Autolab potentiostat/galvanostat (PGSTAT30, Echo Chemie B.V., Netherlands).

Thin metal films were deposited onto Si wafers using an electron beam evaporator (BOC Edwards A306, UK).

The electronic parameters for DEP alignment of nanowires onto the FET devices was controlled by the HP 4284 Precision LCR meter (USA).

The output and transfer characteristics of devices were characterized using an Agilent 4157B Semiconductor Parameter Analyzer System (USA) with a probe station (Summit 11751B-6 system, Cascade Microtech, USA).

3.2 Methodology

3.2.1 bR Growth and Purification

The purity and the concentration of bR can be better controlled by preparation in lab to meet the requirement of my research. To ensure the quality of bR used in this study, the isolation and purification of bR-embedded PM (bR-PM) is critical.

3.2.1.1 Halobacteria Culture

Because it is believed that the expression of bR in the *H. salinarum* strain S9 is not physiologically controlled but rather constitutively activated, this strain is considered a mimic of the anaerobic, illuminated state of *Halobacterium* cells (224). Due to its superior capacity to overexpress the wild-type bR (225), strain S9 was employed in all experiments.

The procedure for the growth of strain S9 was partially modified according to the protocol established by Oesterhelt and Stoeckenius (226). After inoculation, the bacteria-containing medium was cultured at 40 ℃ with continuous illumination as well as proper shaking for 120 hours so that the optimal yield of PM could be obtained.

3.2.1.2 Isolation of the bR-PM

Because no intracellular membranes are present in the *H. salinarum* cells, the cell membranes can be easily isolated. The only challenge in obtaining pure PM is removing other components, such as red membrane, from the cell membrane preparation.

Bacterial cells were harvested by pelleting the 1-liter cell culture of *H. salinarum* S9 at 13,000 g for 15 minutes and then resuspending the cells in 100 ml of a basal salt medium, with 1 mg DNAse I added before the overnight dialysis against 2 L of 0.1 M NaCl solution. This dialysis not only lysed the cells but also prevented the product from developing an excessive viscosity that might have resulted from the release of the DNA. The resulting solution was centrifuged at 40,000 g for 40 minutes and the combined reddish purple sediment then washed twice with H_2O by centrifugation at 54,000 g for 1.5 hours until the supernatant appeared colorless or only faintly purple. The final sediment was resuspended in the proper amount of H_2O and applied over a linear sucrose gradient of 30% to 50% density before 17 hours of centrifugation

at 100,000 g to remove the red membrane. The purple bands that appeared in the middle of the sucrose gradient were collected and the sucrose removed by dilution with H_2O and at least two episodes of centrifugation at 100,000 g. The final PM pellets were then resuspended with H_2O to obtain the desired concentration for further experimentation. All centrifugation processes were conducted at 4 ℃ (Fig. 3-1).
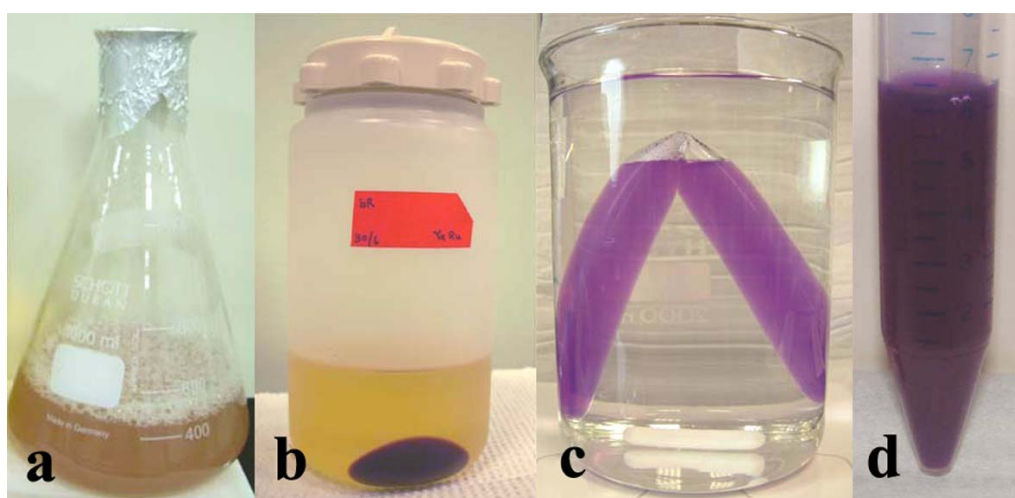
Figure 3-1 Main steps in PM isolation process: (a) bacterial culture, (b) bacterial cell pelleting, (c) cell suspension dialysis, and (d) final PM product.

3.2.1.3 Characterization of the isolated bR-PM

SDS-PAGE Analysis

The gel plate consisted of 12% separating solution and stacking solution.

By the SDS-PAGE bands generated by different samples shown in different columns, the purification process was confirmed to have been successful.

Moreover, the isolated bR was proved to be of high purity, even when compared to the commercial product (Fig. 3-2).
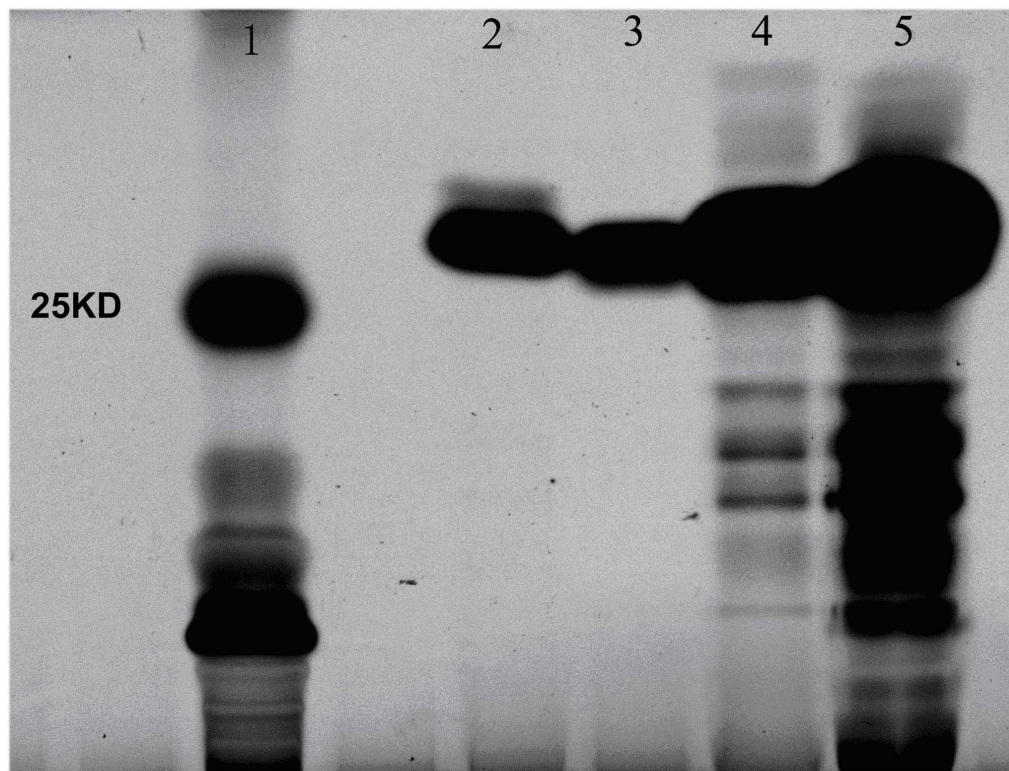
Figure 3-2 Silver staining result of the SDS-PAGE gel. C1. protein standard; C2. commercial bR; C3. pure bR product; C4. crude product before sucrose gradient centrifugation; C5. crude product just after dialysis.

UV-Vis Spectra

Because bR-PM has the characteristic absorption maximum at around 570 nm, by conducting UV-Vis spectra measurement, the concentration of isolated bR can be calculated according to its peak optical density (OD) value, with the suspension of the commercial bR of known concentration serving as control.

According to the Lambert-Beer's law: $A=\alpha lc$, it could be calculated from the OD reading shown in Figure 3-3 that the original concentration of the isolated

bR was approximately 28.23 mg/ml, indicating that the modified isolation procedure could produce a sample of high concentration with high purity and. The UV-Vis result of the isolated bR also revealed that the absorption ratio of A_{280nm}/A_{570nm} was below 1.7, confirming that the PM product was of high quality.
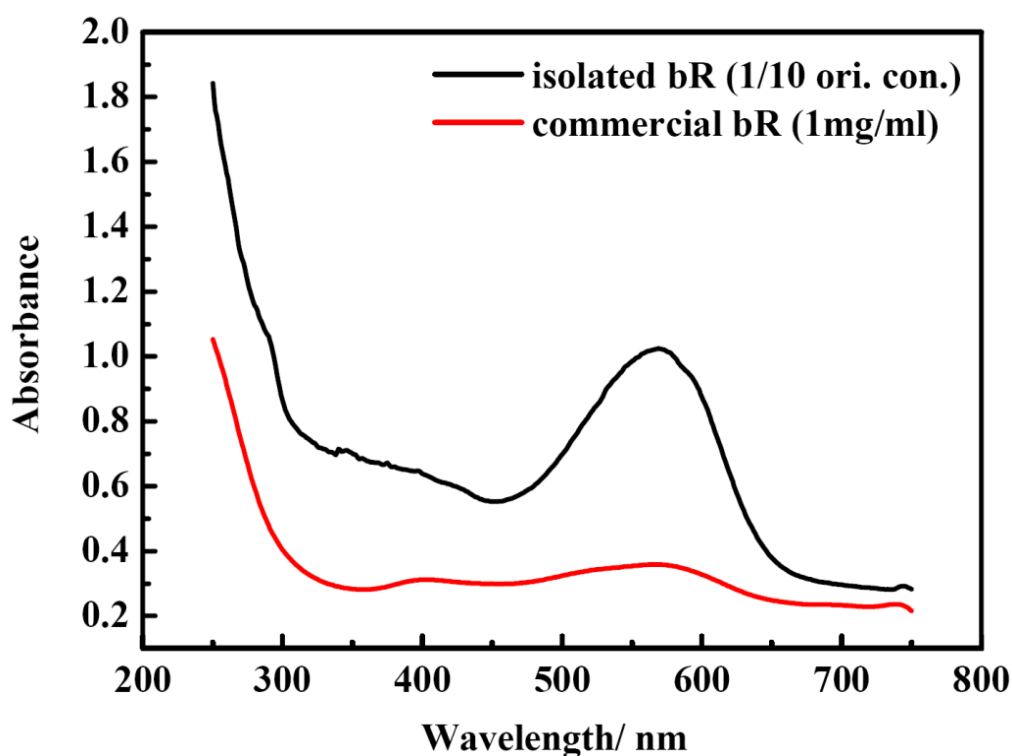
Figure 3-3 UV-Vis spectra of isolated bR and commercial bR.

AFM Image

As shown in Figure 3-4, the isolated bR had the same topology as that reported in the literature, which, together with the UV-Vis measurements and SDS-PAGE analysis, confirmed the quality of the isolated bR for further application.
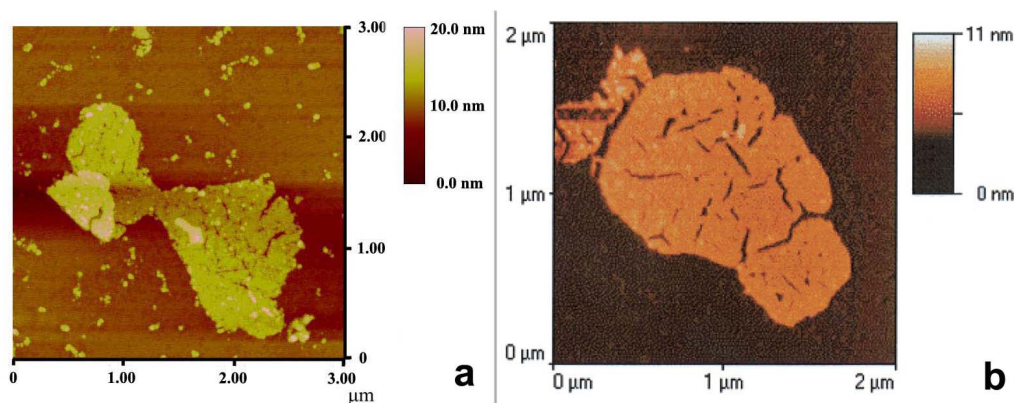
Figure 3-4 (a) AFM image of isolated bR and (b) that reported in the literature (37).

3.2.2 Photoelectric Measurement

An LD-pumped 532nm-laser (Fengyuan Optoelectronics Co. Ltd.), with the output power density at 20 mW•cm,$^{-2}$ and the Polychrome V system, with the output power density at 6.5 mW•cm^{-2} at 570 nm of illumination and at 7 mW•cm^{-2} at 410 of nm illumination, were used as the light sources during different parts of study. The photoelectric responses of pure bR as well as bR-based bionanosystems and the materials serving as controls were examined with potentiostats.

Amperometric and potentiometric chrono measurements at open circuit were conducted for the photocurrent and photopotential response, respectively. Gold assembled with bR or bR-based film was used as the working electrode and Pt wire was used as the counter electrode. The distance between the two electrodes in the photo-electrochemical cell was 8 mm with 0.1 mol/L PBS (pH=7.4) as the electrolyte.

Chapter 4 Fabrication of Oriented PLL/bR-PM Multilayer Structure for Enhanced Photoelectric Response [a]

4.1 Introduction

In previous studies, PDAC (169-170, 227), PAH (168) and PEI (228) were reported as polycationic assemblers in LbL deposition of bR-PM. Since the assembler plays critical role in determining the bR amount immobilized in the LbL multilayer film and thus affecting the photoelectric performance, there is a need to explore more efficient assembler in the LbL immobilization of bR-PM for photoelectric response improvement.

As a positively charged amino acid polymer, PLL is well known for not only its good biocompatibility (229) but also its easy conjugation with bioactive molecules (230-231). The most common application of PLL is as a nonspecific attachment factor in tissue cultureware coating to promote cell adhesion onto solid substrates by increasing the available positive charge (232-233). This polycation is also broadly employed as a linker or constructing element in the

---

[a] Reprinted from *Journal of Colloid and Interface Science*, 344(2010), Li, R., X. Q. Cui, W. H. Hu, Z. S. Lu and C. M. Li, Fabrication of oriented poly-L-lysine/bacteriorhodopsin-embedded purple membrane multilayer structure for enhanced photoelectric response, 150-157, Copyright (2009), with permission from Elsevier.

establishment of a DNA condensation and delivery system (234-235), as well as for conjugation with alginate in microencapsulation (236-237), microarray glass slide coating (238-239), tissue engineering (240-241), and LbL assembly of DNA (242) and some negatively charged proteins (243-244). However, prior to this study, PLL had never been used to assemble a bR-PM-based multilayer structure for improvement for enhancement of the bR photoelectric response. For the first time in this study, PLL was used to LbL construct a PLL/bR-PM multilayer structure by alternative adsorption of PLL and the bR-PM via electrostatic attraction between PLL and the negatively charged CP side of bR-PM (190, 209).

The effect on the photoelectric performance of the assembly by several fabrication parameters, such as PLL and bR-PM concentration, bR-PM suspension pH, and the adsorption time in the bR-PM suspension, as well as the optimal assembling conditions, were determined. The multilayer growth was monitored by UV-Vis, SPR, and AFM. Among these characterization methods, SPR was employed for the first time to provide quantitative data regarding the LbL adsorption of bR-PM. The photoelectric results indicate that the PLL/bR-PM multilayer assembly can generate a higher photocurrent than a bR-PM-based LbL structure utilizing other polycations.

4.2 Preparations and Measurements

4.2.1 bR-PM Suspension Preparation

The bR-PM fragments were suspended in water by ultrasonication for about 120 s to form suspensions with different concentrations. The suspensions were then adjusted to different pH levels using 0.1 M NaOH and 0.1 M HCl to determine the effect of concentration and pH on the photoelectric response of the PLL/bR-PM assembly.

4.2.2 Preparation of the PLL/bR-PM Multilayer Assembly onto Gold and Quartz

PLL was dissolved in Milli-Q H_2O to prepare different concentrations (pH=7.2) to determine the effect of its adsorption concentration on the assembly's photoelectric performance. The PLL/bR-PM composite films were deposited onto different solid supports for characterization and investigation, including quartz slides for UV-Vis absorption measurements, gold-coated glass sensor disks for SPR, and gold-sputtered (400-nm thickness) Si wafers for AFM and photoelectric performance measurements. The quartz supports were pretreated in a Piranha bath (a mixture of concentrated sulfuric acid and 30% hydrogen peroxide (3/1, v/v)) at 80 °C for 40 minutes, followed by ultrasonication in acetone and ethanol, respectively, with a thorough rinse with Milli-Q H_2O after each step. Commercial bare gold-coated glass disks and

freshly gold-sputtered Si wafers were pretreated only by ultrasonication in acetone and ethanol, respectively, with a thorough rinse with Milli-Q H_2O after each step. After treatment, the solid supports were stored in Milli-Q H_2O prior to use. The pretreatment procedure aimed at removing any possible impurities on the surface of the substrate.

To render a net negatively charged surface for subsequent PLL adsorption, the gold-sputtered Si wafer was immersed into a freshly prepared 1 mg/ml 11-MUA ethanol solution overnight, and their surfaces then rinsed with ethanol to remove non-covalently bonded MUA before use. The construction of the PLL/bR-PM assembly onto the gold surface is schematically illustrated in Figure 4-1. The MUA-modified negatively charged planar-gold surface was
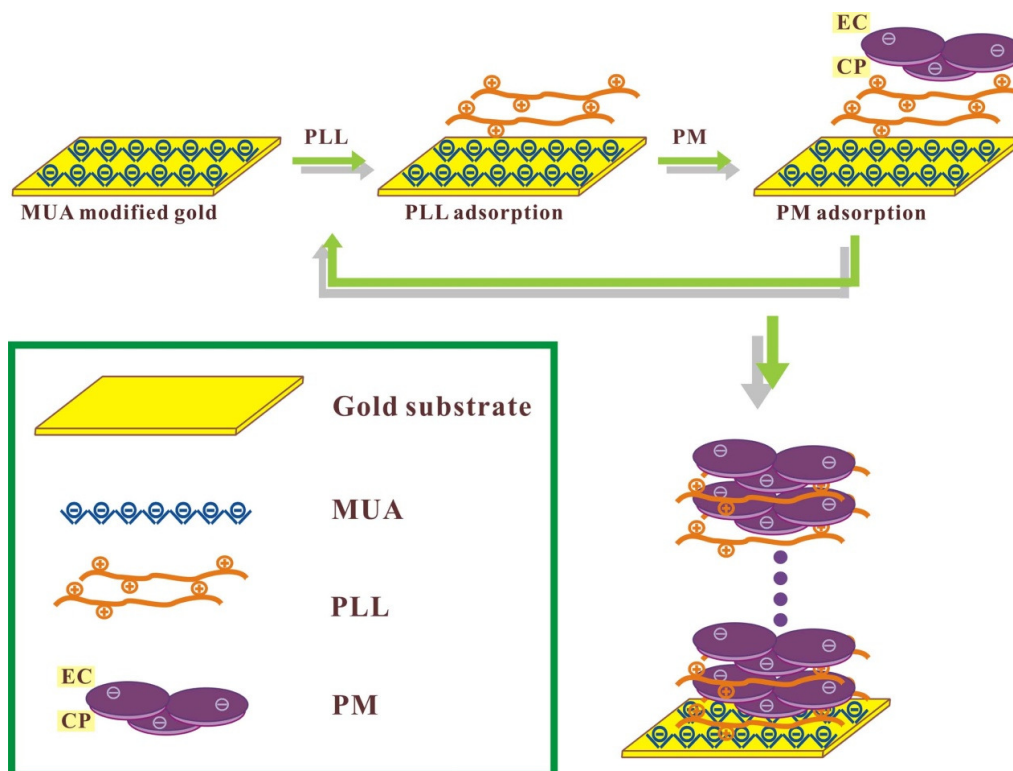
Figure 4-1 Schematic drawing of PLL/bR-PM alternate assembly employing a negatively charged gold surface.

immersed into PLL in which the adsorption concentration would be optimized for a monolayer growth of the polycation. After rinsing with Milli-Q H_2O for 2 minutes and then drying it gently with compressed air, the modified substrate was placed into a bR-PM suspension in which the adsorption concentration, assembly pH, and adsorption time would be optimized; rinsed with water of the same pH as the bR-PM suspension for 2 minutes; and dried gently with compressed air. This process, which resulted in the formation of the first PLL/bR-PM bilayer, was repeated until the desired number of bilayers of PLL/bR-PM had been obtained. All the adsorption procedures were carried out at room temperature (approximately 25 °C).
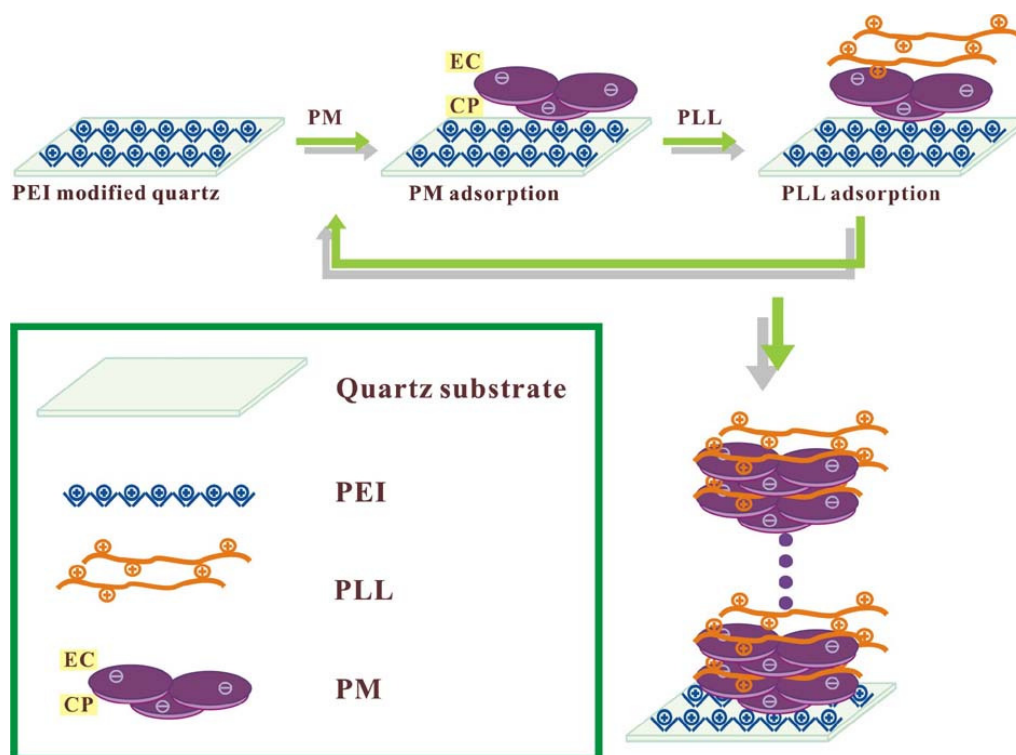
Figure 4-2 Schematic drawing of PLL/bR-PM alternate assembly employing a positively charged quartz surface.

The procedure used for the fabrication of the PLL/bR-PM ultra-thin composite assemblies onto a quartz surface consisted of the same steps as those

used for immobilization on the gold surface except that PEI rather than negatively charged MUA was employed to make the quartz surface positively charged in the first step (Fig. 4-2).

4.2.3 *In-Situ* SPR Measurements

The cleansed gold-coated glass disk was immersed in 11-MUA ethanol solution overnight to make the surface negatively charged and then rinsed with ethanol. The baseline of the SPR binding curve was measured after injecting 100 μl of Milli-Q H_2O. After the baseline became stable, 100 μl of PLL was added to replace the Milli-Q H_2O (indicated by arrow 1 in the binding curve in Figure 4-7 in section 4.4.1). After recording the binding curve, the PLL was replaced by Milli-Q H_2O (indicated by arrow 2 in the binding curve), and the bR-PM suspension was then injected to replace the Milli-Q H_2O (indicated by arrow 3 in the binding curve). Again, after measuring the binding curve, the bR-PM suspension was replaced by Milli-Q H_2O (indicated by arrow 4 in the binding curve). All experiments were conducted at room temperature.

4.3 Effects of Assembly Parameters on the Photoelectric Responses

4.3.1 Effect of PLL and bR-PM Concentration on PLL/bR-PM Assembly

To assemble the PLL/bR-PM structure, a fixed concentration of bR-PM
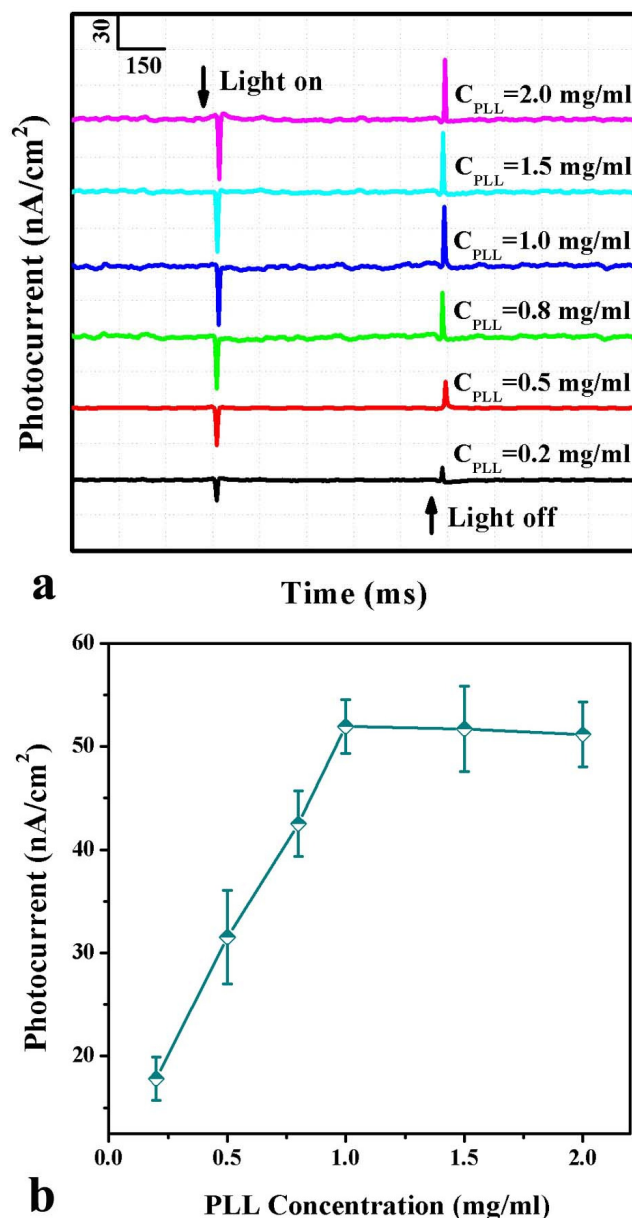
Figure 4-3 a) Photocurrent profile of PLL/bR-PM bilayer with different concentrations of PLL used; b) Peak light-on photocurrent at different PLL concentrations.

suspension (pH=7) at 5 mg/ml with a fixed adsorption time of 10 minutes was used to study the effect of PLL concentration on the photoelectric response. As shown in Figure 4-3a, the amplitude of the photocurrent generated by the PLL/bR-PM bilayer initially increases as the PLL concentration increases. When the PLL concentration rises to 1 mg/ml, the photocurrent reaches a maximum level that it maintains despite further increases in PLL concentration,

63

indicating that PLL-saturated adsorption on MUA via electrostatic attraction between the MUA carboxylate and the lysine ammonium groups occurs at a PLL concentration of 1 mg/ml, resulting in the maximum bR-PM adsorption and a photoelectric response plateau (Fig. 4-3b). Thus, 1 mg/ml PLL was used as the assembly concentration in all the following experiments.
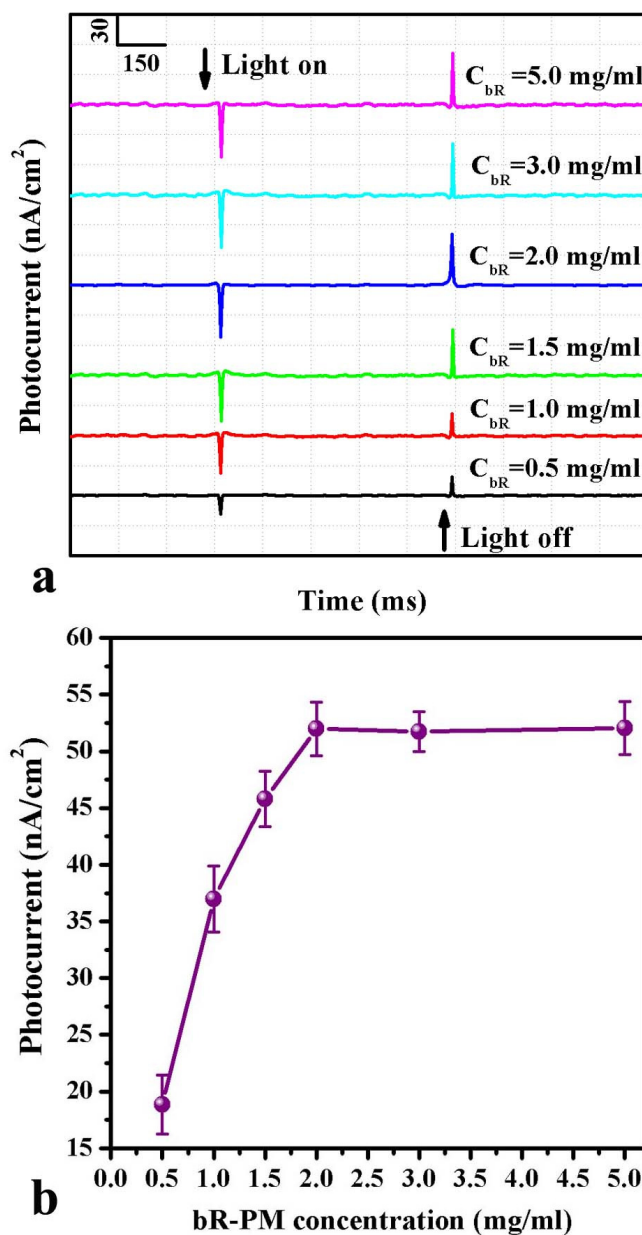
Figure 4-4 (a) Photocurrent profile of PLL/bR-PM bilayer at different bR-PM suspension concentrations. (b) Peak light-on photocurrent at different bR-PM suspension concentrations.

The effect of bR-PM suspension concentration on the photoelectric response of the assembly was also investigated. As shown in Figure 4-4a, the amplitude of the photocurrent generated by the PLL/bR-PM bilayer increases until the bR-PM concentration reaches 2 mg/ml, at which point a plateau photocurrent is maintained despite further increases in the bR-PM concentration. It has been reported that in the electrostatic LbL assembly mediated by PDAC (170), the adsorbed bR-PM is actually the monolayer. Because it appears that the maximum coverage of the bR-PM monolayer on the positively charged PLL surface can be achieved at a 2 mg/ml concentration of bR-PM, this concentration was used for the multilayer PLL/bR-PM assembly.

4.3.2 Effect of bR-PM Suspension pH on PLL/bR-PM Assembly

The pH effect of the bR-PM suspensions at the PLL and bR-PM concentrations described above on the photoelectric response was studied to identify the PLL/bR-PM assembly that would provide the best photoelectric response. As shown in Figure 4-5a, the photocurrent amplitude of the PLL/bR-PM bilayer continues to increase as the pH increases from its initial acidic range, with the maximum photocurrent obtained at a pH of 9, at which point it sharply decreases when pH is further increased. Within the range of pH 9 to 12 (the pH tolerance limit of bR-PM, refers to Table 2-1), this decreasing trend continues. Figure 4-5b, which depicts the change of peak light-on photocurrent vs. the pH adjustment, shows that the amplitude of the photocurrent of the

bilayer structure is determined only by the adsorbed amount of bR-PM. Absorbance maxima of the assembly at 564 nm, the characteristic UV-Vis absorption peak of bR-PM, are plotted vs. different pH of bR-PM suspension in Figure 4-5c, reflecting the adsorption amount of bR-PM in the PLL/bR-PM assembly, which strongly accords with the photoelectric response change and indicates that the optimal assembly pH is 9. Since the PLL/bR-PM assembly relies on electrostatic attraction, the assembled amount of bR-PM should be greatly dependent on the surface charge.

In accordance with previous studies (245-246), the charge variation of the assembled component vs. pH can be used to explain the effect of pH of the bR-PM suspension on the photoelectric response. The isoelectric points (PIs) of bR-PM and PLL are from pH 4 to 5 and 9.7, respectively (37, 247). With an increase in the assembly pH from 5 to 9, the negative charge of the bR-PM should increase and the positive charge of the PLL decreases accordingly. The results in Figure 4-5b and c reveal that the charge of bR-PM determines the assembly pH to be less than or equal to 9, possibly due to the fact that the charge of PLL is relatively higher than that of the bR-PM from pH 5 to 9, even during its decreasing mode, which is why the adsorbed bR-PM increases with an increase in its pH. However, when the pH gradually exceeds the PI of PLL (9.7), it is no longer positively charged, leading the bR-PM adsorption to decrease and consequently resulting in a decrease in the photocurrent of the PLL/bR-PM bilayer.
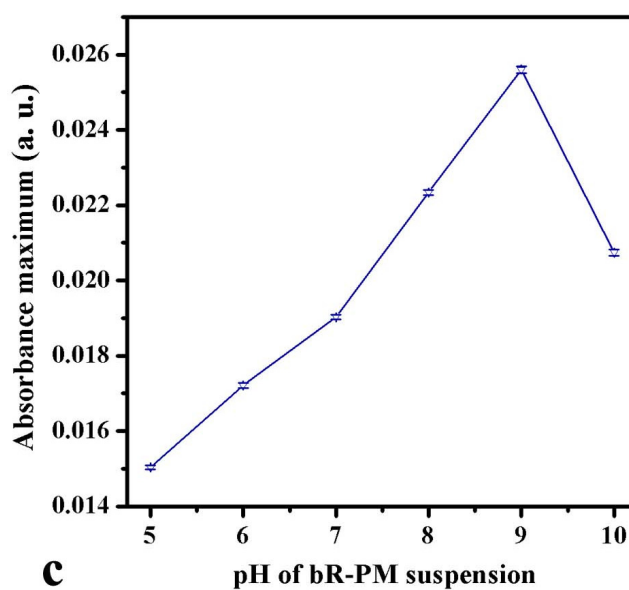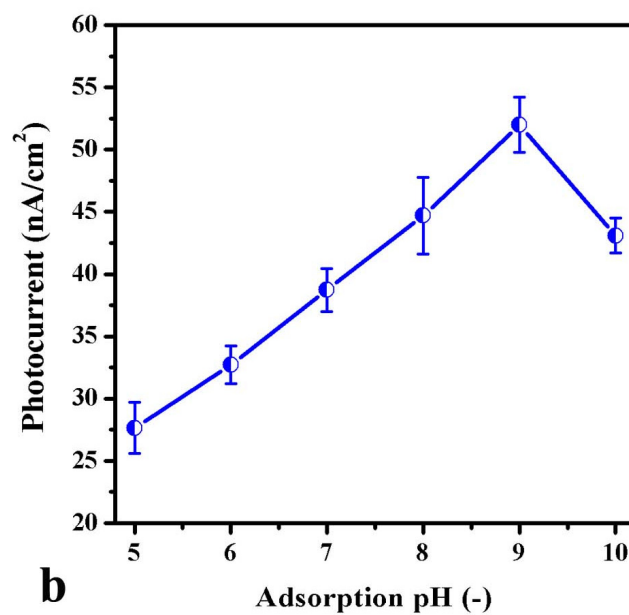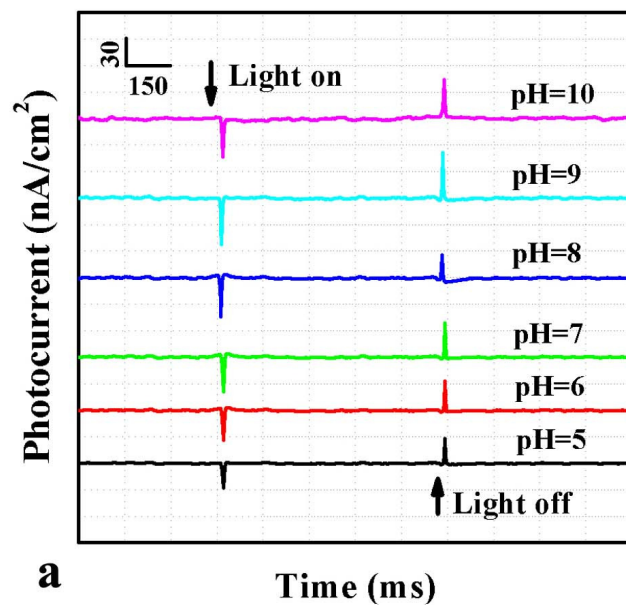
Figure 4-5 (a) Photocurrent profile of PLL/bR-PM bilayers with bR-PM suspensions of different pH levels used. (b) Peak light-on photocurrent with bR-PM suspensions of different pH levels used. (c) Absorbance maxima at 564 nm with bR-PM suspensions of different pH levels used.

4.3.3 Effect of bR-PM Adsorption Time on PLL/bR-PM Assembly
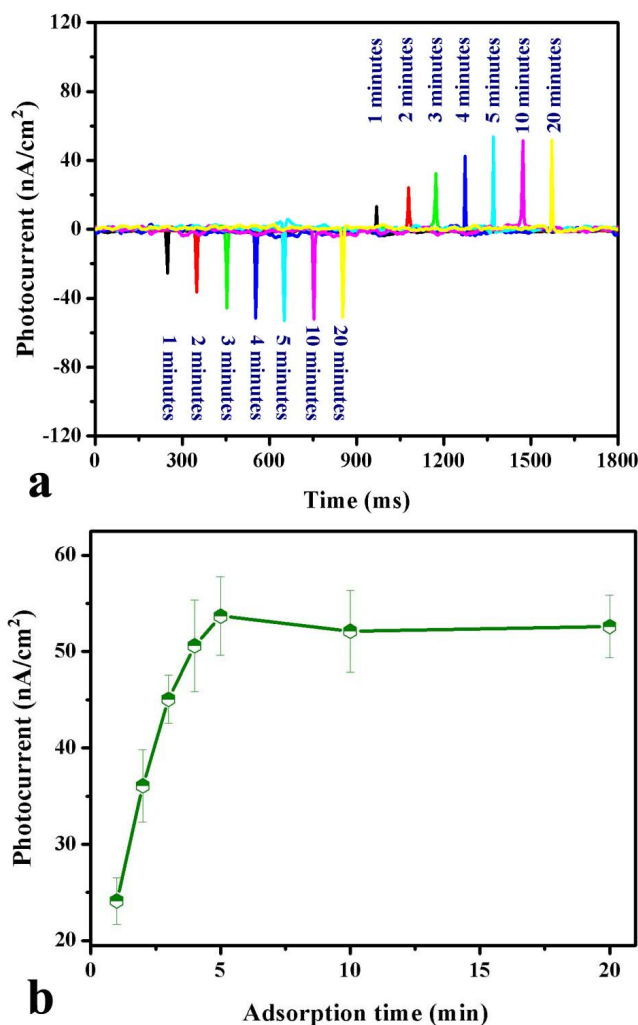
Figure 4-6 (a) Photocurrent profile of PLL/bR-PM bilayers at different adsorption times in bR-PM suspension. (b) Peak light-on photocurrent at different adsorption times in bR-PM suspension.

The effect of bR-PM adsorption time on the photocurrent when both the

PLL and bR-PM suspensions were at the optimal concentrations and pH was

investigated. The experimental results in Figure 4-6 show that the photocurrent sharply increases with an increase in the adsorption time until 5 minutes, when it becomes almost constant, clearly indicating that the bR-PM adsorption achieves full coverage after 5 minutes for the maximum current. As shown in Figure 4-7, which depicts the adsorption process studied by *in-situ* SPR, there is no further angle shift in SPR after 5 minutes adsorption, demonstrating a maximum coverage monolayer has been formed at that point, which strongly accords with the results shown in Figure 4-6b.

4.4 Construction of PLL/bR-PM Multilayer Assembly

The optimal adsorption conditions were applied to construct the multilayer PLL/bR-PM LbL assembly. To generate a high photoelectric response, it is critical to construct a monolayer of oriented bR with no passive pores that could cause short circuits upon illumination (37). Thus, the construction process of the multilayer film was monitored *in situ* using various methods and the photoelectric responses of the built multilayer were investigated.

4.4.1 *In-Situ* SPR Study

The shift in the SPR angle upon adsorption is often studied *in situ* to monitor adsorption process and performance (248-251). This study conducted an *in-situ* investigation of the assembly process of the PLL/bR-PM multilayer to obtain data on the coverage and the adsorption of the bR-PM in the

multilayer assembly. Due to the limited linear range of SPR measurements (252), only the first bilayer was investigated.

Figure 4-7 shows the SPR angle shift caused by each step of the first PLL/bR-PM bilayer formation in the LbL assembly. After measurement of the baseline, a rather small angle shift occurs with the addition of PLL on the substrate at only approximately 100 m° due to the comparatively low molecular weight of PLL. However, the addition of bR-PM leads to a dramatic change in the SPR angle shift ($\Delta\theta$ = 926 m°) because the bR-PM patch has much larger size (up to 5μm) (37) than PLL. Assuming a continuous film is produced, the theoretical $\Delta\theta$ can be calculated using the Fresnel equation for a four-layer system (prism/gold film/PM film/solution) (253). The PM patch is known to have a constant thickness of 5 nm (37). With the known refractive indices (254) of n1 (glass) = 1.518, n2 (gold film@670 nm) = 0.1372 + 3.7852i, d2 = 50 nm, n3 (PM) = 1.532 (255), and n4 (aqueous solution) = 1.334, the theoretical $\Delta\theta$ is calculated to be 1040 m°. Compared with the theoretical $\Delta\theta$ calculated from an ideal full-covered immobilization of bR-PM, i.e., 100% coverage, the actual coverage of bR-PM in the LbL process can be estimated as:

$$\text{coverage} = \frac{\text{actual } \Delta\theta}{\text{theoretical } \Delta\theta} = 89.04\%$$

For large patches such as bR-PM, which has lateral dimensions of up to 5 μm (37), approximate 90 percent is quite high coverage in the LbL method, indicating that PLL is a good polycationic assembler for the LbL film

70
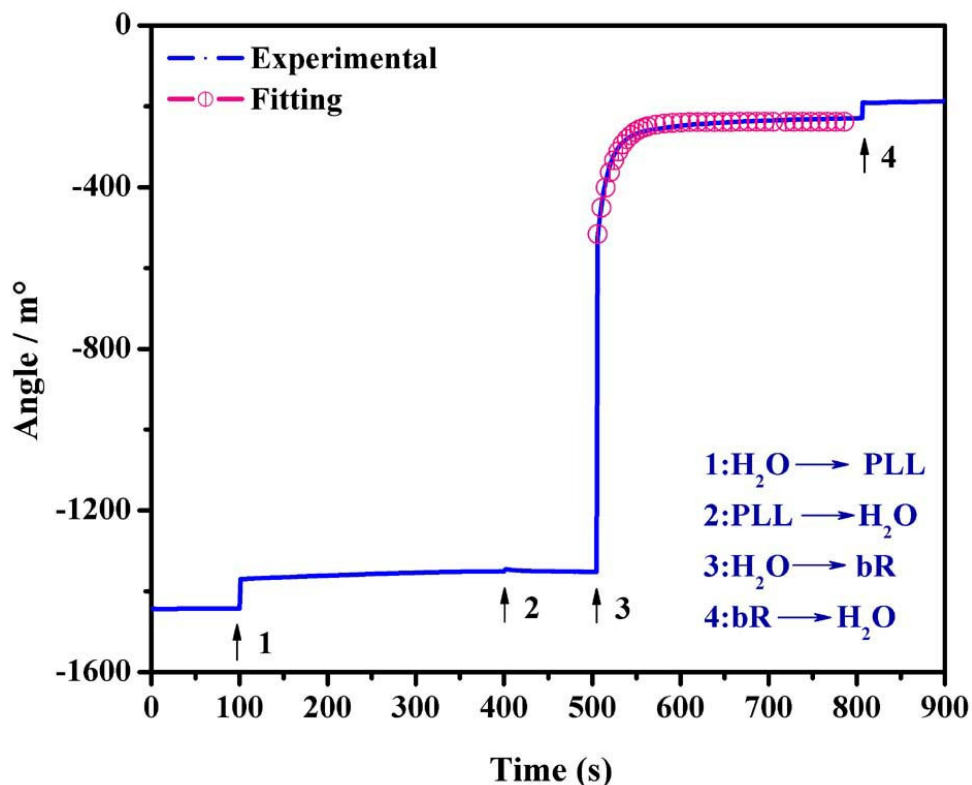
Figure 4-7 *In-situ* scanning SPR binding curve (solid line) and Langmuir adsorption kinetics fitting curve (circles) of the first PLL/bR-PM bilayer adsorption.

construction of the multilayer bR-PM.

Generally, the adsorption behavior of species from a solution of concentration [T] onto an unfilled surface can be expressed in terms of

$$\theta(t) = \theta_{eq}(1 - e^{-(k_a[T]+k_d)t})$$

where t is time, θ_{eq} is the equilibrium value for θ at a particular bulk concentration, K_a is the adsorption coefficient, and k_d is the desorption coefficient (256). Thus the SPR angle shift caused by the adsorption of bR-PM during the bilayer assembly is fitted as shown in the circle curve in Figure 4-7. Comparison of the fitted result with the original *in-situ* SPR response reveals

71

that the bR-PM adsorption dynamics of the PLL/bR-PM multilayer assembly is well in agreement with the Langmuir adsorption kinetics.

The density of adsorbed bR-PM in the PLL/bR-PM multilayer assembly were calculated in terms of increases in the SPR angle between two buffer phases at a ratio of 1 ng/mm^2 per 120 m° (249). From the SPR angle shift $\Delta\theta = 926$ m° caused by the bR-PM addition, the adsorbed density of bR-PM is estimated to be 7.72 ng/mm^2 per bilayer. The SPR result discussed above quantitatively characterizes the bR-PM immobilization process by LbL technique.

4.4.2 AFM Characterization

Evolution in the surface morphology during the PLL/bR-PM multilayer assembly construction was depicted by AFM images. Before polyelectrolyte adsorption, the MUA-modified gold electrode surface (Fig. 4-8a) is rather smooth, with sputtered gold nanoparticles spread uniformly across the surface. After the formation of two PLL/bR-PM bilayers (Fig. 4-8b), dispersion across the whole surface can be observed as large patches with lateral dimensions of approximately 0.5-2 μm, which is in agreement with the reported size of the bR-PM structure (37). The high bR-PM coverage is also consistent with the SPR results. When the number of bilayer increases to 4, 6 and 8, as shown in Figures 4-8c, d and e, respectively, the patch structure of bR-PM becomes more obvious, while small particle structures always appear on the bR-PM patches, a
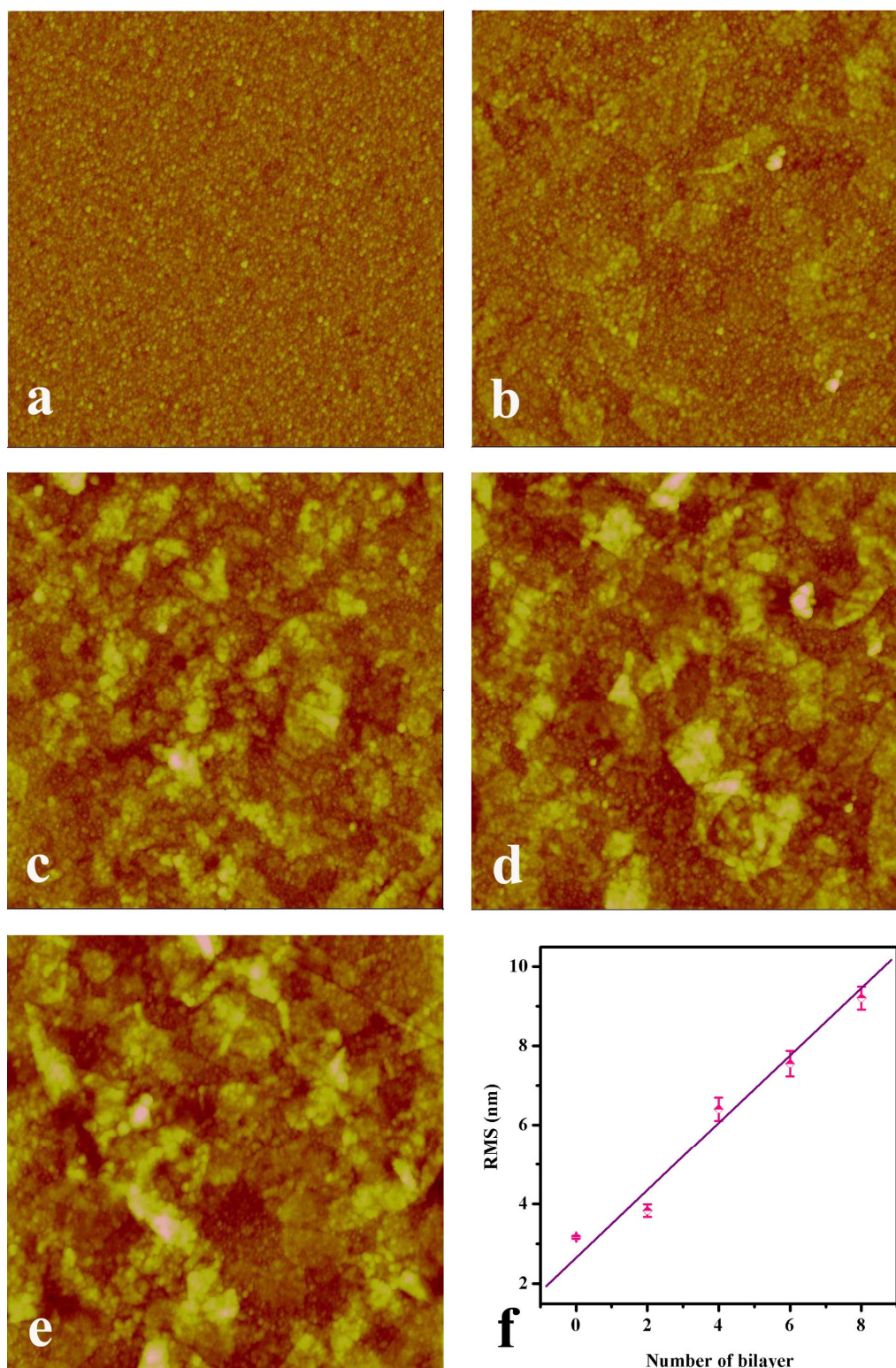
Figure 4-8 AFM topography images of (a) MUA modified gold surface; (b) two bilayers, (c) four bilayers, (d) six bilayers, and (e) eight bilayers of PLL/bR-PM film adsorption with the bR-PM as the outer layer, respectively (all images are of size 5.0 μm×5.0 μm and the maximum z-range is 80 nm). (f) The relationship between roughness and the number of bilayers.

finding consistent with the reported PLL profile resulting from other LbL process (257). The distribution of the PLL dots also illustrates the strong electrostatic attraction between the two polyelectrolytes. RMS changes introduced by growth of the PLL/bR-PM multilayer are plotted in Figure 4-8f, showing that the roughness of the top surface of each multilayer assembly, apparently caused by the patch structure of bR-PM, increases almost linearly as the number of bilayers increases. The linear relation of roughness vs. number of bilayers may indicate that each assembled bR-PM monolayer structure is very reproducible in the multilayered film. Each AFM sample was carefully preserved without any damage after the morphology examination and directly used to conduct the photoelectric measurements.

4.4.3 UV-Vis Analysis

Figure 4-9a shows the different views on the quartz before and after PLL/bR-PM multilayer assembly. Compared to the nearly transparent blank quartz on the left, the quartz on the right exhibits a light purple color, indicating the presence of bR-PM. Figure 4-9b shows the UV-Vis spectra for sequentially assembled PLL/bR-PM multilayer (curves from bottom to top show the absorption spectrum of 2, 4, 6 and 8 bilayers, respectively), indicating both absorption peaks at 278 and 564 nm, the characteristic absorption peaks for bR-PM, the increase of which vs. the number of assembled bilayers is linear (inset of Figure 4-9b), clearly displaying that the adsorbed bR-PM quantitatively
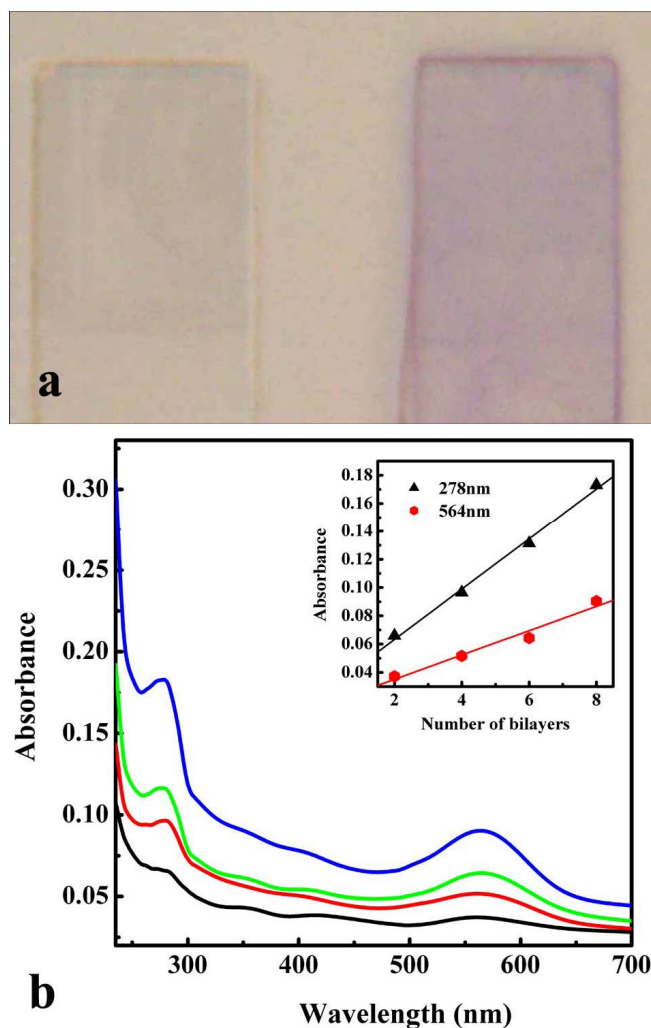
Figure 4-9 (a) Quartz before (left) and after (right) the PLL/bR-PM multilayer assembly. (b) UV-Vis spectra of PLL/bR-PM immobilized quartz (black, red, green and blue curves represent the absorption spectrum of 2, 4, 6 and 8 bilayers, respectively). Inset shows the absorbance at 564 nm and 278 nm, respectively, vs. the number of bilayers.

increases proportionally with the assembled bilayers increases. The UV-Vis result strongly demonstrates that the spontaneous PLL mediated bR-PM adsorption by the LbL technique not only effectively and reproducibly assemble an equal amount of bR-PM onto each bilayer, but also retain its original conformation in terms of the consistent characteristic absorption peaks of bR-PM in different multilayer, a result that strongly agrees with the AFM images.

The absorbance for each bilayer of PLL/bR-PM at 564 nm was calculated to be 1.25×10^{-2} from the slope of the linear fitted result shown in the inset of Figure 4-9b. This absorbance directly reflects the amount of bR-PM adsorption in one bilayer because PLL contributes no absorption in this wavelength range. In comparison to the bR-PM adsorbed through LbL using other polycationic assemblers that has been reported in other studies (168, 170, 228), the absorbance reading of per bilayer obtained in this work is much higher, indicating that PLL can act as a highly positive charged monolayer for better adsorption of bR-PM than those polycationic assemblers reported.

4.5 Photoelectric Response of the PLL/bR-PM Multilayer Assembly

The photocurrent generated from bR-PM under illumination is an important and desirable property for its use in bioelectronic device applications. The typical photoelectric responses of the 2, 4, and 8 bilayers of the PLL/bR-PM assembly are shown in Figure 4-10a. The capacitive photocurrent produced from the PLL-assembled multilayer film in this measurement exhibits the feature identical to those reported in previous studies (127, 146-148, 258). The negative peak (light-on photocurrent) corresponds to turning on the light, while the positive peak photocurrent (light-off photocurrent) corresponds to turning off the light. The result shows that the photocurrent almost linearly increases with an increase in the number of assembled bilayers in the growth of the first

eight bilayers. This indicates that the physiological activity of the bR-PM in the PLL-assembled multilayered structure is well preserved, and thus the photocurrent is simply dependent on the total amount of bR-PM adsorbed in the assembled multilayer film.
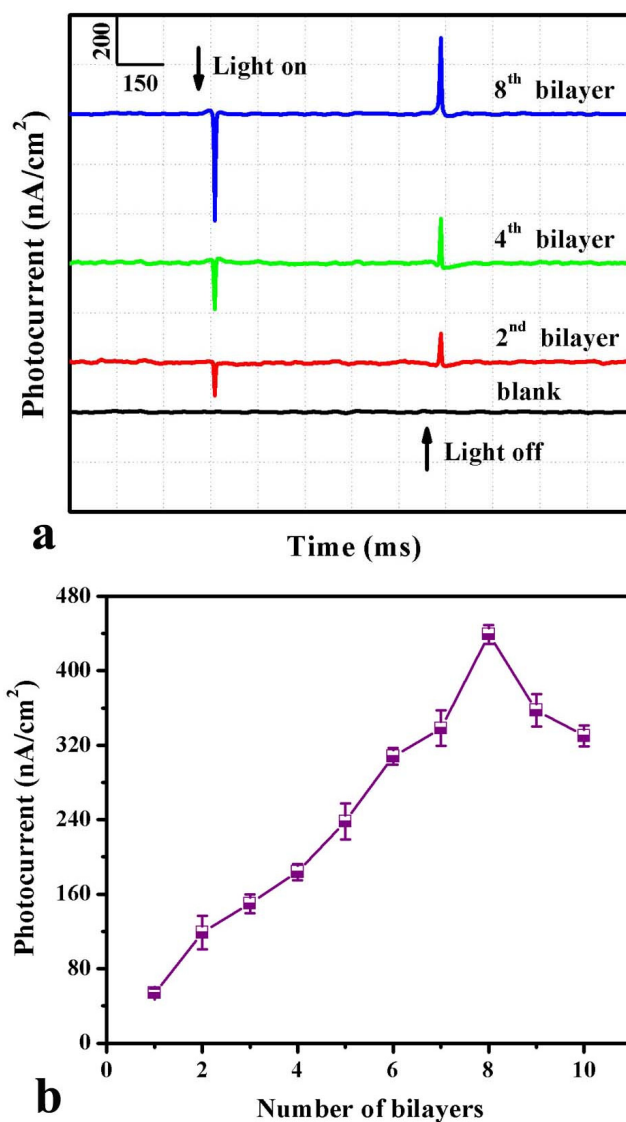
Figure 4-10 (a) Photocurrent response generated by the 2, 4, and 8 bilayers of the PLL/bR-PM assembled under optimal parameters. (b) Peak light-on photocurrent at different bilayers of PLL/bR-PM LbL assembly.

However, as the number of bilayers adsorbed surpasses eight, the photocurrent starts to decline (Fig. 4-10b). Previous studies have explained that the increased resistance of other polycation-assembled multilayer films with the increase in the number of bilayers results in a decreased photocurrent (168, 170, 228). There might be another reasonable explanation that the decrease in photocurrent after reaching a certain thickness is caused by the increased diffusion resistance of protons, as the capacitive photocurrent is generated from the built proton gradient by the proton pumping of bR-PM under illumination, which is directly related to the proton diffusion process.

The photocurrent generated by a bR-PM multilayer film constructed using the LbL technique could reach 420 nA/cm^2 when the number of PLL/bR-PM bilayers increases to eight, which is higher than the photocurrent generated from LbL bR-PM films assembled by other polycationic assemblers in previous reports (168, 170, 228) (data corresponding to incident green light of a power density at 20 mW/cm^2 are compared in Table 1). This result, together with the results regarding the amount of adsorption derived from UV-Vis spectra (refer

Table 4-1 Comparison of the maximum photocurrent generated by bR-PM/polycation multilayer assembly with different polycationic assembler used.

Polycations used in the assembly	PDAC	PAH	PEI	PLL
Maximum photocurrent (nA/cm^2)	~ 116	~ 10*	~ 293	~ 420

 * Only the power density of white light was provided in the literature.

 to section 4.4.3), indicates that PLL is a superior assembler in LbL construction of a bR-PM based multilayer film with high photoelectric response.

4.6 Conclusion

This chapter described the successful construction of a well-oriented PLL/bR-PM multilayer film through electrostatic adsorption using the LbL assembly technique. The UV-Vis absorption spectrum demonstrates that the natural conformation of bR-PM is properly preserved after its construction into a multilayer structure and confirmed that the assembling process of each PLL/bR-PM bilayer is highly reproducible, with the amount of bR-PM adsorption linearly increasing as the number of bilayers increased. The *in-situ* SPR monitoring reveals that in the multilayer film growth, the amount of bR-PM adsorption strongly accords with Langmuir adsorption kinetics, and verifies that the coverage of the bR-PM monolayer in the multilayer film could reach as high as 90%. The amount of bR-PM adsorbed in the film is also calculated from the SPR results. AFM characterization proves that the patch structure of bR-PM remained well in the PLL/bR-PM multilayer and that its roughness linearly increases with an increase in the number of bilayers. The results of the optimization of various LbL assembly parameters indicate that PLL functions as a favorable polycation for the electrostatic LbL assembly of bR-PM that significantly enhances the bR-PM photoelectric response.

Chapter 5 Enhancement of bR Photoelectric Response Using Multilayered $WO_3 \cdot H_2O$ Nanocrystals/PVA Membrane [b]

5.1 Introduction

Enhancing the photoelectric response of a bR-based system is essential for bR bioelectronic applications, but has proven very challenging. Various methods, such as chemically induced enhancement (221) and LbL enhancement (259) have been investigated. Nanomaterials possess unique properties due to their small size that may prove very beneficial in bioelectronic applications (260-261). Several nanomaterials have been incorporated into bR to either increase the amplitude (262) or change the pattern (263) of its photoelectric responses.

Due to their spillover effect, $WO_3 \cdot H_2O$ nanocrystals have been recently employed to improve the performance of the proton exchange membrane in fuel cells (264). However, application of $WO_3 \cdot H_2O$ nanocrystals in a biomolecule-based system had never been investigated before. Since the photoelectric

---

[b] Reproduced by permission of The Royal Society of Chemistry.
http://www.rsc.org/publishing/journals/CC/article.asp?doi=b923354g

response of bR originates from the protein's unique proton translocation, it would be expected to be enhanced by the effective proton spillover of $WO_3 \cdot H_2O$ nanocrystals. The challenge is how to build integrated membrane and have the effective spillover process. In this work, the precursor of $WO_3 \cdot H_2O$ nanocrystals was incorporated into a PVA matrix to form a mixture that can ensure the $WO_3 \cdot H_2O$ nanocrystals distribution as well as their contact with bR and the effect of the $WO_3 \cdot H_2O$/PVA membrane on the bR photoelectric response was subsequently investigated.

5.2 Preparation of the Integrated Membrane

5.2.1 $WO_3 \cdot nH_2O$ Nanocrystal Precursor Preparation

The preparation of the $WO_3 \cdot nH_2O$ nanocrystal precursor was based on a protocol slightly modified from that reported by Habazaki (265) and Yang (264). 5 ml H_2O, 10 ml 30% H_2O_2, and 5 ml IPA were combined to render a uniform solution before 1 g of tungsten powder was mixed with the solution. The reaction solution was kept steadily until the tungsten powder completely dissolved. Excessive H_2O_2 was removed by dipping a platinum black-coated Pt foil into the solution to prevent further oxidation, and excessive IPA was removed by vacuum distillation at room temperature with a rotary evaporator to prevent possible harm to bR components during integrated membrane preparation.

5.2.2 Integrated Membrane Electrode Preparation

A 5 mg/ml suspension of bR-PM was prepared before use. EPS method (146-148) was used to uniformly immobilize the bR-PM with favorable orientation on a piece of gold electrode.

2 ml of the as-prepared $WO_3 \cdot nH_2O$ nanocrystal precursor was mixed with 6 ml of the 66.67 mg/ml PVA solution, and then spin-coated on a freshly prepared bR-modified electrode. The thickness of the $WO_3 \cdot nH_2O$ precursor/PVA layer was tailored by repeated spin-coating, followed by one hour of heating at 60 ℃ to allow formation of the integrated $bR/WO_3 \cdot nH_2O/PVA$ membrane. $WO_3 \cdot nH_2O/PVA$ membrane and bR/PVA membrane were also prepared as controls.

5.3 Characterization of the Integrated Membrane

5.3.1 Surface Morphology Characterization

Figure 5-1a shows that the surface morphology of the as-prepared $WO_3 \cdot nH_2O/PVA$ membrane examined by FESEM is smooth with no obvious protuberances. The cross-section of the $WO_3 \cdot nH_2O/PVA$ membrane prepared by 12 episodes of spin-coating (Fig. 5-1b) illustrates that the thickness of the $WO_3 \cdot nH_2O/PVA$ membrane is relatively consistent.
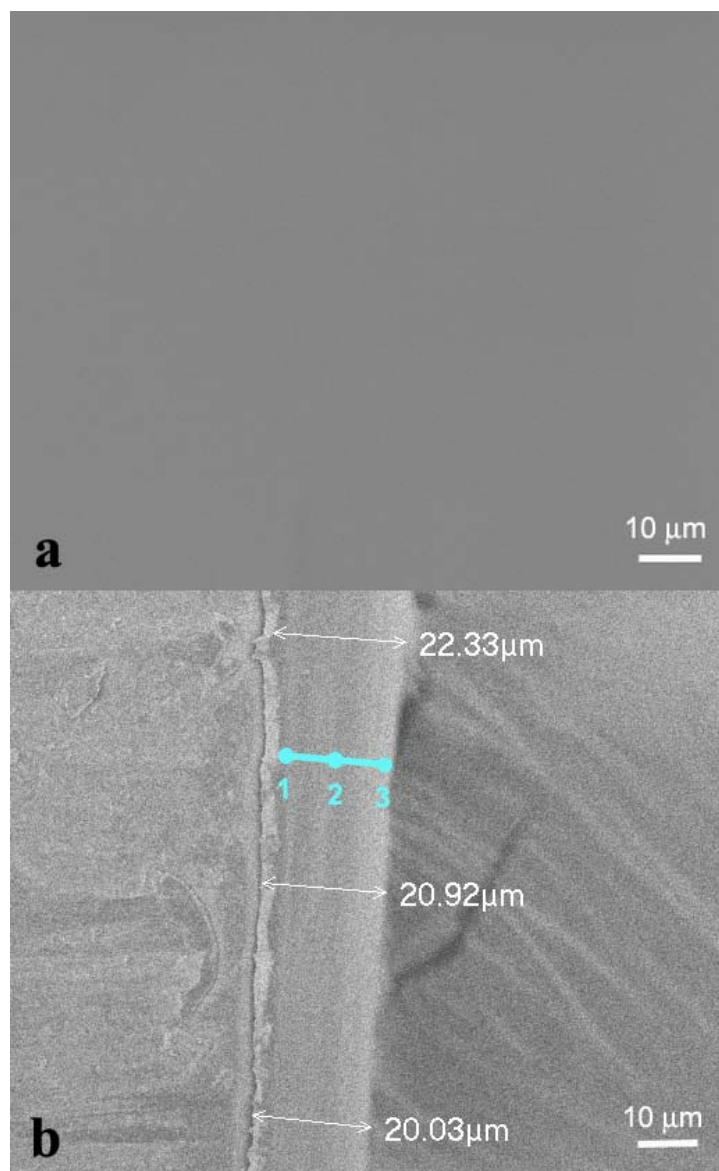
Figure 5-1 SEM micrographs of (a) the surface and (b) cross-section of the WO$_3$•nH$_2$O/PVA membrane.

5.3.2 Determination of Element Distribution

The distribution of the tungsten element across the WO$_3$•nH$_2$O/PVA membrane was investigated. The EDX mapping corresponding to the surface of the membrane (Fig. 5-1a) is presented in Figure 5-2a and the EDX spectra corresponding to the measured points shown in the membrane cross-section

(Fig. 5-1b) is shown in Figure 5-2b. These results together demonstrate that the tungsten element uniformly distributes across both directions of the $WO_3 \cdot nH_2O$/PVA membrane.
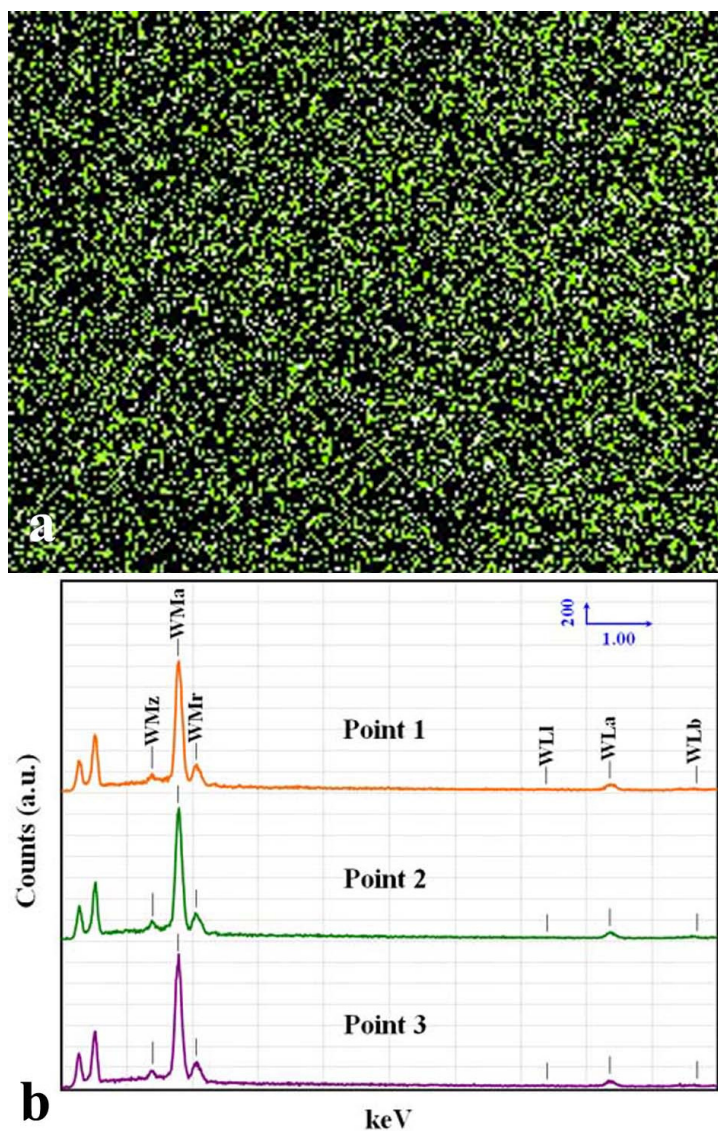
Figure 5-2 (a) EDX mapping along the surface and (b) EDX spectra along the cross-section of the $WO_3 \cdot nH_2O$/PVA membrane.

5.3.3 Microstructure Examination

HRTEM was conducted to study the microstructure of the $WO_3 \cdot nH_2O$ embedded in the PVA membrane. Figure 5-3a clearly shows that $WO_3 \cdot nH_2O$ nanocrystals with diameters of 3~5 nm were spatially stacked in the PVA
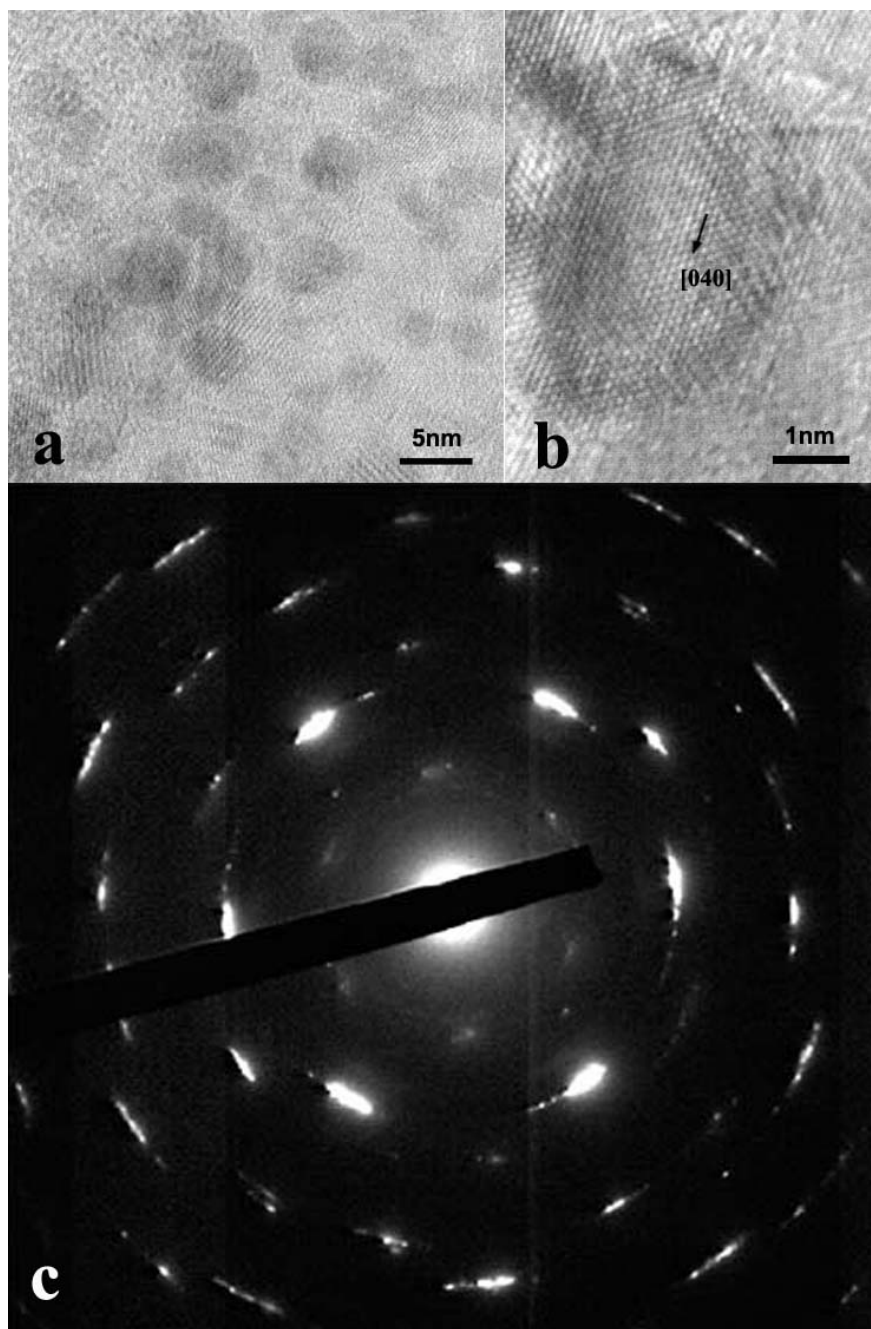
Figure 5-3 HRTEM image at (a) low magnification and (b) high magnification, and the (c) SAED pattern of the $WO_3 \cdot nH_2O$/PVA membrane.

membrane. As shown in Figure 5-3b, the crystal lattice spacing of $WO_3 \cdot nH_2O$

is measured to be d=0.27$\pm$0.01 nm, corresponding to the interplanar spacing of

(040) plane of the standard WO_3 hydrate (JCPDS, card No.: 20-1806). The

selective area electron diffraction (SAED) pattern in Figure 5-3c displays non-

continuous rings composed of diffraction spots, which further confirms the

poly-crystalline nature of the nanocomposite membrane.

5.3.4 Identification of Crystal Structure

The crystal structure of the $WO_3 \cdot nH_2O$/PVA membrane was characterized

by XRD. Figure 5-4 shows three relatively sharp peaks in curve II, two of

which (2θ=25.63° and 2θ=33.44°) can be indexed to (111) and (040) reflection,
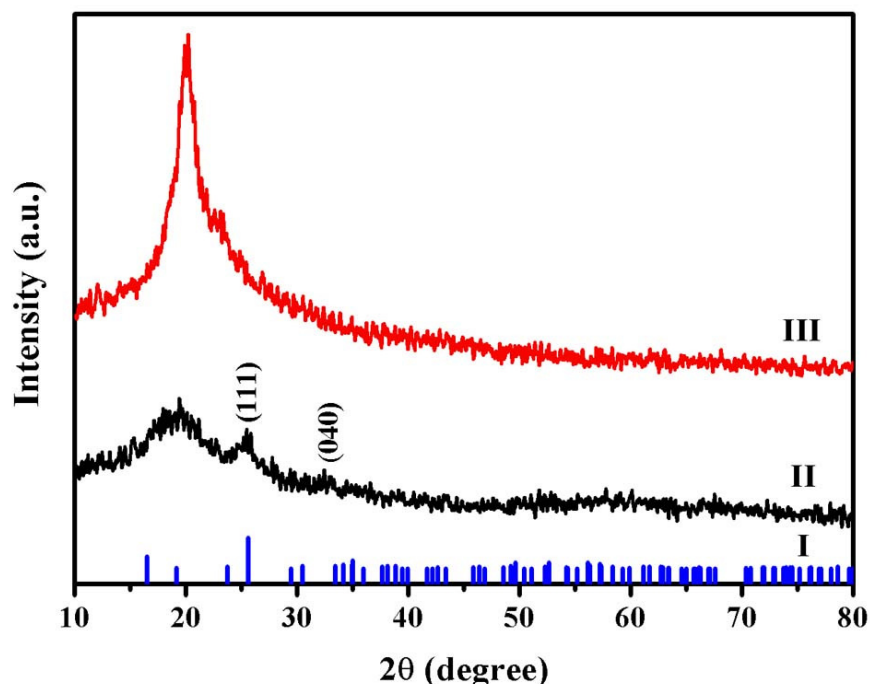
Figure 5-4 XRD patterns of (I) the standard values of tungsten oxide hydrate (JCPDS 20-1806), (II) $WO_3 \cdot nH_2O$/PVA membrane, and (III) plain PVA membrane.

respectively, of the tungsten oxide hydrate (I, JCPDS, card No.: 20-1806), suggesting that the hydrate of WO_3 forms during the preparation of the membrane. Another prominent peak ($2\theta=19.42°$) could be ascribed to the PVA component, which shifts slightly from the main peak ($2\theta=20.22°$) in the XRD pattern of PVA (curve III) due to the change in concentration. As no characteristic peaks of impurities are observed, the prepared membrane is confirmed to be a PVA/WO_3 hydrate hybrid. Using the Scherrer Formula (266), the crystallite size of the WO_3 hydrate is calculated to be ~3.0 nm, which is highly consonant with the previous HRTEM observation.

5.3.5 Determination of Thermal Properties

The thermal properties of the $WO_3 \bullet nH_2O$/PVA membrane was determined by TGA. The TGA profile for the $WO_3 \bullet nH_2O$/PVA membrane in Figure 5-5 shows an weight loss of ~7% at approximately 200 ℃, which is due to the evaporation of the occluded water, followed by a second sharp weight loss of ~5% at approximately 250 ℃, which is likely due to the loss of chemically combined water in the WO_3 hydrate. The TGA curve section of PVA (inset) is rather flat between 200 ℃ and 300 ℃, indicating that there is no decomposition of the polymer in that temperature range. The third sharp weight loss of ~6% occurs between 250 ℃ and 440 ℃, which is consistent with the obvious weight loss of ~83% between 320 ℃ and 550 ℃ in the TGA curve of PVA (inset), demonstrating the decomposition of the PVA component in the $WO_3 \bullet nH_2O$/PVA membrane.

From the TGA result, the number of the chemically combined water molecules is calculated to be 1, indicating that the WO_3 hydrate should be denoted as $WO_3 \cdot H_2O$. The abundant water in the hydrated WO_3 has great significance in maintaining the moisture of the integrated membrane to attain higher stability (264) and a better proton transport environment (267) in the integrated membrane.
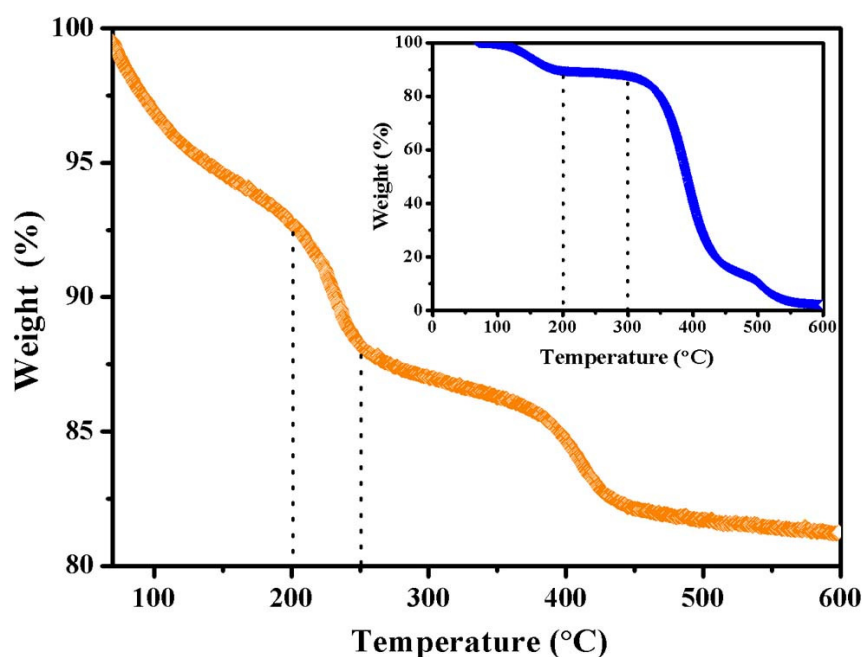
Figure 5-5 TGA curves of the $WO_3 \cdot nH_2O$/PVA membrane. Inset shows the TGA curves of the PVA membrane.

5.4 Effects of Preparation Conditions on the Photoelectric Response

Utilizing the $WO_3 \cdot H_2O$ proton-spillover effect to obtain an enhanced photoelectric response from the integrated $bR/WO_3 \cdot H_2O$/PVA membrane is the ultimate goal of this study. To attain this objective, it is necessary to investigate related factors that might have a significant effect on the photoelectric response.

This section describes the preparation time of the $WO_3 \cdot H_2O$ precursor, the ratio of the $WO_3 \cdot H_2O$ precursor used in the membrane preparation, and the formation time of the $WO_3 \cdot H_2O$ nanocrystals used to optimize the membrane composition and thus obtain the highest photoelectric response from the integrated $bR/WO_3 \cdot H_2O/PVA$ membrane.
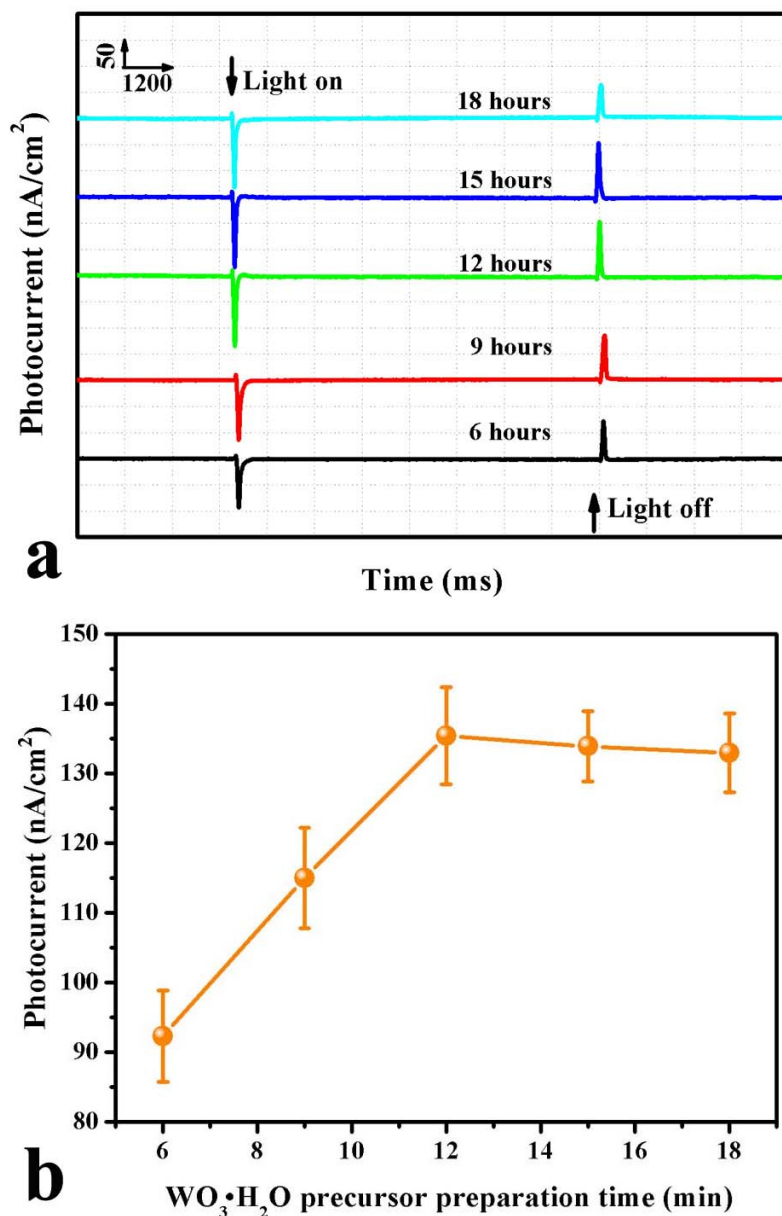
Figure 5-6 Effect of the preparation time of the $WO_3 \cdot H_2O$ precursor on the photocurrent of the integrated $bR/WO_3 \cdot H_2O/PVA$ membrane.

5.4.1 Effect of WO$_3$•H$_2$O Precursor Preparation Time

The photocurrent of the integrated bR/WO$_3$•H$_2$O/PVA membrane containing one layer of WO$_3$•H$_2$O/PVA coating was investigated at the WO$_3$•H$_2$O precursor preparation times of 6, 9, 12, 15, and 18 hours, respectively. Figure 5-6 shows that 12 hours can be regarded as the critical point of the preparation time, at which the dissolving of tungsten powder has been completed thoroughly and no more WO$_3$•H$_2$O precursor will be generated even the preparation time is longer; at preparation times longer than 12 hours, the amplitudes of the photocurrent generated by the integrated membrane containing the WO$_3$•H$_2$O precursor do not increase at all, while the amplitudes attained at preparation times shorter than 12 hours are insufficient for application.

5.4.2 Effect of WO$_3$•H$_2$O Precursor Ratio

The ideal ratio of the WO$_3$•H$_2$O precursor to PVA for obtaining the best photoelectric performance from the integrated membrane was investigated. The results of using a series of ratios of the integrated membrane with one layer of WO$_3$•H$_2$O/PVA coating and the resulting photocurrents were investigated.

As shown in Figure 5-7, when the ratio of the WO$_3$•H$_2$O precursor to PVA is 1 g (calculated by the original mass of the W powder) to 6 ml, the final photocurrent of the integrated membrane is the highest among all the samples. This finding indicates that having too few WO$_3$•H$_2$O nanocrystals in the membrane insufficiently enhance the photocurrent while too little PVA might cause non-uniform or unstable membrane formation, leading to a lack of WO$_3$•H$_2$O
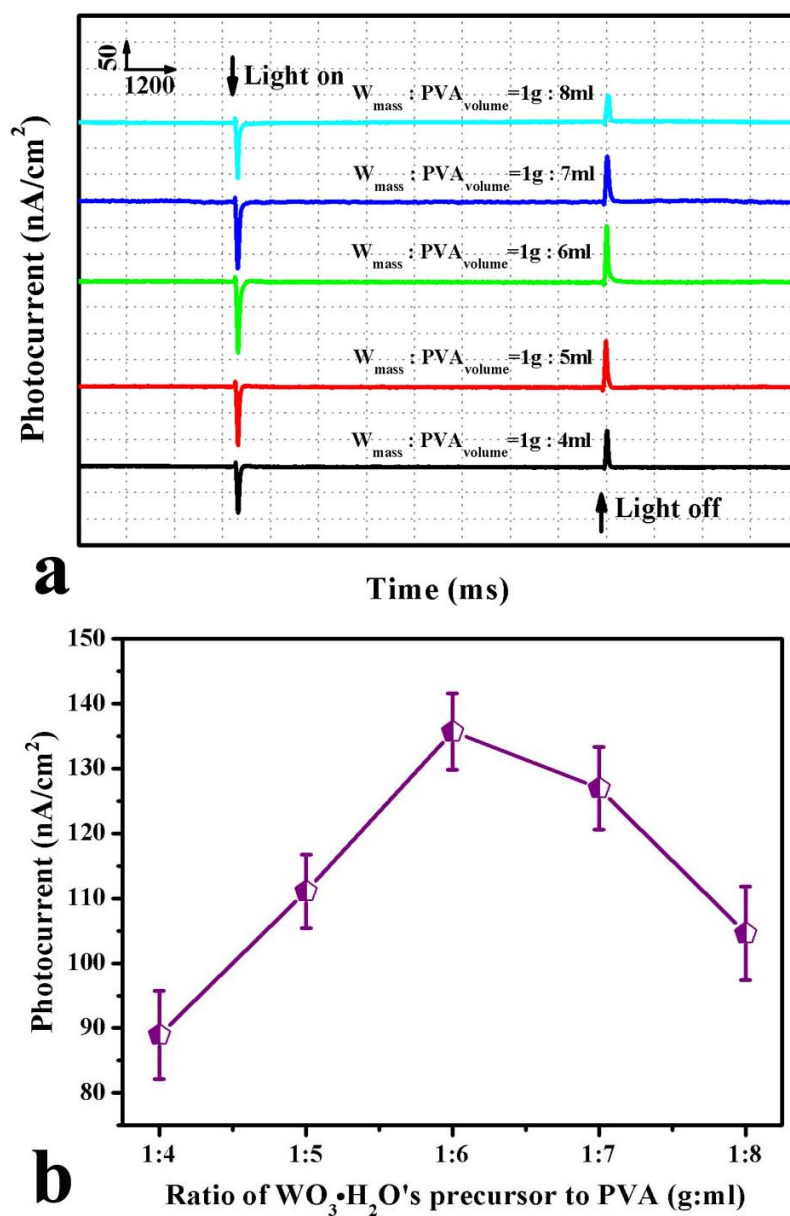
Figure 5-7 Effect of the ratio of $WO_3 \cdot H_2O$'s precursor to PVA on the photocurrent of the integrated $bR/WO_3 \cdot H_2O/PVA$ membrane.

nanocrystal integration with other components in the integrated membrane so that the photocurrent could not be enhanced so obvious as that when the formation of the membrane is well controlled under an optimal ratio of $WO_3 \cdot H_2O$ precursor to PVA at 1g to 6 ml.

5.4.3 Effect of WO$_3$•H$_2$O Nanocrystals Formation Time

Although bR is known to be more thermal-resistant than normal proteins, it is not recommended to expose bR to temperatures higher than 50 ℃ (the temperature of its ecological niche) unless necessary. However, the formation of WO$_3$•H$_2$O nanocrystals from their precursors requires heating at a temperature of at least 60 ℃, which makes the heating time a very important parameter in making an integrated membrane that retains bR activity and biological functions. Another reason why the heating process must be considered is that transparent WO$_3$•H$_2$O nanocrystals can be accelerated to form non-transparent tungsten bronze by high-temperature environment, which might later block the irradiation onto the bR component, and thus affect the photoelectric performance of the integrated membrane.

Using the same ratio of WO$_3$•H$_2$O precursor to PVA (1 g: 6 ml), a formation-time dependent study of the photocurrent of the one-layer WO$_3$•H$_2$O/PVA-coated bR integrated membrane was conducted. Figure 5-8 shows that formation time of either shorter or longer than 60 minutes result in smaller amplitudes in the photocurrent of the integrated membrane. During the brief time in which the WO$_3$•H$_2$O nanocrystals are in the process of formation, the enhancement of the photocurrent are less than that obtained from sufficiently formed WO$_3$•H$_2$O nanocrystals after 60 minutes of heating. Both the reasons mentioned above might play a role in the decrease in photocurrent for formation times longer than 60 minutes, which is determined to be the optimal WO$_3$•H$_2$O nanocrystal formation time.
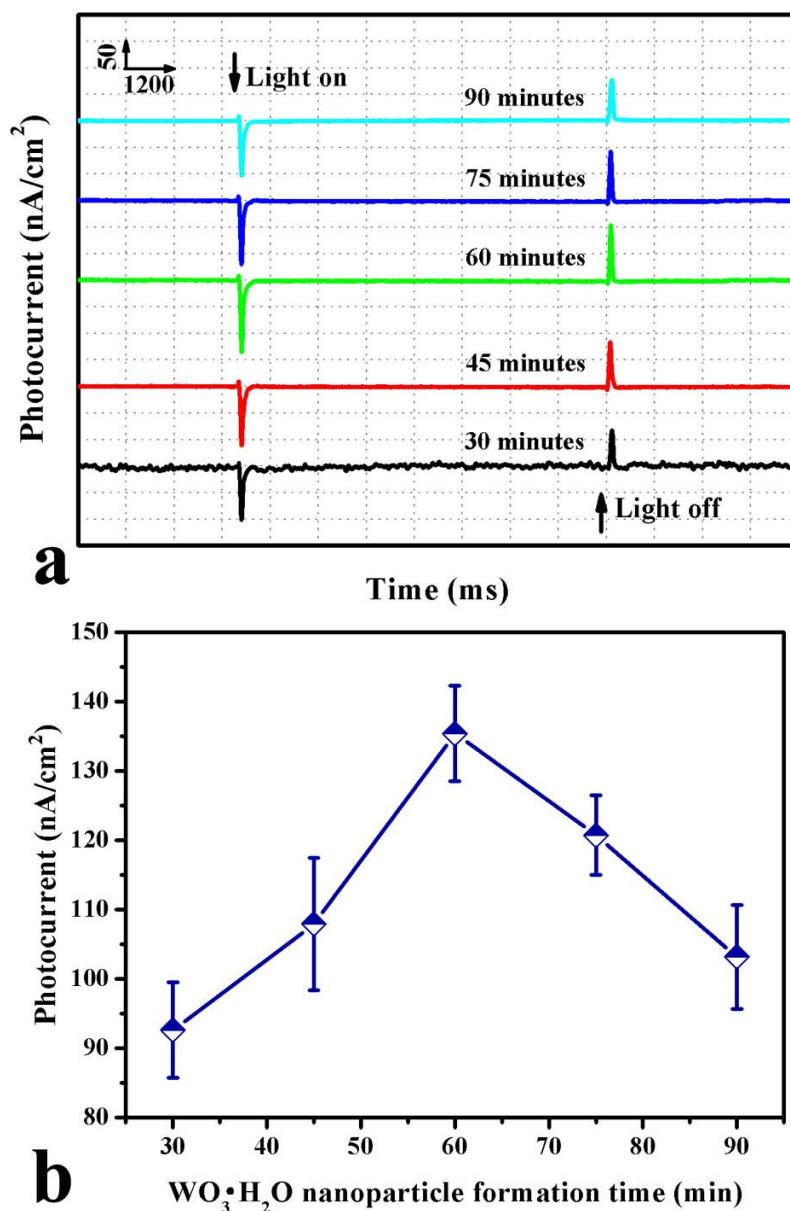
Figure 5-8 Effect of the formation time of $WO_3 \cdot H_2O$ nanocrystals on the photocurrent of the integrated bR/$WO_3 \cdot H_2O$/PVA membrane.

5.5 Photoelectric Responses of Integrated Membrane with Different Compositions

The effect of the number of $WO_3 \cdot H_2O$/PVA layers on the photoelectric responses of the integrated bR/$WO_3 \cdot H_2O$/PVA membrane are illustrated in Figure 5-9. Initially, both the photocurrent (Fig. 5-9a) and photovoltage (Fig. 5-

9b) responses of the integrated bR/WO$_3$•H$_2$O/PVA membrane increase proportionally with the increase in the number of coated WO$_3$•H$_2$O/PVA layers on top of the bR layer. However, after the photoelectric response reaches the maximum at ~20 μm thickness of the multilayered WO$_3$•H$_2$O/PVA membrane, which corresponds to 12 spin-coated single layers, it decreases with a further increase in the number of modified layers.

The photoelectric responses of the integrated bR/WO$_3$•H$_2$O/PVA membrane demonstrate a capacitive nature (signal II in Fig. 5-10) identical to that generated by pure bR (signal I in Fig. 5-10) due to the proton-pumping effect (263). Figure 5-10a and 5-10b depict the typical responding photocurrent and photovoltage profiles for membranes consisting of different components, showing that both the photocurrent and photovoltage responses of the integrated bR/WO$_3$•H$_2$O/PVA membrane (signal II in both figures) are enhanced to be approximately six times more than that of pure bR (signal I in both figures). However, the PVA/bR membrane without the WO$_3$•H$_2$O component (signal III in both figures) does not generate obvious enhancement of the bR photoelectric response (signal I) in comparison to the integrated bR/WO$_3$•H$_2$O/PVA membrane with the same thickness (signal II). In addition, the WO$_3$•H$_2$O/PVA membrane without bR cannot produce any photoelectric response under the same experimental conditions (signal IV in both figures). All these results clearly indicate that the WO$_3$•H$_2$O nanocrystals in the integrated bR/WO$_3$•H$_2$O/PVA membrane are the only factor that dramatically boost the bR photoelectric response.
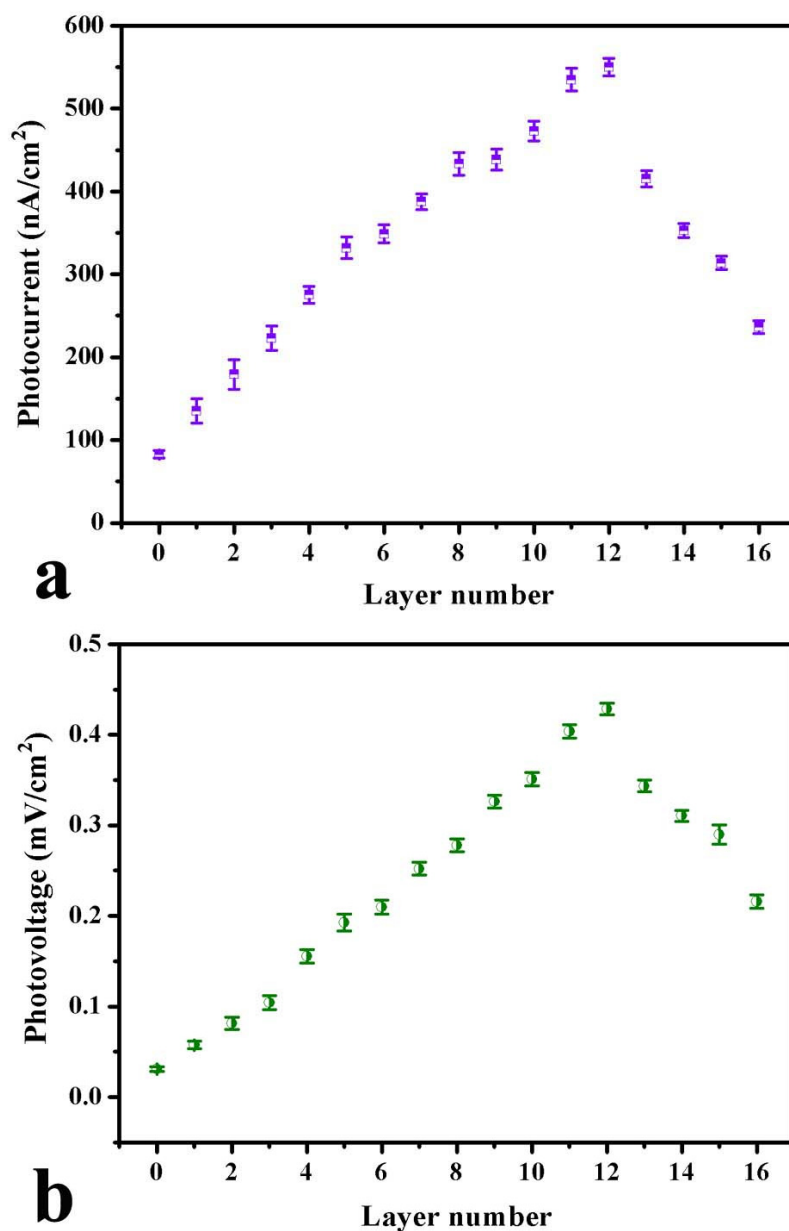
Figure 5-9 Effect of the layer numbers of $WO_3 \cdot H_2O/PVA$ on the photocurrent of the integrated $bR/WO_3 \cdot H_2O/PVA$ membrane.

The photoelectric responses of the integrated membrane exhibit a significantly longer decay time (Fig. 5-11) than that of the pure bR film, suggesting that the longer neutralization time of the polarization is caused by the larger proton gradient formed by the proton transport in the integrated system (146-148).
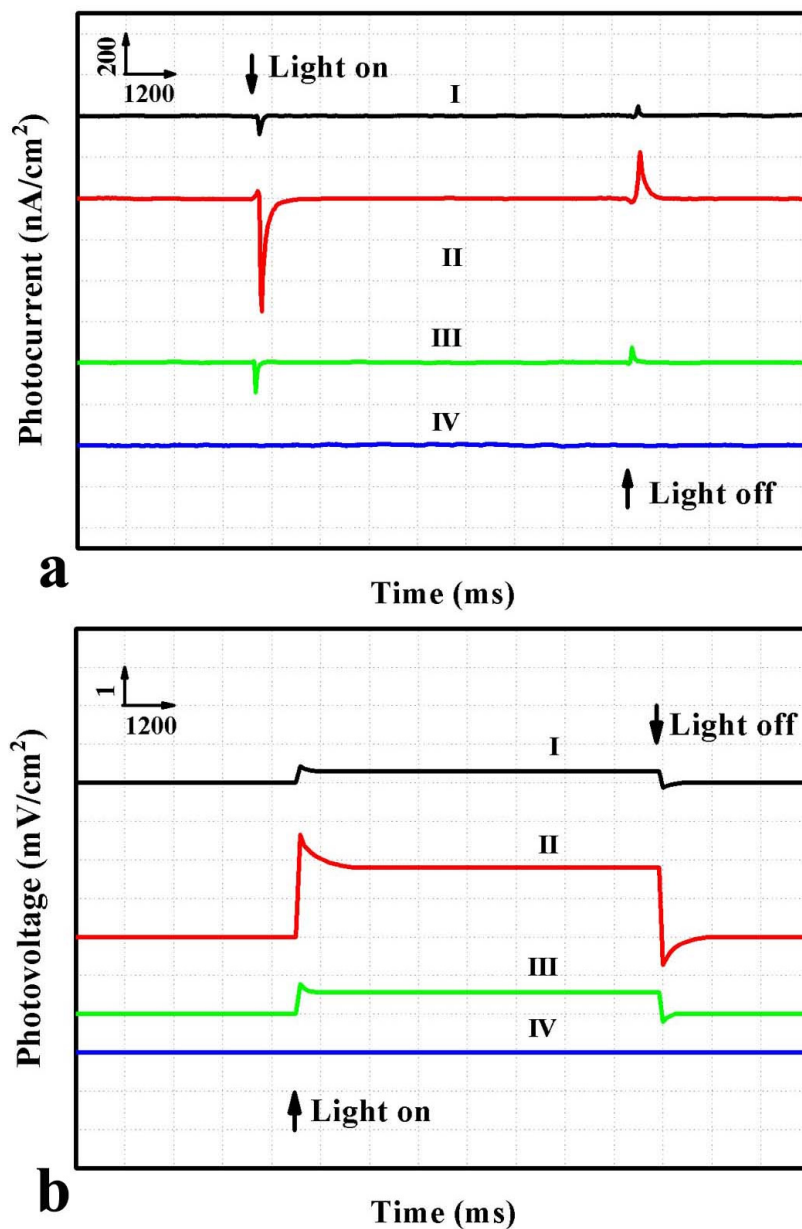
Figure 5-10 Photoelectric responses of the bR/WO$_3$•H$_2$O/PVA membrane. (a) Photocurrent and (b) photovoltage of (I) pure bR, (II) bR integrated with 12 layers of WO$_3$•H$_2$O/PVA component, (III) bR integrated with 12 layers of PVA component, and (IV) 12 layers of WO$_3$•H$_2$O/PVA membrane alone.

5.6 Mechanism for Photoelectric Enhancement

To understand the fundamental insight of the photoelectric enhancement is very important. It is known that WO$_3$•H$_2$O can perform hydrogen spillover to
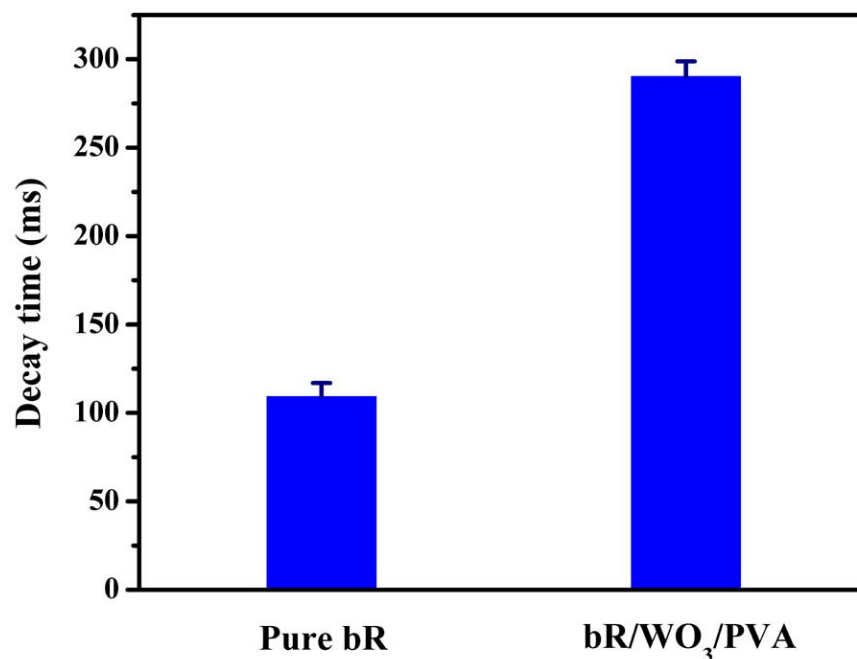
Figure 5-11 Decay time comparison of photocurrents generated by pure bR and bR/WO$_3$•H$_2$O/PVA integrated membrane.

produce protons (268-269), during which the color of WO$_3$•H$_2$O changes from light yellow to dark yellow showing the formation of hydrogen tungsten bronze, which is the direct index of the hydrogen spillover (269). In this work, the color change of WO$_3$•H$_2$O/PVA membrane in photoelectric experiment with the bR presence was much faster than that without bR, possibly evidencing that bR-introduced electric field could strengthen the hydrogen spillover process.

A mechanism based on the light-driven proton pumping of bR associated with the hydrogen spillover of WO$_3$•H$_2$O nanocrystals is therefore proposed, as shown in Figure 5-12. When green light irradiates the integrated membrane, protons in the interface between the bR film and the gold electrode are pumped out by bR molecules to produce capacitive current while build a local electric

field vertical to the membrane to trick the hydrogen spillover (268) of $WO_3 \cdot H_2O$ nanocrystals and produce protons, which would move away from the electrode in the same manner as the protons pumped out from the bR. This larger amount of moving protons increases the potential gradient in the double layer structure of the electrode for a higher photoelectric current. Due to this
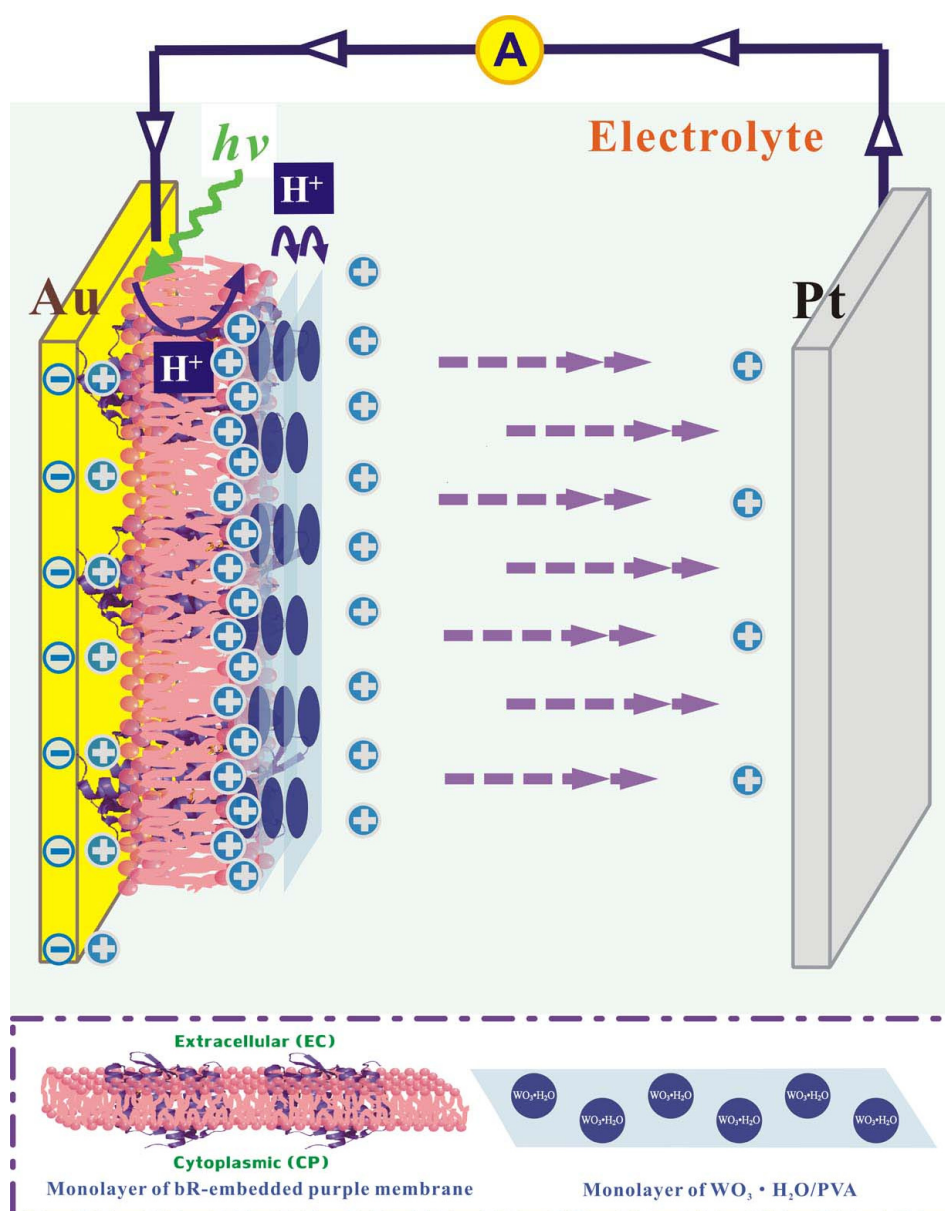
Figure 5-12 (a) Model of the photoelectric response generation of the integrated $bR/WO_3 \cdot H_2O/PVA$ membrane, (b) monolayer of bR-PM, and (c) monolayer of $WO_3 \cdot H_2O/PVA$ component.

reason the photoelectric response is proportional to the number of $WO_3 \cdot H_2O$/PVA layers in the integrated membrane within a certain range. However, when the number of $WO_3 \cdot H_2O$/PVA layers increases to above 12, the photoelectric response decreases, possibly due to increased resistance in the thick film (Fig. 5-9).

5.7 Conclusion

Construction of a multilayered $WO_3 \cdot H_2O$/PVA membrane on bR increases the bR photoelectric response approximately six fold. The mechanism behind the photoelectric enhancement may be the $WO_3 \cdot H_2O$ hydrogen spillover process. This finding may lead to the development of a method of significantly enhancing the bR photoelectric signal in bioelectronic devices, rendering a promising proton-exchange membrane for biofuel cell applications.

Chapter 6 Stationary Current Generated from Photocycle of a Hybrid bR/QDs Bionanosystem [c]

6.1 Introduction

Due to its direct relevance to bR photoelectric properties, the bR photocycle has been studied extensively over the past 30 years. UV-Vis (270), FTIR (75), resonance Raman spectroscopy (271), solid-state NMR (272), and x-ray crystallography (273) have been employed to contribute detailed information regarding the structural changes in and provide insight into the mechanism of the photocycle. Several studies (274-275) have characterized individual intermediates in the photocycle (274-275)(274-275)(274-275)(274-275)and investigated the photoelectric signal of wild-type bR and different genetically engineered bR mutants under different types of illumination (127, 276). Among these studies, stationary photocurrents have been obtained with addition of protonophore 1799 into several of bR mutants with blue-light illumination (277). However, due to the fixed photocycle of wild-type bR, no stationary current excited by only one wavelength external illumination has been produced to date.

_____

[c] Reprinted in part with permission from [Li, R., C. M. Li, et al. **2007**. *Appl. Phys. Lett.* 91:223901] Copyright [2007], American Institute of Physics.

QDs are photostable, color-tunable semiconducting nanocrystals with a wide absorption spectrum and a narrow emission peak. CdTe nanocrystals with different sizes have tunable emissions from green to red due to quantum confinement (278). When the diameter of CdTe QDs is 2 to 3 nm, they can emit fluorescence of around 530 nm by excitation from light source with higher energy. For example, if a 410 nm light source is applied to excite them, CdTe QDs can emit 530 nm of fluorescence. These two wavelengths just correspond to the absorbance maxima of the two most important intermediates in bR photocycle, the protonated ground state B_{570} and the deprotonated bleached form M_{412} (279), respectively.

As has been reported, if M_{412} is illuminated by blue light during its lifetime, it is photoconverted back to bR (280), and its proton rebinding is enhanced by the blue light (281). The current study was the first to use QDs as subsidiary near-field light sources to accelerate the bR photocycle in a hybrid bR/QD bionanosystem. The resulting stationary photocurrent of the hybrid system under external blue illumination verified the capacity of QDs to serve as embedded light sources.

6.2 Preparation and Measurement

6.2.1 CdTe QDs

To obtain the green-fluorescence emitter, the CdTe QDs in this study were synthesized by using the one-pot aqueous method (278). First, 4 ml of 0.04 mol•l^{-1} CdCl$_2$ was diluted to 50 ml in a beaker, then 100 mg of trisodium citrate• 2H$_2$O, 4 ml of 0.01 mol•l^{-1} Na$_2$TeO$_3$, 70 mg of MSA, and 50 mg of NaBH$_4$ were added and continuously stirred until the color of the solution turned green. The solution was then transferred into the autoclave and heated at 180 ℃ for the length of time necessary to obtain the CdTe QDs of the desired size.

The CdTe QDs were formed according to the following reactions:

$$4\ TeO_3^{2-}+3BH_4^{-}\rightarrow 4Te^{2-}+3BO_2^{-}+6H_2O \qquad (1)$$

$$CdL+Te^{2-}\rightarrow CdTe+L,\ where\ L=MSA \qquad (2)$$
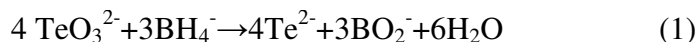
During reaction (1), NaBH$_4$ reduces TeO$_3^{2-}$ to Te,$^{2-}$ then in reaction (2), the fresh Te^{2-} reacts with Cd^{2+} to yield CdTe. Citrate must be added to avoid the deposition of cadmium tellurite (CdTeO$_3$).

6.2.2 Preparation of bR/QD Hybrid-Based Electrode

The concentration of the as-prepared CdTe QD solution was concentrated to 0.25 mol/l. The prepared bR-PM fragments were then suspended in Milli-Q H$_2$O to form a 5 mg/ml suspension of pH 7.4 before use. The bR suspension

and QD solution were then mixed together at a 9:1 ratio and resuspended to achieve a homogeneous mixture. EPS was conducted according to Wang et al.'s protocol (148) with a minor modification to immobilize the bR/QD mixture onto a gold electrode, forming the desired bionanosystem.

6.3 Characterization of the Hybrid Membrane

6.3.1 UV-Vis Spectra and Fluorescence Intensity Curves of bR/QDs Mixture

Figure 6-1a shows the fluorescence of the bR/QD mixture, the BSA/QD mixture, and the Milli-Q H_2O/QD mixture, respectively, under excitation of 410 nm illumination. As can be observed by comparing the bR/QD mixture to both the BSA/QD and Milli-Q H_2O/QD mixture, the latter two of which serve as controls, the addition of bR into the QD solution decreases the fluorescence intensity dramatically - to less than 5% of that of the original intensity. This difference in the fluorescence intensity between the bR/QD mixture and the other two mixtures is evidently due to the role of bR. It is well known that the maximum absorbance of bR at its ground state is 570 nm (Fig. 6-1b), a fact that can explain the reduction of fluorescence intensity of QDs after their combination with bR. Clearly, a large proportion of the fluorescence emitted by QDs (537 nm) must have been absorbed by bR.
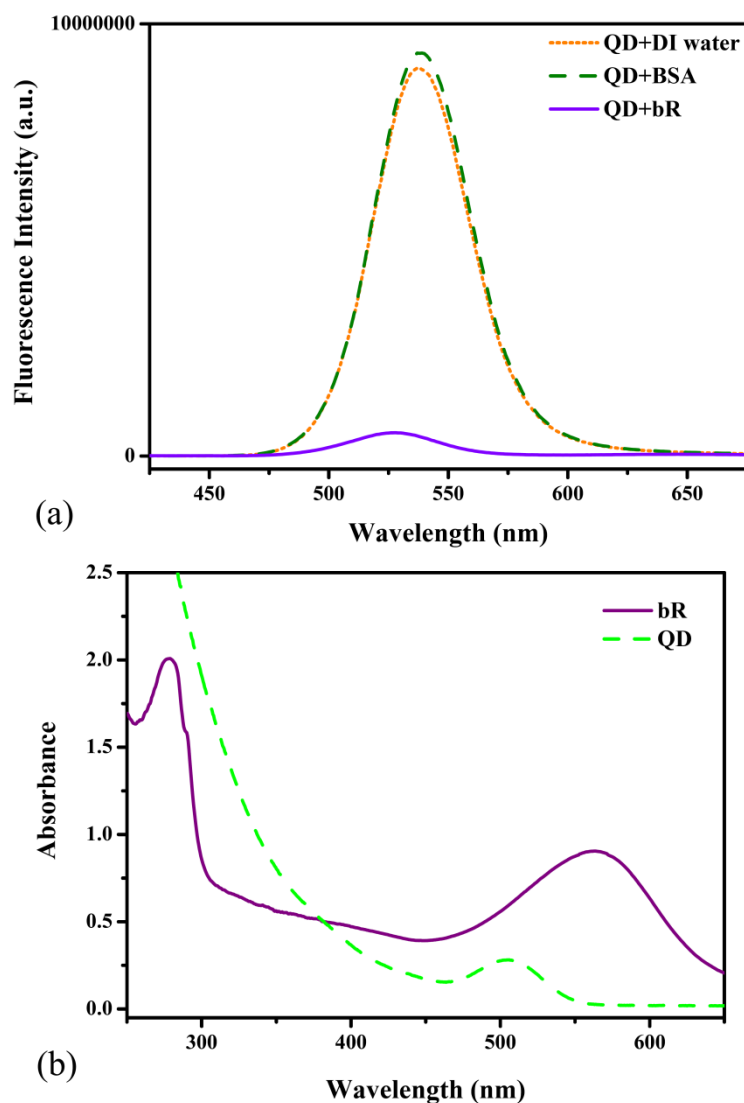
Figure 6-1 (a) Fluorescence intensity curves of bR/QDs mixture, BSA/QDs mixture and Milli-Q H2O/QDs mixture (mixed at a ratio of 9:1, respectively) and (b) UV-Vis spectra of bR suspension and QDs solution.

6.3.2 Fluorescence Intensity of the bR/QD Thin Films

Figure 6-2b, which shows the fluorescence of the bR and bR/QD thin films under excitation of 460 nm light source, demonstrates that pure bR emits very weak fluorescence, while the bR/QD bionanosystem can give off strong fluorescence. Both the optical images (Fig. 6-2a) and the fluorescent images

104

(Fig. 6-2c) also show the remarkable differences between the two thin films.

Both the morphology and fluorescence intensity data reveal that EPS deposition

is efficient for immobilization of the negatively charged bR/QDs, of which the

QDs are negatively charged due to the -COO⁻ group from MSA and bR has a

high density of negative surface charge (169), with the fluorescence well
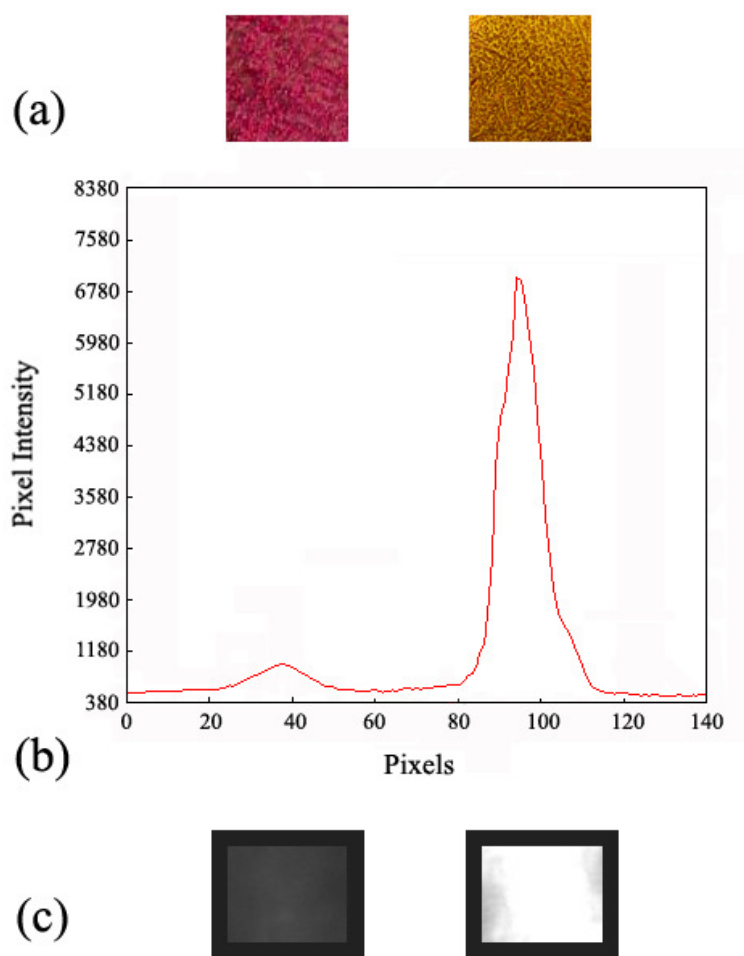
Figure 6-2 (a) Optical image of bR-immobilized gold surface (left) and bR/QD bionanosystem-immobilized gold surface (right). (b) Fluorescence intensity curve for bR-immobilized gold surface (left peak) and bR/QD-composite-immobilized gold surface (right peak). (c) Fluorescence images for bR-immobilized gold surface (left rectangle) and bR/QD-bionanosystem immobilized gold surface (right rectangle), which correspond to the peaks in (b).

reserved. This result also proves that QDs can be added into the bR photoelectric response system as incorporated nanoscaled light sources that can completely physically intermingle with bR without introducing any impurities.

6.4 Photoelectric Response of the Hybrid Membrane

Figure 6-3 shows the photoelectric responses of the bR/QD bionanosystem. With QDs serving as the subsidiary light sources, the bR/QD bionanosystem generates a stationary photocurrent pulse when excited with 410 nm of illumination (Fig. 6-3a). The shape of the photocurrent pulse is completely different from those generated by both a bR/QD bionanosystem under 570 nm of illumination (Fig. 6-3b) and pure bR under 410 nm of illumination (Fig. 6-3c), although the magnitude of the three are all approximately 45 nA/cm^2. It is noteworthy that the phenomena discovered in this work are specific to the bR/QD bionanosystem under excitation of 410 nm of illumination because the photocurrent shape of pure bR excited with 410 nm of illumination also two spikes in opposite directions.

Generally, application of only 570 nm of illumination can initiate the deprotonation of the Schiff-base linkage, which is located at the bR binding site of the retinal component, thus transforming bR from B_{570} to M_{412}. The formation of the M_{412} intermediate that leads to an increase in proton concentration at the electrode/electrolyte interface due to bR proton release

106
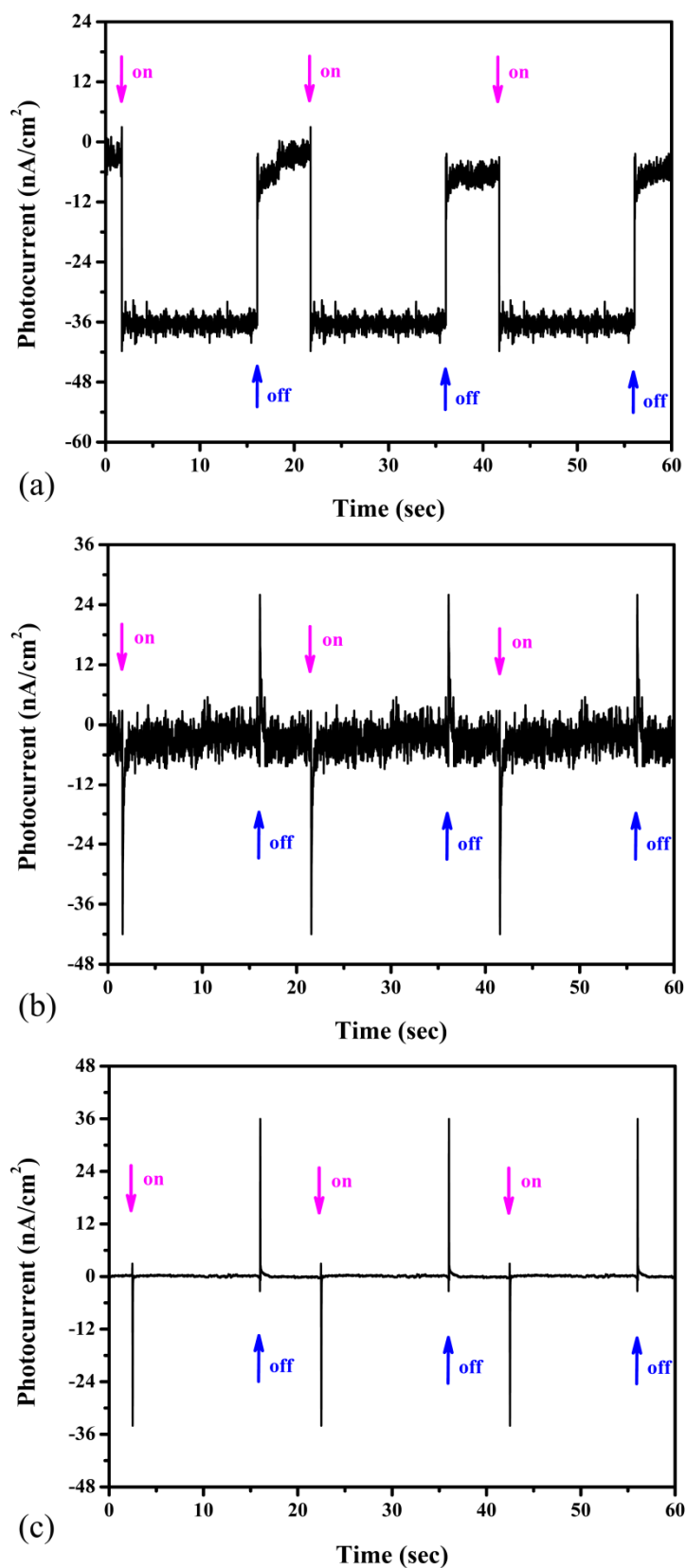
Figure 6-3 Time profiles of the photocurrent of the (a) bR/QD bionanosystem under 410 nm of illumination, (b) bR/QD bionanosystem under 570 nm illumination, and (c) pure bR under 410 nm illumination.

produces the light-on photocurrent; in contrast, the decay of the M_{412}intermediate back to B_{570}, the rate-limiting step in the photocycle (282) that results in a decrease in proton concentration at the interface due to bR proton uptake, contributes to the light-off photocurrent (169). As this process takes place, the photocycle is completed, with both the light-on and -off photocurrents behaving as transient spikes.

Blue light illumination, on the other hand, can reconvert the M state to the initial B_{570} state within only several hundred nanoseconds (283-286). It can also translocate protons but in the opposite direction; that is, from the EC to the CP side (287). As reported by Nagy (279), Uehara *et al.* (288), and He *et al.* (289), if a wild type bR sample is initially irradiated with green light and then also exposed to blue light illumination, the blue light could cause an opposite effect to that of the green light illumination. As a result, the photocurrent excited by green light would be partly counteracted by that excited by the blue light.

6.5 Mechanism for the Stationary Photocurrent Generation

This study proposes a model for the bR/QDs bionanosystem in which the bR and QDs retain their respective specific functions to provide a platform that incorporates both a current generator and a light source, as shown in Figure 6-4. Since B_{570} and M_{412} have much longer lifetimes than other intermediates in the bR photocycle (290-291), only B_{570} and M_{412} and their corresponding excited

states are considered in the model. In this experiment, although only 410 nm illumination is externally applied, the CdTe QDs incorporated into the bionanosystem act like many nanoscaled light sources uniformly distributed and embedded among the bR molecules to generate fluorescence at 537 nm. Thus, blue light and green light irradiate the bR component in the system while simultaneously affects B_{570} and M_{412}, respectively. As shown in Figure 6-4a, at its initial exposure to 410 nm of illumination, the bR in the system becomes light-adapted, i.e., the bR returned to its ground state (B_{570}). Then, the fluorescence at 537 nm emitted by the QDs immediately irradiates the adjacent bR molecules, which causes a steep drop from their baseline (proton releasing). Besides exciting QDs, the 410 nm illumination also directly affects the bR by accelerating the decay of its recently formed M_{412} intermediate (proton uptaking). As Nagy pointed out (279), when blue light is applied in addition to green light, the transmitted proton does not truly reach the extracellular surface of the PM, allowing the bR molecule to regain it, thereby shunting the proton pump.

In this experiment, two wavelengths of illumination are superimposed on each other during the entire process when the light source is on. Hence, although proton release and uptake repeatedly occurred inside the PM, the proton never truly reaches the EC space, thus generating a stationary photocurrent. Only when the external blue light is turned off and the green fluorescence of the QDs thus extinguishes, the proton could be pumped to the

EC side, which, accompanied by the decay of the M_{412} intermediate, results in a

decrease in proton concentration at the interface due to bR proton uptake and

produces the light-off photocurrent (169).
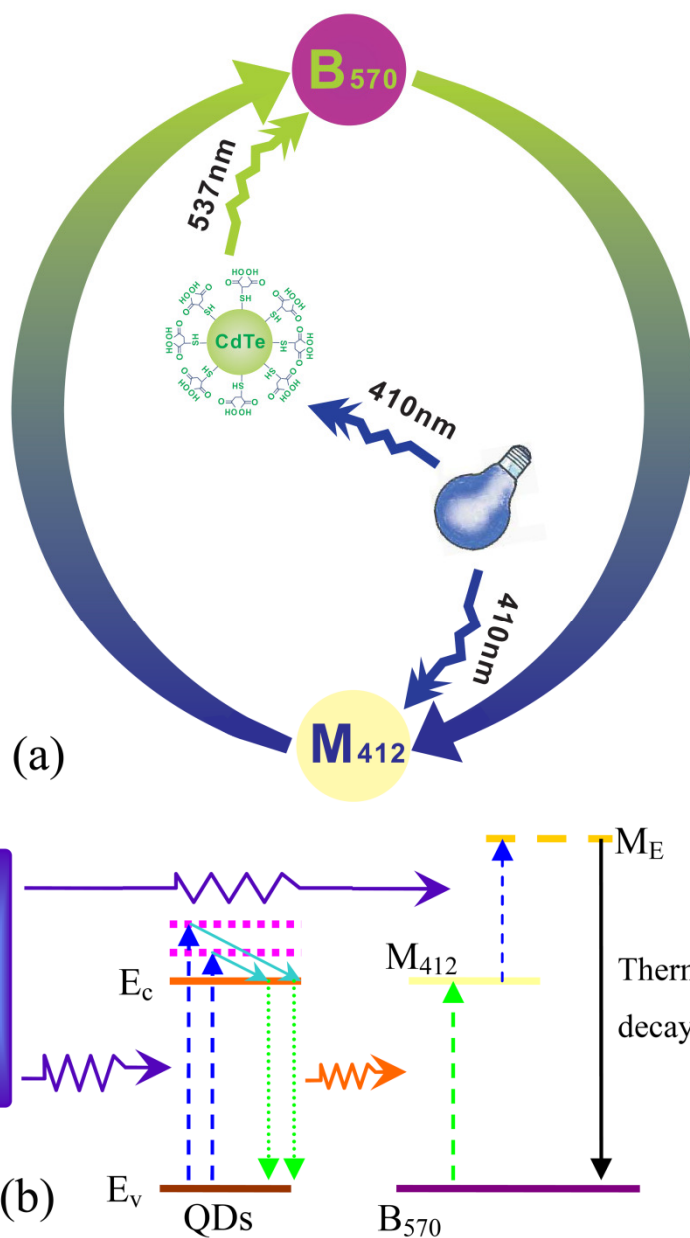
Figure 6-4 Model of the stationary current generation of bR/QDs bionanosystem as (a) photochemical cycle and (b) equivalent level diagram of the photochemical cycle.

From the view of energy change (Fig. 6-4b), upon blue light illumination,

QDs are pumped to the excited state and then emit green light. As a result of the absorption of green light, bR molecules are excited from the B_{570} state to the M_{412} state. At the same time, the blue light pumps M_{412} to its excited state ME, which photochemically decays to the initial B_{570} state in a shorter time (approximately in nanosecond scale) compared to the normal thermal relaxation of several milliseconds. Therefore, the photocycle could operate more rapidly than the situation with illumination of only 570 nm, and thus generates the stationary photocurrent.

6.6 Conclusion

In this work, a novel hybrid bR/QD bionanosystem is constructed. In the hybrid QDs play a role as subsidiary incorporated nanoscaled light sources. With the assistance of QD fluorescence, single wavelength blue light illumination can induce the hybrid bionanosystem to produce a stationary photocurrent. This bR/QD bionanosystem has great potential in the fabrication of new types of optical devices and bio solar cells.

Chapter 7 Bidirectional Mediation of TiO$_2$ Nanowires Field Effect Transistor by Dipole Moment from PM [d]

7.1 Introduction

One-dimensional (1D) inorganic nanostructures (nanotubes, nanowires and nanorods), possessing unique physical and chemical properties derived from their various size, shapes and constitutions are of great importance in both theoretical research (292-293) and practical applications (294-295). Currently, the study of metal oxide semiconductors with 1D nanostructures intrigues many research groups, primarily due to their potential applications in electronic and optoelectronic devices such as solar cells (296), nanosensors (297), and nanolasers (298).

Among numerous materials in this category, TiO$_2$ nanostructures have been extensively studied in electrochemical sensors (260), photovoltaic cells (299), and lithium batteries (300). Besides their inherent physicochemical properties, TiO$_2$ nanostructures have low toxicity and high biocompatibility (261), which make them superior candidates for applications, especially for uses associated

_____

[d] Reproduced by permission of The Royal Society of Chemistry.
http://pubs.rsc.org/en/Content/ArticleLanding/2010/NR/B9NR00375D

with biomaterials (301). To date, only few demonstrations of TiO_2 nanowires based field effect transistors (FETs) including single-nanowire FET (302) and Co-doped TiO_2 nanowire FET (303) have been reported. However, it remains a great challenge to improve the charge transport properties, particularly by an external mediation in the electrical transport of the TiO_2 nanowires FET.

One notable characteristic of bR-PM closely related to its proton pumping function is the permanent dipole moment (191), pointing unidirectionally from its cytoplasmic (CP) side to the extracellular side (EC). Considerable efforts have been made in theoretical studies of this bio-origin dipole (191, 304-305). Bradley *et al*. conducted a pioneering study to locate the dipole in the PM by studying its interaction with a carbon nanotube (CNT)s-based nanodevice (306). Although properties of the bR dipole remain unclear, the dipole moment of 3.3×10^{-28} C•m per bR monomer (307) is believed to result from a charge asymmetry on the two sides of the bR-PM (308). Such a dipole moment appears too small to have any noticeable impact on bulk materials, but it is highly possible to play a critical role in nanoscale interactions, and thus may have a significant effect on nanomaterials.

In this work, a unique TiO_2 nanowires FET was fabricated by aligning and connecting the TiO_2 nanowires with source and drain electrodes under dielectrophoretic (DEP) force, and then was further modified with bR-PM before the effect of bR-PM on the FET performance was investigated.

7.2 Device Preparation and Measurement

7.2.1 TiO$_2$ Nanowires Preparation

Hydrothermal synthesis method (309), rendering high pressure and high temperature environment, is used to fabricate TiO$_2$ nanowires (310). In brief, 200 mg commercial TiO$_2$ granules were mixed with 40 ml 10 mol•L^{-1} NaOH solution and then placed into a Teflon-lined autoclave. Under autogenous pressure, the autoclave was maintained at 180 ℃ for 24 h and then allowed to cool naturally until it reached room temperature. All the liquid in the product was decanted before the sample was washed with 1 mol•L^{-1} of HCl aqueous solution repeatedly, allowing ion exchange from Na$^+$ to H$^+$ to form H$_2$Ti$_3$O$_7$, and then washed with Milli Q water and absolute ethanol, sequentially, for several times. The sample was dried at 70 ℃ for 6 h to obtain a soft, fibrous, white TiO$_2$ powder. TiO$_2$ nanowire suspensions at different concentrations were prepared in absolute ethanol by 5 minutes of ultrasonication for the optimization of concentration in the electric field assisting alignment process.

7.2.2 Patterning

Heavily n-doped silicon (Si) wafers with a 100-nm thick top oxide layer (SiO2) were patterned using photoresist (311). After patterning, the wafers were introduced to an electron beam evaporator, and thin metal films (1 nm of Ti and 50 nm of Au) were deposited on them under a 1×10^{-6} Torr vacuum. After the

deposition, the patterned photoresist was lifted off the wafers by immersion in acetone assisted by gentle sonication to finalize the electrode patterning.

7.2.3 Device Fabrication

The silicon wafer and its surface SiO_2 layer (100 nm), which had a unit area capacitance of 34 nF/cm^2 (312), was employed as the gate electrode and gate dielectric, respectively. For all devices, the channel length and width were 2 μm and 1800 μm, respectively. The electrode-patterned wafers were briefly cleaned by sonication in acetone before use. The LCR meter was used to conduct the alignment of TiO_2 nanowires across the electrode pair, employing DEP forces in an alternating electric field to make the nanowires align in a direction parallel to that of the electric field. The alignment parameters were optimized before further experimentation in order to contact both ends of most nanowires across the electrode pair.

After characterization and measurement of the TiO_2 nanowires FETs, the EPS method was employed with a minor modification (263) on the protocol of Wang *et al*. (148) to immobilize the bR-PM (2 mg/mL, neutral pH) onto the FETs for mediation of their performance.

7.2.4 Electric Characterization

The output as well as transfer characteristics of devices with and without bR-PM were characterized using a semiconductor-parameter analyzer system

with a probe station under conditions of controlled relative humidity (RH) and nitrogen atmosphere unless stated otherwise.
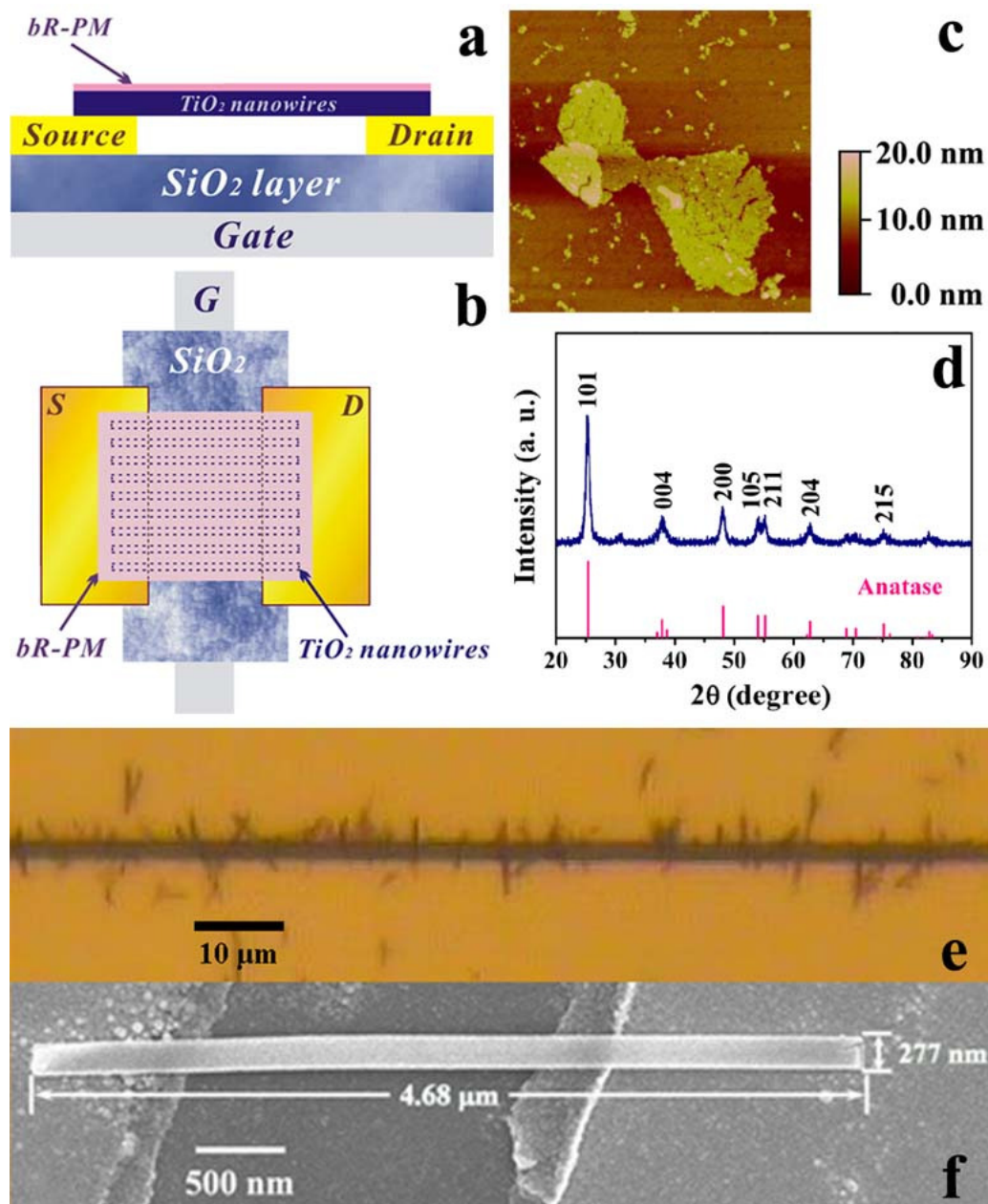
Figure 7-1 Structure of the TiO_2 nanowires FET device. (a) Side view and (b) top view of the schematic structure; (c) AFM image of bR-PM (image size of 3.0 µm × 3.0 µm); (d) XRD spectrum of TiO_2 nanowires, lower part shows the standard diffraction peaks of anatase TiO_2 (JCPDS No. 89-4921); (e) TiO_2 nanowires alignment across the channel of electrodes under microscope (top view) and (f) SEM image of single TiO_2 nanowire aligned across the channel.

7.3 Device Structure

The schematic structure of the bottom-contact device with gold as the source and drain electrodes is illustrated in Figure 7-1a. The approach utilized to fabricate the TiO_2 nanowires FET device is actually an alignment process using DEP force in an alternating electric field, as that used to align various nanostructures such as DNA molecules (313), gold nanowires (314), CNTs (315-316), metal/semiconducting nanoparticles, and nanorods (317-318). In this study, for nanowires deposition across a pair of electrodes, the DEP assisted alignment is chosen because the external applied electric field induces polarization and thus generates a temporary dipole moment along the nanowires for an energetically favorable orientation, i.e., an orientation parallel to the direction of the electric field (318). In addition to facilitating the parallel alignment of multiple nanowires across the two electrodes, the method allows electrical contact of the nanowires with the two electrodes to construct the nanowires FET device.

To ensure both ends of the nanowires are in good contact with the paired Au electrodes, the nanowire concentration and parameters of the electric field for the alignment such as frequency and voltage were optimized (Fig. 7-2), resulting in the optimal experimental conditions of 0.5 mM of TiO_2 nanowires, 15 kHz and 2 V, respectively, as shown in Figure 7-2h. With these optimized conditions used, analysis of all microscopic images revealed that each fabricated FET device was composed of approximately 200 single TiO_2

nanowires. The image in Figure 7-1e shows that multiple TiO_2 nanowires were parallelly aligned and vertically across the two electrodes. In Figure 7-1f, a representative SEM image for a single TiO_2 nanowire in the device clearly illustrates its good alignment across the two electrodes, with an average length and width of 4.68 μm and 277 nm, respectively. The chemical composition of the as-prepared nanowires was confirmed by X-ray diffraction (XRD) analysis as shown in Figure 1d. All the identified peaks of the XRD patterns can be unambiguously assigned to anatase TiO_2 (JCPDS card No. 89-4921). The bR-PM was characterized by UV-Vis spectroscopy in the previous work (263).

The surface morphology of the bR-PM (Fig. 7-1c) depicts the patch structure of the monolayer bR-PM, indicating that the orientation of bR-PM should be uniform to induce unidirectional dipoles in order to maximize the possible effect of bio-origin dipoles on the FET. Thus the EPS method was used to deposit bR-PM on the top of the TiO_2 nanowires FET to render the optimal orientation of every bR molecule, i.e., with its CP side facing to nanowires and its EC side facing outside. In such a way, the permanent dipole in each bR molecule could be vertically oriented to the PM surface, and thus the electric field (E_{bR}) generated points vertically from the surface of the bR- PM to the TiO_2 nanowires FET.
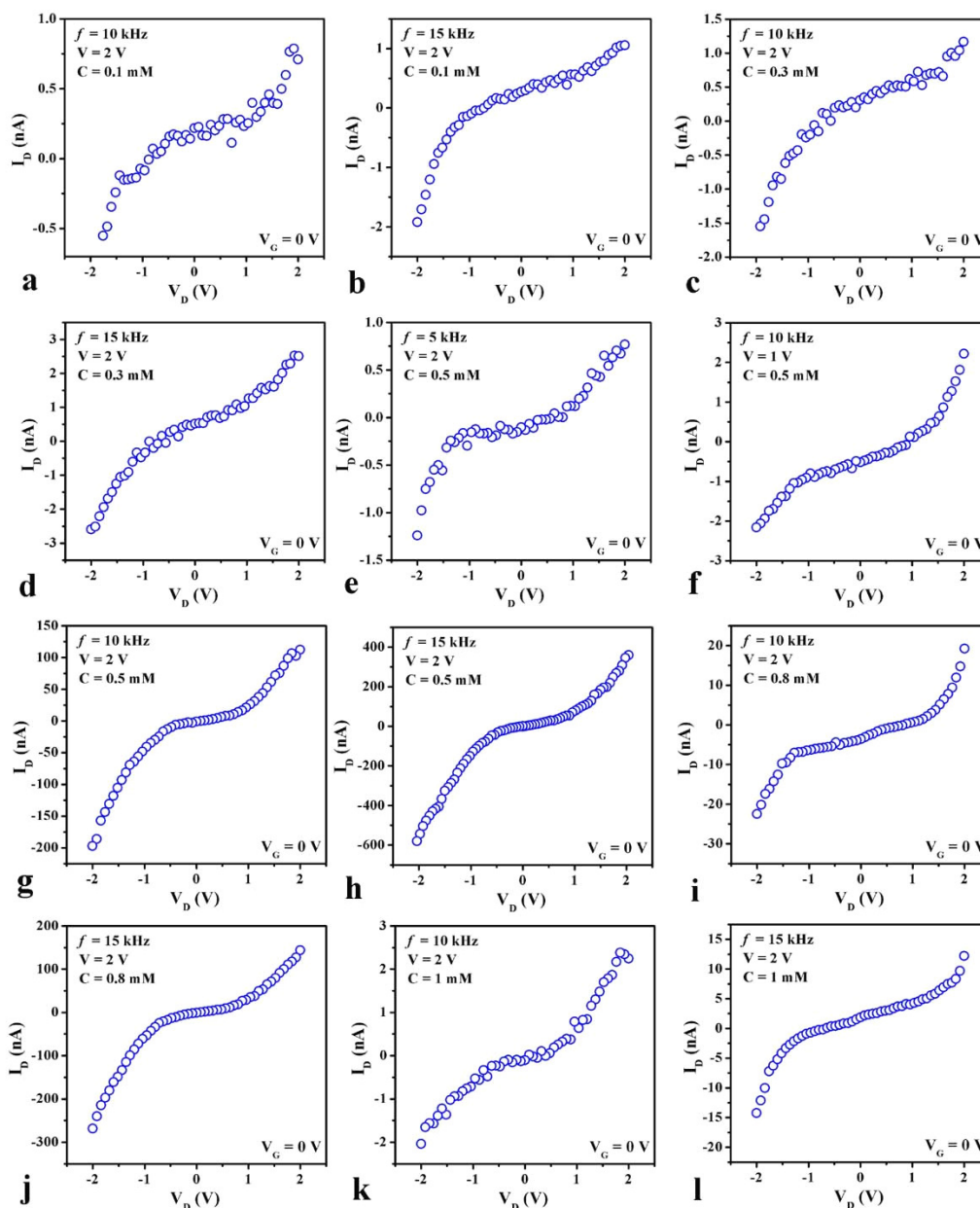
Figure 7-2 Optimization of the alignment parameters. Sets of frequency, voltage, and TiO_2 concentration are shown in each figure.

7.4 Effect of bR-PM on the Electric Transport of the TiO_2 Nanowires FET

The effect of bR-PM modification on the output (I_D-V_D) characteristics and

the transfer (I_D-V_G) characteristics of the TiO_2 nanowires FET are shown in

Figure 7-3 and Figure 7-4, respectively. Clearly, the modification of bR-PM on TiO$_2$ nanowires raises the drain current in n-channel operation (V_G, $V_D < 0$, Figure 7-3a) whereas reduces the drain current in p-channel operation (V_G, $V_D > 0$, Figure 7-3b). The corresponding I_D-V_D changes after bR-PM modification are presented in Figure 7-3c and d, respectively. The transfer characteristics demonstrate the same trend in Figure 7-4a and 7-4b. The on/off ratio rises from approximately 9 to 12 for the TiO$_2$ nanowires FET after bR-PM modification
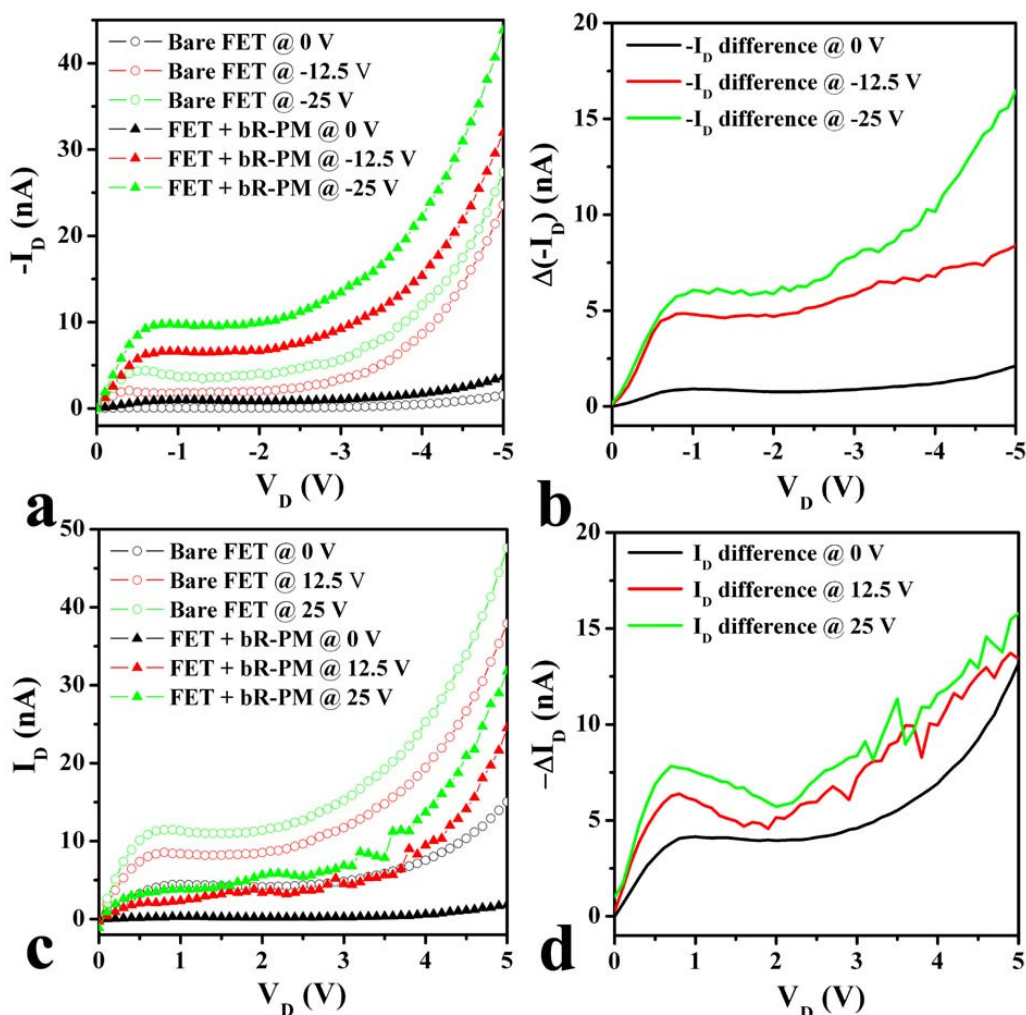
Figure 7-3 Effect of bR-PM on the output (I_D-V_D) characteristics of the TiO$_2$ nanowires FET in the negative gate voltage region (a) without and with PM deposition and (b) the difference caused, and within the positive gate voltage region (c) without and with PM deposition and (d) the difference caused.
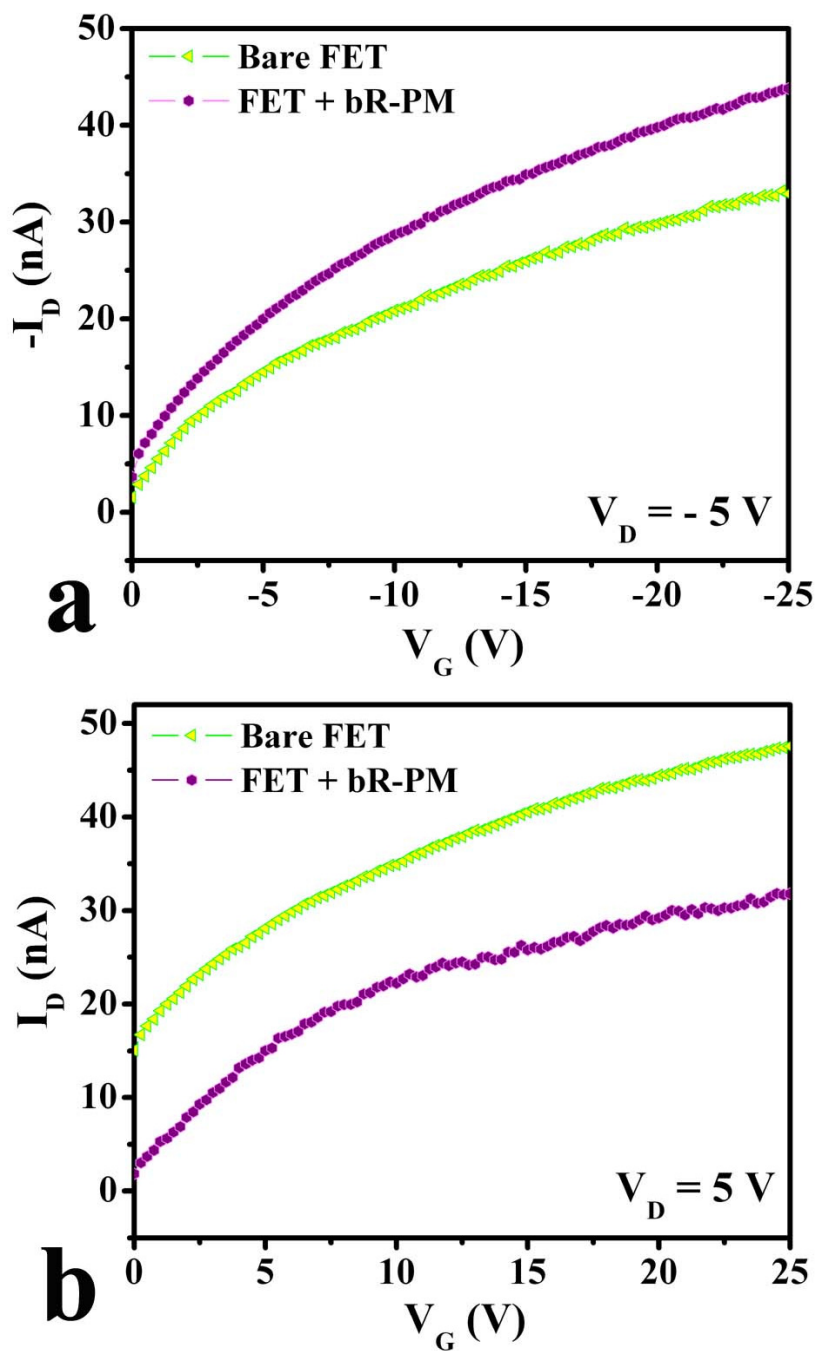
Figure 7-4 Effect of bR-PM on the transfer (I_D-V_G) characteristics of the TiO_2 nanowires FET within the (a) negative gate voltage region and (b) positive gate voltage region.

by changing the gate voltage from 0 to -25 V. Both the output and the transfer

characteristics clearly indicate that bR-PM modification has a bidirectional

mediation effect on the TiO_2 nanowires FET under different directions of the

gate electric field and that, especially when the gate voltage is negative, bR-PM modification can enhance the transfer and output characteristics of the FET.

Device mobility (μ) in the linear regime under negative gate bias was extracted following the equation (neglecting contact resistance) used by Cai. *et al*. (311)

$$(V_{DS} << V_{GS} - V_T): I_{DS} = V_{DS} C_i \mu (V_{GS} - V_T) W/L$$

where I_{DS}, C_i, V_{GS}, and V_T are the drain current, the capacitance per unit area of the gate dielectric layer, the gate voltage, and the threshold voltage, respectively.
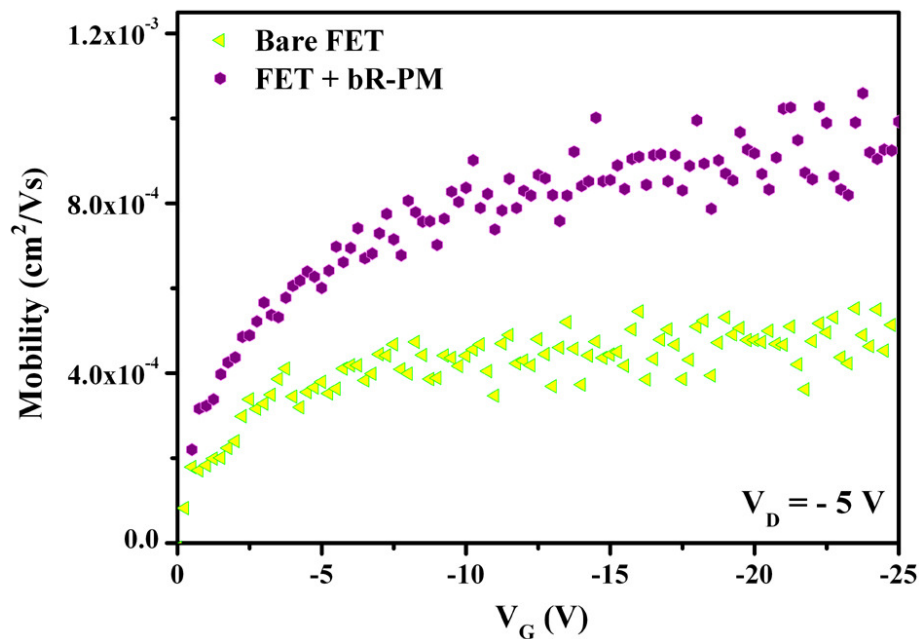
Figure 7-5 Mobility of the TiO_2 nanowires FET before and after bR-PM modification.

From our experimental results in Figure 7-5, with imposed negative bias, the mobility of the bare TiO_2 nanowires FET is 5.14×10^{-4} $cm^2 \cdot V^{-1} \cdot s^{-1}$

(corresponding to a carrier concentration of 5.67×10^9 C•cm^{-3}), while after bR-PM modification it increases by a factor of 2 to 9.93×10^{-4} cm^2•V^{-1}•s^{-1} (corresponding to a carrier concentration of 9.08×10^9 C•cm^{-3}), indicating that bR-PM modification can greatly enhance the hole mobility in TiO_2 nanowires FETs, a finding consistent with the transfer and output characterization results shown above.

7.5 Mediation Mechanism

Because TiO_2 is very sensitive to humidity (319-320), any modification of bR-PM from an aqueous suspension could introduce moisture on the TiO_2 FET structure that yields a high leakage current for an increased drain current. To exclude this possibility as the reason for the production of the current, the effect of RH on the bR-PM-modified FET was investigated. The I_D-V_D curves of the FETs measured at a series of levels of RH (Fig. 7-6) exhibits an increased drain current, with an increase in RH for FETs both with and without the bR-PM modification. However, although the increase caused by RH for both FETs with and without the bR-modification is of almost the same magnitude, it is insignificant in comparison to the enhanced drain current by modification of the bR. In addition, since the I_D-V_D measurement of the FETs are conducted under low RH (< 30%), the effect of RH on the drain current of the bR-modified FET could be ignored.
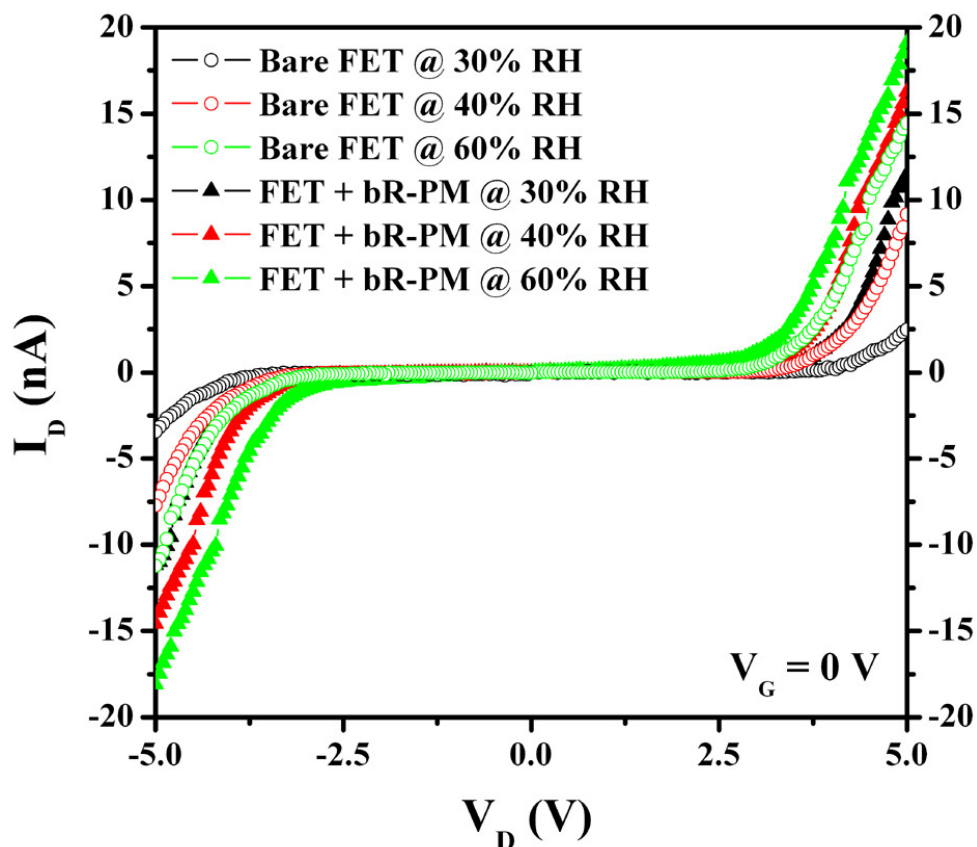
Figure 7-6 Effects of the RH change on TiO_2 nanowires FET without and with bR-PM modification.

The electric field induced by the permanent dipole of bR-PM is very likely to contribute to the enhanced performance of the bR-modified TiO_2 nanowires FET under negative gate voltage. The EPS method employed in the bR-PM modification ensured an orientation of the membrane favorable to generating unidirectional E_{bR} on the FET surface by the inherent dipoles of bR molecules. Regarding this assumption, the intensity of the E_{bR} could be theoretically estimated. Other researchers have found the value of the dipole to be approximately 3.3×10^{-28} C•m per bR monomer (307), and it is known that bR-PM patches have a constant thickness of 5 nm (37).

The following formulas were used for dipole moment calculation and electric field calculation, respectively:

$$p = q * d \qquad (1)$$

$$E = k * \frac{q}{r^2} \qquad (2)$$

where p, q, d, and r are the dipole moment, the charge amount, the displacement vector pointing from the negative charge to the positive charge, and the distance from the particle with charge q to the electric field evaluation point, respectively. Because the bR-PM directly contacted the TiO_2 nanowires in this study, the electric field at the bottom surface of the bR could be used to represent the electric field exerted on the surface of the TiO_2. If it is assumed that the electric field in the bR layer produced by the inherent dipoles is uniform, r can be replaced with d. Since k is a constant equal to 8.987×10^9 N•m^2•C^{-2}, E_{bR} can be calculated to be approximately 2.37×10^7 N• C^{-1} (equal to 2.37×10^7 V• m^{-1}) for a monolayer of bR-PM.

The electric field generated by the gate voltage, here termed E_G, was calculated by using the formula:

$$E_G = V_G / d \qquad (3)$$

where d is the thickness of the SiO_2 layer (100 nm). For $E_G = 0 \sim 16.67 \times 10^7$ N• C^{-1} when $V_G = 0 \sim -25$ V, which is comparable to E_{bR}, indicating that the assumption that that the E_{bR} can affect FET performance is reasonable.

The relationship between the number of modified bR-PM layers and FET performance was investigated to determine if a relationship existed between increased FET performance under negative gate voltage and the characteristics of the dipole's effect. For the modification by oriented multilayer bR-PM on the TiO_2 nanowires FET, as the number of layers increases, the neutralization of opposite charge located on adjacent surfaces of the membranes will take place, making the overall value of E_{bR} generated by the deposited multilayer bR-PM decreased, and thus a diminishing trend in the augment of the I_D being resulted in. By varying the concentration of the bR-PM suspension, bR-PM with different layer numbers could be deposited on the TiO_2 nanowires FET to adjust the electric field generated from the bR dipoles. Figure 7-7 shows the relationship between the normalized ΔI_D (normalized $\Delta I_D = (I_{D \text{ (with bR-PM)}} - I_{D \text{ (without bR-PM)}}) / I_{D \text{ (without bR-PM)}})$ vs. the gate voltage after modification by depositing different numbers of layers of bR-PM. A reduction in ΔI_D vs. the gate voltage can be observed as the number of layers of bR-PM deposited onto the TiO_2 nanowires FET increases.

My previous study (259) indicated that, one patch layer of bR-PM corresponds to an approximate optical density in express of $OD_{560} = 0.0256$. Thus, the layer number of bR-PM deposited on the FET device can be directly monitored by the OD_{560} of the modified multilayer membrane, and the relationship between the concentration of the bR-PM suspension and the optical density of the deposited multilayer membrane established. With a bR-PM
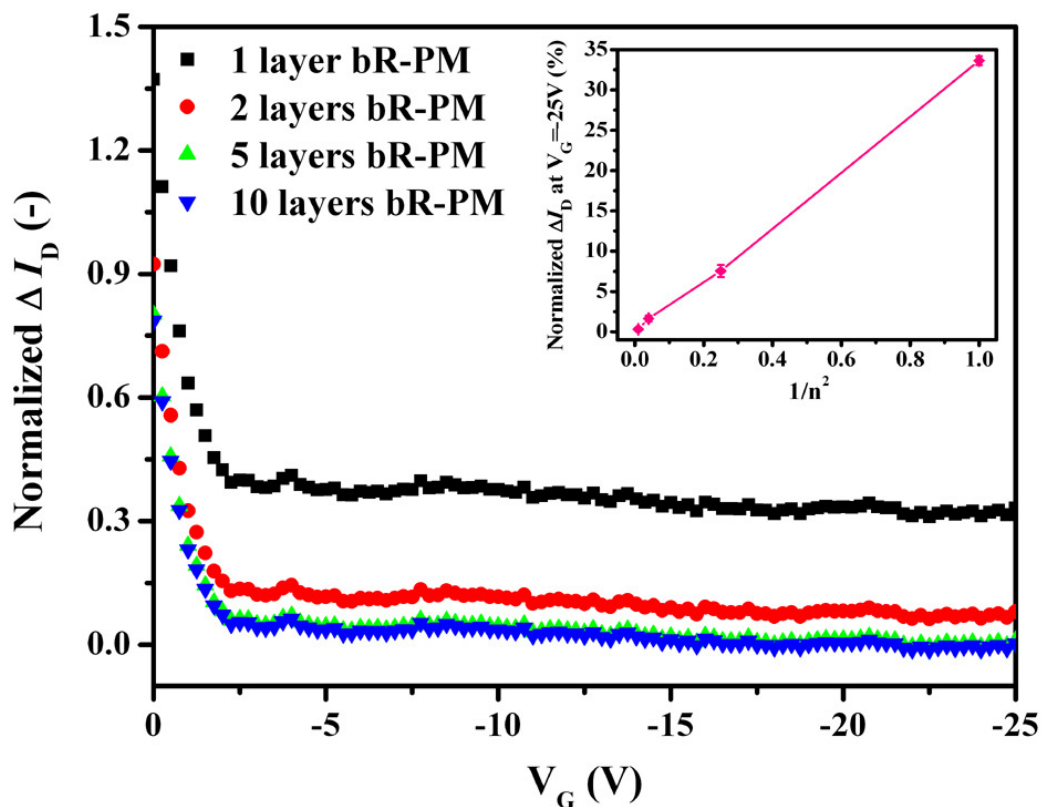
Figure 7-7 Effects of the deposited bR-PM of different layer number on the normalized ΔI_D of the TiO$_2$ nanowires FET at V_D = -5V. Inset depicts the relationship between the percentage of the ΔI_D at the maximum gate voltage and the reciprocal of the square of the number of bR-PM layers modified.

suspension of 2 mg/ml and a deposited amount of 1 μl, OD$_{560}$=0.256 of the resulting bR-PM membrane could be obtained, indicating that approximate 10 layers of PM patches could be deposited on the FET surface. Therefore, the number of bR-PM layers could be adjusted by applying a series of dilution factors in the 2 mg/ml bR-PM suspension. The relationship between the change of normalized ΔI_D in express of percentage at the maximum gate voltage (in this case -25 V) vs. the reciprocal of the square of the modified number of bR-PM layers is shown in the inset of Figure 7-7. Theoretically, the effects of modification at a dilution factor of 1, 2, 5, and 10 in the 2-mg/ml bR-PM

suspension should correspond to 10, 5, 2, and 1 layer bR-PM membrane deposited on the of the FET, respectively. If the electric field generated by dipole moment from monolayer bR-PM is regarded as E_{bR}, the electric field generated by dipole moment from 2, 5, and 10 layers of bR-PM are 1/4 E_{bR}, 1/25 $E_{bR,}$ and 1/100 E_{bR}, respectively. The quantitative trend shown in the inset of Figure 7-7 accords well with the theoretically calculated E_{bR} change, indicating that the drain current change is roughly in inverse proportion to the layer number of deposited bR-PM, which again confirms the assumption that the TiO$_2$ nanowires FET can be influenced by dipole moment from the modified bR-PM.

The unidirectional permanent dipole existing within bR molecules is proposed here to account for the observed mediation in performance of the TiO$_2$ nanowires FET, as schematically shown in Figure 7-8. When negative bias is applied (Fig. 7-8a), E_{bR} produced by the permanent dipole of the bR is in the same direction of E_G does, the electric field produced by the gate voltage. Thus, bR-PM modification can enhance the entire electric field applied on the TiO$_2$ nanowires FET to generate a significantly larger drain current. However, when a positive gate voltage is applied (Fig. 7-8b), the E_{bR} is in the opposite direction to that of E_G, weakening the entire electric field applied to the TiO$_2$ nanowires FET and thus decreasing the drain current. These approach may have universal significance to enhance the performance of FETs based on other nanowires.
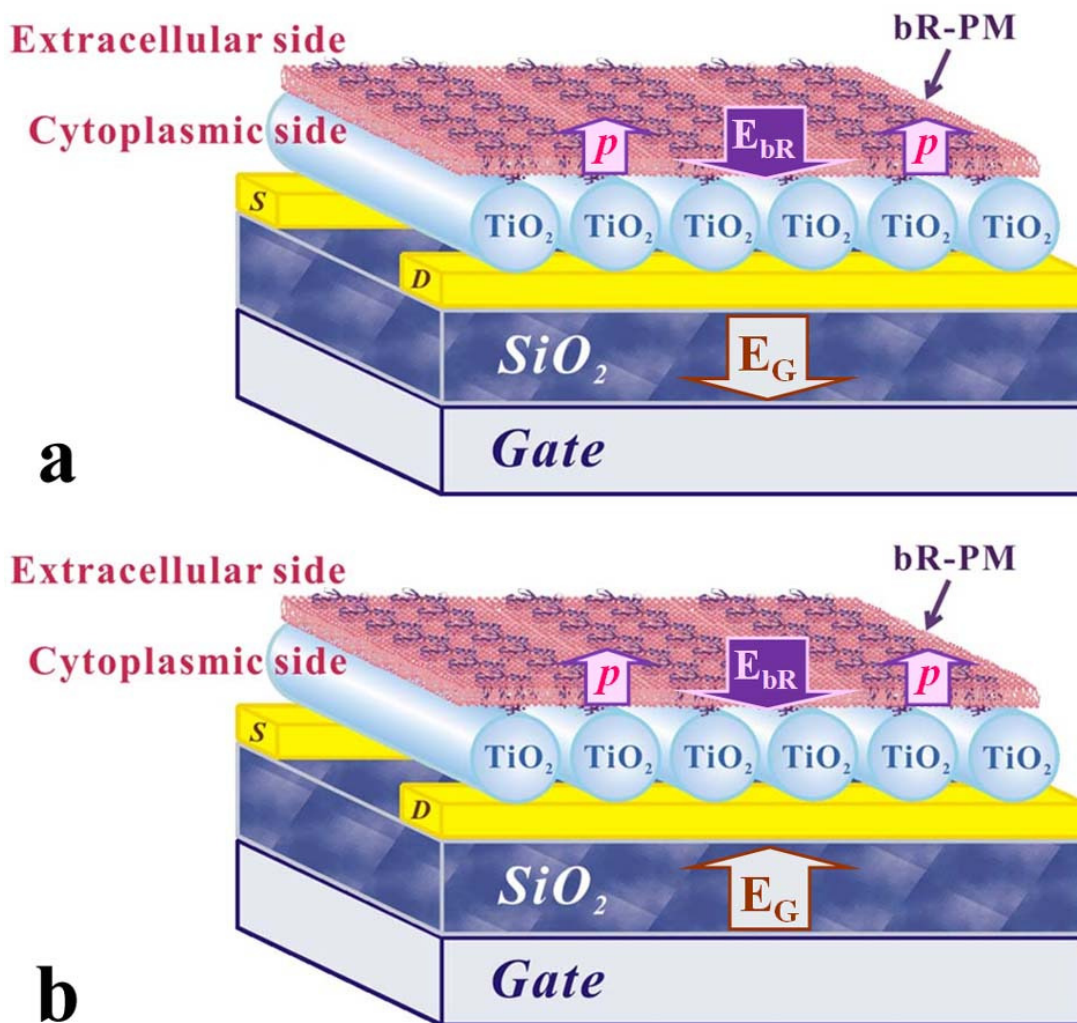
Figure 7-8 Schematic drawing of the relationship between the E_{bR} and E_G when (a) negative gate voltage and (b) positive gate voltage is applied on the TiO$_2$ nanowires FET.

7.6 Conclusions

In this study, bR-PM modified bottom-contact TiO$_2$ nanowires FETs are fabricated and the dipole bio-originated from bR-PM is employed to tune the FET performance. It is found that with negative gate voltage, both the transfer and output characteristics of the TiO$_2$ nanowires FETs improved, with the hole mobility improved by a factor of 2 after bR-PM modification. By varying the

concentration of the bR-PM suspension used in the modification, the number of layers deposited onto the FET surface is adjusted and it is found that normalized ΔI_D decreases as the number of bR-PM layers modified on the FET increases, providing evidence that the electric field generated by the dipole moment from the bR-PM enhances the hole transport in the TiO_2 nanowires FET. This bidirectional mediation of bR-PM on FET performance provides a novel platform for bR-PM bioelectronics application.

Chapter 8 General Conclusion and Outlook

8.1 General Conclusion

This dissertation thoroughly reviews the research of bR, especially on the photoelectric properties related to converting light energy to electric energy *in vitro*. After introducing the fundamental structure and biological functions of bR, it summarizes potential bioelectronic applications proposed for bR over past 30 years. The development and limitations of reported bR-based photoelectric devices are discussed, and the motivations/objectives are brought forth accordingly.

As one of my accomplishments, a new strategy using PLL as the assembler to construct well-oriented PLL/bR-PM multilayer film by LbL technique through electrostatic adsorption has been successfully established. Through investigations on the respective effect of concentrations, pH and adsorption time on the photoelectric response, various LbL assembly parameters were optimized and chosen to fabricate the optimal multilayer structure. Different characterizations were employed to monitor the multilayer construction process. The UV-Vis absorption spectrum demonstrates the natural conformation of bR-PM is properly preserved in the assembled multilayer structure and confirms that the assembly process of each PLL/bR-PM bilayer is highly reproducible with a linear relationship of the adsorption amount of bR-PM versus the bilayer number. The *in-situ* SPR monitoring reveals that the

adsorption of bR-PM in the multilayer film growth is well in agreement with the Langmuir adsorption kinetics and verifies the coverage of bR-PM monolayer in the PLL assembled multilayer film could reach as high as 90%. The adsorbed amount of bR-PM in the film is also calculated from the SPR results. AFM characterization proves that the patch structure of bR-PM remains in the PLL/bR-PM multilayer and the roughness linearly increases with the increased bilayer number. As the assembler plays critical role in determining the amount of bR assembled in the LbL multilayer film and thus the photoelectric performance, the photoelectric performance of PLL/bR-PM multilayer was compared with those generated by bR film assembled with other polycations as reported in literature. The result demonstrates that PLL is an excellent assembler for the LbL assembly of bR-PM to significantly enhance the photoelectric responses.

A unique integrated bR/$WO_3 \cdot H_2O$/PVA membrane retaining the bR biological function as a proton pump and the specific spill-over effect of $WO_3 \cdot H_2O$ nanocrystals was fabricated. In the integrated film, $WO_3 \cdot H_2O$ nanocrystals were pre-incorporated with PVA matrix to form a membrane followed by being laminated on top of the oriented bR film. It has been verified that such integrated film boosts photoelectric response of bR by around six fold. The enhancement mechanism is possibly due to the hydrogen spillover process of the $WO_3 \cdot H_2O$. This work could render a promising proton exchange membrane in bio fuel cell applications.

A novel hybrid bR/QDs bionanocomposite was fabricated to synergy the unique properties from both components. The excitation and emission wavelengths of the QDs, 410 and 532 nm, just correspond to the absorbance maxima of the two most important intermediates in the photocycle of bR, the protonated ground state B_{570} and the deprotonated bleached form M_{412}, making it possible for QDs to play the role as subsidiary near-field light sources in nanoscale. With the involvement of QDs, externally applied single-wavelength blue light illumination (410 nm) can cause green fluorescence in the hybrid system so that simultaneous effects of blue and green illumination are exerted on bR photocycle to make it accelerated, thus inducing an unusual stationary photocurrent in the hybrid bionanosystem. The bR/QD bionanosystem would have promising applications in fabricating new type of optical devices and bio solar cell.

The inherent dipole moment in bR-PM was also applied to modify the bottom-contact TiO$_2$ nanowires FET and produce a bidirectional mediation effect on the FET performance. In the bR-modified nanowire transistor, it is found that with negative gate voltage, both transfer and output characteristics of the TiO$_2$ nanowires FETs are improved with the hole mobility increased apparently by a factor of 2. By varying the concentration of the bR-PM suspension used in the modification, the layer number deposited onto the FET surface was adjusted. Results reveals that the normalized ΔI_D decreases with layer number of bR-PM increases, proving that the electric field generated by

the dipole moment from the bR-PM actually enhances the hole transport in the TiO$_2$ nanowires FET. The bidirectional mediation of bR-PM on the performance of the FET provides a novel platform for the bioelectronic application of bR-PM.

The accomplishment of this project not only provides new approaches to improve bioelectronic performance of bR for viable applications but also expands in-depth fundamental knowledge in bioelectronics.

8.2 Outlook

For the improvement in LbL immobilization of bR, screening more high-efficient assemblers with great biocompatibility that can help to immobilize more bR into the LbL multilayer film and thus generating higher photoelectric response could be a good direction of research. Moreover, it is worth investigating how to overcome the increased resistance as layer number grows in the multilayer film so that the photoelectric response can be further improved.

In the view of nanomaterials selection for construction of bR-based assemblies, more attempts with newly developed nanostructured materials can be made. When it comes to the bR/QD hybrid bionanocomposite, it is of high importance to further improve the amplitude of the stationary photocurrent by

the construction of various bionanocomposites that might make a bR-based bio solar cell come into being.

For the bidirectional mediation on electrical performance of TiO_2 nanowires FET by bR, further study could be carried out to optimize the assembly, particularly, to significantly reduce the leakage current by the improvement in the modification structure and device fabrication techniques. In addition, a bR-enhanced single nanowire FET device will be very attractive in future work.

Regarding that bR is naturally light-sensitive and possesses very similar structure to rhodopsin, the mammalian retina protein, by using advance assembly techniques and nanocomposing of bR with superior functional materials, enhancement of the photoelectric response of bR-based assemblies could ultimately lead to the success in construction of artificial eyes based on bR. This is definitely exciting and very challenging research project in the future.

Abbreviations

bR: bacteriorhodopsin

PM: purple membrane

bR-PM: bacteriorhodopsin-embedded purple membrane

Rh: rhodopsin

H. salinarum: *Halobacterium salinarum*

CP: cytoplasmic

EC: extracellular

PLL: poly-L-lysine

PVA: poly vinyl alcohol

IPA: 2-propanol

11-MUA: 11-mercaptoundecanoic acid

PBS: phosphate buffered saline

TEMED: N, N, N', N' -tetramethylethylene

SDS: sodium dodecyl sulfate

PAGE: polyacrylamide gel electrophoresis

APS: amonium persulfate

QD: quantum dot

UV-Vis: ultraviolet-visible spectroscopy

AFM: atomic force microscope

EDX: energy dispersive X-ray spectroscopy

SAED: selective area electron diffraction

BSA: bovine serum albumin

DEP: dielectrophoretic

RH: relative humidity

FET: field effect transistor

LbL: layer-by-layer

PDAC: poly(dimethyldiallylammonium chloride) (169-170, 227)(169-170, 227)(169-170, 227)(169-170, 227)

PAH: poly(allylamine hydrochloride)

PEI: poly(ethylenimine)

EPS: electrophoretic sedimentation

LB: Langmuir-Blodgett

SPR: surface plasmon resonance

ITO: indium tin oxide

CNT: carbon nanotube

FESEM: field emmission scanning electronic microscopy

FTIR: Fourier transform infrared

HRTEM: high-resolution transmission electron microscopy

XRD: X-ray powder diffraction

TGA: thermogravimetric analysis

References

1. Willner, I., and E. Katz. **2005**. Bioelectronics - An Introduction. In: Bioelectronics: From Theory to Applications. I. Willner, and E. Katz, editor editors (eds). Wiley-VCH, Weinheim, Germany. 1-14.

2. Katz, E., and I. Willner. **2003**. Probing biomolecular interactions at conductive and semiconductive surfaces by impedance spectroscopy: Routes to impedimetric immunosensors, DNA-Sensors, and enzyme biosensors. *Electroanalysis* 15:913-947.

3. Heller, A. **1990**. Electrical wiring of redox enzymes. *Accounts of Chemical Research* 23:128-134.

4. Willner, I., and E. Katz. **2000**. Integration of layered redox proteins and conductive supports for bioelectronic applications. *Angewandte Chemie-International Edition* 39:1180-1218.

5. Göpel, W., and P. Heiduschka. **1995**. Interface analysis in biosensor design. *Biosensors & Bioelectronics* 10:853-883.

6. Zhong, C. J., and M. D. Porter. **1995**. Designing interfaces at the molecular-level. *Analytical Chemistry* 67:A709-A715.

7. Campbell, C. N., D. Gal, N. Cristler, C. Banditrat, and A. Heller. **2002**. Enzyme-amplified amperometric sandwich test for RNA and DNA. *Analytical Chemistry* 74:158-162.

8. Yang, M. S., M. E. McGovern, and M. Thompson. **1997**. Genosensor technology and the detection of interfacial nucleic acid chemistry. *Analytica Chimica Acta* 346:259-275.

9. Bardea, A., E. Katz, A. F. Buckmann, and I. Willner. **1997**. NAD(+)-dependent enzyme electrodes: Electrical contact of cofactor-dependent enzymes and electrodes. *Journal of the American Chemical Society* 119:9114-9119.

10. Anzai, J., H. Takeshita, Y. Kobayashi, T. Osa, and T. Hoshi. **1998**. Layer-by-layer construction of enzyme multilayers on an electrode for the preparation of glucose and lactate sensors: Elimination of ascorbate interference by means of an ascorbate oxidase multilayer. *Analytical Chemistry* 70:811-817.

11. Bartlett, P. N., and K. F. E. Pratt. **1995**. Theoretical treatment of diffusion and kinetics in amperometric immobilized enzyme electrodes.1. Redox mediator entrapped within the film. *Journal of Electroanalytical Chemistry* 397:61-78.

12. Galceran, J., S. L. Taylor, and P. N. Bartlett. **2001**. Modelling the steady-state current at the inlaid disc microelectrode for homogeneous mediated enzyme catalysed reactions. *Journal of Electroanalytical Chemistry* 506:65-81.

13. Ghindilis, A. L., and I. N. Kurochkin. **1994**. Glucose potentiometric electrodes based on mediatorless bioelectrocatalysis - a new approach. *Biosensors & Bioelectronics* 9:353-357.

14. Ianniello, R. M., T. J. Lindsay, and A. M. Yacynych. **1982**. Immobilized xanthine-oxidase chemically modified electrode as a dual analytical sensor. *Analytical Chemistry* 54:1980-1984.

15. Kazanskaya, N., A. Kukhtin, M. Manenkova, N. Reshetilov, L. Yarysheva, O. Arzhakova, A. Volynskii, and N. Bakeyev. **1996**. FET-based sensors with robust photosensitive polymer membranes for detection of ammonium ions and urea. *Biosensors & Bioelectronics* 11:253-261.

16. Zayats, M., A. B. Kharitonov, E. Katz, A. F. Buckmann, and I. Willner. **2000**. An integrated NAD(+)-dependent enzyme-functionalized field-effect transistor (ENFET) system: development of a lactate biosensor. *Biosensors & Bioelectronics* 15:671-680.

17. Bardea, A., A. Dagan, I. Ben-Dov, B. Amit, and I. Willner. **1998**. Amplified microgravimetric quartz crystal-microbalance analyses of oligonucleotide complexes: a route to a Tay-Sachs biosensor device. *Chemical Communications*:839-840.

18. BenDov, I., I. Willner, and E. Zisman. **1997**. Piezoelectric immunosensors for urine specimens of Chlamydia trachomatis employing quartz crystal microbalance microgravimetric analyses. *Analytical Chemistry* 69:3506-3512.

19. LionDagan, M., I. BenDov, and I. Willner. **1997**. Microgravimetric quartz-crystal microbalance analysis of cytochrome c interactions with pyridine and pyridine-nitrospiropyran monolayer electrodes: Characterization of inter-protein complexes at the functionalized surfaces. *Colloids and Surfaces B-Biointerfaces* 8:251-260.

20. O'Sullivan, C. K., R. Vaughan, and G. G. Guilbault. **1999**. Piezoelectric immunosensors - Theory and applications. *Analytical Letters* 32:2353-2377.

21. Amador, S. M., J. M. Pachence, R. Fischetti, J. P. McCauley, A. B. Smith, and J. K. Blasie. **1993**. Use of self-assembled monolayers to covalently tether protein monolayers to the surface of solid substrates. *Langmuir* 9:812-817.

22. Hobara, D., K. Niki, C. Zhou, G. Chumanov, and T. M. Cotton. **1994**. Characterization of cytochurome c immobilized on modified gold and silver electrodes by surface-enhanced Raman spectroscopy. *Colloids and Surfaces A: Physicochemical and Engineering Aspects* 93:241-250.

23. Jordan, C. E., and R. M. Corn. **1997**. Surface plasmon resonance imaging measurements of electrostatic biopolymer adsorption onto chemically modified gold surfaces. *Analytical Chemistry* 69:1449-1456.

24. Liedberg, B., C. Nylander, and I. Lundström. **1995**. Biosensing with surface-plasmon resonance - how it all started. *Biosensors & Bioelectronics* 10:R1-R9.

25. Raitman, O. A., E. Katz, A. F. Buckmann, and I. Willner. **2002**. Integration of polyaniline/poly(acrylic acid) films and redox enzymes on electrode supports: An in situ electrochemical/surface plasmon resonance study of the bioelectrocatalyzed oxidation of glucose or lactate in the integrated bioelectrocatalytic systems. *Journal of the American Chemical Society* 124:6487-6496.

26. Raitman, O. A., F. Patolsky, E. Katz, and I. Willner. **2002**. Electrical contacting of glucose dehydrogenase by the reconstitution of a pyrroloquinoline quinone-functionalized polyaniline film associated with an Au-electrode: an in situ electrochemical SPR study. *Chemical Communications*:1936-1937.

27. Feher, G., J. P. Allen, M. Y. Okamura, and D. C. Rees. **1989**. Structure and function of bacterial photosynthetic reaction centers. *Nature* 339:111-116.

28. Kartha, S., R. Das, and J. R. Norris. **1991**. Electron transfer in photosynthetic reaction centers. In: Metal Ions in Biological Systems. vol. 27. H. Sigel, and A. Sigel, editor editors (eds). Marcel Dekker, New York. 323-359.

29. Stryer, L. **1986**. Cyclic-GMP cascade of vision. *Annual Review of Neuroscience* 9:87-119.

30. Siebert, F. **2003**. Retinal Proteins. In: Photochromism: Molecules and Systems. H. D. a. H. BouasLaurent, editor (ed) (eds). Eisevier, Amsterdam. 756-792.

31. Haupt, W. **1983**. Photoperception and photomovement. *Philosophical Transactions of the Royal Society of London Series B-Biological Sciences* 303:467-478.

32. Senger, H., and W. Schmidt. **1994**. Diversity of photoreceptors. In: Photomorphogenesis in Plants. R. E. Kendrick, and G. H. M. Kronenberg, editor editors (eds). Kluwer Academic Publishers, Dordrecht. 301-325.

33. Smith, H. **1975**. Phytochrome and photomorphogenesis: an introduction to the photocontrol of plant development. McGraw-Hill, London.1766

34. Birge, R. R. **1990**. Nature of the primary photochemical events in rhodopsin and bacteriorhodopsin. *Biochimica et Biophysica Acta* 1016:293-327.

35. Marinetti, T. **1987**. Large-scale nonproton ion release and bacteriorhodopsins state of aggregation in lipid vesicles.1. Monomers. *Biophysical Journal* 52:115-121.

36. Willner, I., and S. Rubin. **1996**. Control of the structure and functions of biomaterials by light. *Angewandte Chemie-International Edition in English* 35:367-385.

37. Hampp, N. **2000**. Bacteriorhodopsin as a photochromic retinal protein for optical memories. *Chemical Reviews* 100:1755-1776.

38. Oesterhelt, D., and W. Stoeckenius. **1971**. Rhodopsin-like protein from the purple membrane of Halobacterium halobium. *Nature: New biology* 233:149-152.

39. Li, F., Y. Feng, P. J. Dong, and B. Tang. **2010**. Gold nanoparticles modified electrode via a mercapto-diazoaminobenzene monolayer and its development in DNA electrochemical biosensor. *Biosensors & Bioelectronics* 25:2084-2088.

40. Wise, K. J., N. B. Gillespie, J. A. Stuart, M. P. Krebs, and R. R. Birge. **2002**. Optimization of bacteriorhodopsin for bioelectronic devices. *Trends in Biotechnology* 20:387-394.

41. Henderson, R., and G. F. X. Schertler. **1990**. The structure of bacteriorhodopsin and its relevance to the visual opsins and other 7-helix g-protein coupled receptors. *Philosophical Transactions of the Royal Society of London Series B-Biological Sciences* 326:379-389.

42. Findlay, J. B. C. **1986**. The structure of rhodopsin. *Photobiochemistry and Photobiophysics* 13:213-228.

43. Hirai, T., S. Subramaniam, and J. K. Lanyi. **2009**. Structural snapshots of conformational changes in a seven-helix membrane protein: lessons from bacteriorhodopsin. *Current Opinion in Structural Biology* 19:433-439.

44. Oesterhelt, D., and W. Stoeckenius. **1973**. Functions of a new photoreceptor membrane. *Proceedings of the National Academy of Sciences of the United States of America* 70:2853-2857.

45. Koutalos, Y., and T. G. Ebrey. **1986**. Recent progress in vertebrate photoreception. *Photochemistry and Photobiology* 44:809-817.

46. Blaurock, A. E., and W. Stoeckenius. **1971**. Structure of the purple membrane. *Nature: New biology* 233:152-155.

47. Michel, H., D. Oesterhelt, and R. Henderson. **1980**. Orthorhombic two-dimensional crystal form of purple membrane. *Proceedings of the National Academy of Sciences of the United States of America* 77:338-342.

48. Haupts, U., J. Tittor, and D. Oesterhelt. **1999**. Closing in on bacteriorhodopsin: Progress in understanding the molecule. *Annual Review of Biophysics and Biomolecular Structure* 28:367-399.

49. Henderson, R., and P. N. T. Unwin. **1975**. Three-dimensional model of purple membrane obtained by electron microscopy. *Nature* 257:28–32.

50. Unwin, P. N. T., and R. Henderson. **1975**. Molecular structure determination by electron microscopy of unstained crystalline specimens. *Journal of Molecular Biology* 94:425-440.

51. Lanyi, J. K. **2004**. X-ray diffraction of bacteriorhodopsin photocycle intermediates (Review). *Molecular Membrane Biology* 21:143-150.

52. Leifer, D., and R. Henderson. **1983**. Three-dimensional structure of orthorhombic purple membrane at 6.5 Å resolution. *Journal of Molecular Biology* 163:451–466.

53. Michel, H., and D. Oesterhelt. **1980**. Three-dimensional crystals of membrane proteins: Bacteriorhodopsin. *Proceedings of the National Academy of Sciences of the United States of America* 77:1283–1285.

54. Glaeser, R. M., J. S. Jubb, and R. Henderson. **1985**. Structural comparison of native and deoxycholate-treated purple membrane. *Biophysical Journal* 48:775-780.

55. Tsygannik, I. N., and J. M. Baldwin. **1987**. Three-dimensional structure of deoxycholate-treated purple membrane at 6 Å resolution and molecular averaging of three crystal forms of bacteriorhodopsin. *European biophysics journal* 14:263–272.

56. Khorana, H. G., G. E. Gerber, W. C. Herlihy, C. P. Gray, R. J. Anderegg, K. Nihei, and K. Biemann. **1979**. Amino acid sequence of bacteriorhodopsin. *Proceedings of the National Academy of Sciences of the United States of America* 76:5046-5050.

57. Ovchinnikov, Y. A., N. G. Abdulaev, M. Y. Feigina, A. V. Kiselev, and N. A. Lobanov. **1979**. The structural basis of the functioning of bacteriorhodopsin: An overview. *FEBS Letters* 100 219–224.

58. Grigorieff, N., T. A. Ceska, K. H. Downing, J. M. Baldwin, and R. Henderson. **1996**. Electron-crystallographic refinement of the structure of bacteriorhodopsin. *Journal of Molecular Biology* 259:393-421.

59. Henderson, R., J. M. Baldwin, T. A. Ceska, F. Zemlin, E. Beckmann, and K. H. Downing. **1990**. Model for the structure of bacteriorhodopsin based on high-resolution electron cryomicroscopy. *Journal of Molecular Biology* 213:899-929.

60. Henderson, R., and D. Shotton. **1980**. Crystallization of purple membrane in three dimensions. *Journal of Molecular Biology* 139:99-109.

61. Michel, H. **1982**. Characterization and crystal packing of 3-dimensional bacteriorhodopsin crystals. *EMBO Journal* 1:1267-1271.

62. Schertler, G. F. X., H. D. Bartunik, H. Michel, and D. Oesterhelt. **1993**. Orthorhombic crystal form of bacteriorhodopsin nucleated on benzamidine diffracting to 3.6 Å resolution. *Journal of Molecular Biology* 234:156-164.

63. Henderson, R., J. M. Baldwin, K. H. Downing, J. Lepault, and F. Zemlin. **1986**. Structure of purple membrane from halobacterium halobium: recording, measurement and evaluation of electron micrographs at 3.5 Å resolution. *Ultramicroscopy* 19:147-178.

64. Pebay-Peyroula, E., G. Rummel, J. P. Rosenbusch, and E. M. Landau. **1997**. X-ray structure of bacteriorhodopsin at 2.5 angstroms from microcrystals grown in lipidic cubic phases. *Science* 277:1676-1681.

65. Landau, E. M., and J. P. Rosenbusch. **1996**. Lipidic cubic phases: A novel concept for the crystallization of membrane proteins. *Proceedings of the National Academy of Sciences of the United States of America* 93:14532-14535.

66. Rummel, G., A. Hardmeyer, C. Widmer, M. L. Chiu, P. Nollert, K. P. Locher, I. Pedruzzi, E. M. Landau, and J. P. Rosenbusch. **1998**. Lipidic cubic phases: New matrices for the three-dimensional crystallization of membrane proteins. *Journal of Structural Biology* 121:82-91.

67. Belrhali, H., P. Nollert, A. Royant, C. Menzel, J. P. Rosenbusch, E. M. Landau, and E. Pebay-Peyroula. **1999**. Protein, lipid and water organization in bacteriorhodopsin crystals: a molecular view of the purple membrana at 1.9 angstrom resolution. *Structure* 7:909-917.

68. Luecke, H., B. Schobert, H. T. Richter, J. P. Cartailler, and J. K. Lanyi. **1999**. Structure of bacteriorhodopsin at 1.55 angstrom resolution. *Journal of Molecular Biology* 291:899-911.

69. Schobert, B., J. Cupp-Vickery, V. Hornak, S. O. Smith, and J. K. Lanyi. **2002**. Crystallographic structure of the K intermediate of bacteriorhodopsin: Conservation of free energy after photoisomerization of the retinal. *Journal of Molecular Biology* 321:715-726.

70. Findlay, J. B. C., and D. J. C. Pappin. **1986**. Opsin family of proteins. *Biochemical Journal* 238:625-642.

71. Ebrey, T. G. **1993**. Light energy transduction in bacteriorhodopsin. In: Thermodynamics of Membrane Receptors and Channels. M. B. Jackson, editor (ed) (eds). CRC Press, Boca Raton, FL. 353–387.

72. Lanyi, J. K. **1993**. Proton Translocation Mechanism and Energetics in the Light-Driven Pump Bacteriorhodopsin. *Biochimica et Biophysica Acta* 1183:241-261.

73. Mathies, R. A., S. W. Lin, J. B. Ames, and W. T. Pollard. **1991**. From femtoseconds to biology - mechanism of bacteriorhodopsins light-driven proton pump. *Annual Review of Biophysics and Biophysical Chemistry* 20:491-518.

74. Oesterhelt, D., J. Tittor, and E. Bamberg. **1992**. A unifying concept for ion translocation by retinal proteins *Journal of Bioenergetics and Biomembranes* 24:181-191.

75. Rothschild, K. J. **1992**. FTIR difference spectroscopy of bacteriorhodopsin - toward a molecular-model. *Journal of Bioenergetics and Biomembranes* 24:147-167.

76. Lozier, R. H., R. A. Bogomolni, and W. Stoeckenius. **1975**. Bacteriorhodopsin: a light-driven proton pump in Halobacterium Halobium. *Biophysical Journal* 15:955-962.

77. Petrich, J. W., J. Breton, J. L. Martin, and A. Antonetti. **1987**. Femtosecond absorption-spectroscopy of light-adapted and dark-adapted bacteriorhodopsin. *Chemical Physics Letters* 137:369-375.

78. Polland, H. J., M. A. Franz, W. Zinth, W. Kaiser, E. Kolling, and D. Oesterhelt. **1986**. Early picosecond events in the photocycle of bacteriorhodopsin. *Biophysical Journal* 49:651-662.

79. Sharkov, A. V., A. V. Pakulev, S. V. Chekalin, and Y. A. Matveetz. **1985**. Primary events in bacteriorhodopsin probed by subpicosecond spectroscopy. *Biochimica et Biophysica Acta* 808:94-102.

80. Jardetzky, O. **1966**. Simple allosteric model for membrane pumps. *Nature* 211:969–970.

81. Lanyi, J. K., and G. Varo. **1995**. The photocycles of bacteriorhodopsin. *Israel Journal of Chemistry* 35:365-385.

82. Oesterhelt, D. **1998**. The structure and mechanism of the family of retinal proteins from halophilic archaea. *Current Opinion in Structural Biology* 8:489-500.

83. Luecke, H., and J. K. Lanyi. **2003**. Structural clues to the mechanism of ion pumping in bacteriorhodopsin. In: Membrane Proteins. D. C. Rees, editor (ed) (eds). Elsevier Science B. V., Amsterdam. 111-130.

84. Balashov, S. P., E. S. Imasheva, T. G. Ebrey, N. Chen, D. R. Menick, and R. K. Crouch. **1997**. Glutamate-194 to cysteine mutation inhibits fast light-induced proton release in bacteriorhodopsin. *Biochemistry* 36:8671-8676.

85. Brown, L. S., J. Sasaki, H. Kandori, A. Maeda, R. Needleman, and J. K. Lanyi. **1995**. Glutamic-acid-204 is the terminal proton release group at the extracellular surface of bacteriorhodopsin. *Journal of Biological Chemistry* 270:27122-27126.

86. Albeck, A., N. Friedman, M. Sheves, and M. Ottolenghi. **1986**. Role of retinal isomerizations and rotations in the photocycle of bacteriorhodopsin. *Journal of the American Chemical Society* 108:4614-4618.

87. Fang, J. M., J. D. Carriker, V. Baloghnair, and K. Nakanishi. **1983**. Evidence for the necessity of double-bond (13-ene) isomerization in the proton pumping of bacteriorhodopsin. *Journal of the American Chemical Society* 105:5162-5164.

88. Honig, B., T. Ebrey, R. H. Callender, U. Dinur, and M. Ottolenghi. **1979**. Photoisomerization, energy storage, and charge separation: A model for light energy transduction in visual pigments and bacteriorhodopsin. *Proceedings of the National Academy of Sciences of the United States of America* 76:2503-2507.

89. Kuschmitz, D., and B. Hess. **1982**. Trans-cis isomerization of the retinal chromophore of bacteriorhodopsin during the photocycle. *FEBS Letters* 138:137-140.

90. Mathies, R. A., C. H. B. Cruz, W. T. Pollard, and C. V. Shank. **1988**. Direct observation of the femtosecond excited-state cis-trans isomerization in bacteriorhodopsin. *Science* 240:777-779.

91. Tsuda, M., M. Glaccum, B. Nelson, and T. G. Ebrey. **1980**. Light isomerizes the chromophore of bacteriorhodopsin. *Nature* 287:351-353.

92. Birge, R. R., L. A. Findsen, and B. M. Pierce. **1987**. Molecular-dynamics of the primary photochemical event in bacteriorhodopsin - theoretical evidence for an excited singlet-state assignment for the J-intermediate. *Journal of the American Chemical Society* 109:5041-5043.

93. Bogomolni, R. A., R. A. Baker, R. H. Lozier, and W. Stoeckenius. **1980**. Action spectrum and quantum efficiency for proton pumping in halobacterium-halobium. *Biochemistry* 19:2152-2159.

94. Li, Q. Q., R. Govindjee, and T. G. Ebrey. **1984**. A correlation between proton pumping and the bacteriorhodopsin photocycle. *Proceedings of the National Academy of Sciences of the United States of America-Biological Sciences* 81:7079-7082.

95. Longstaff, C., and R. R. Rando. **1987**. Deprotonation of the schiff-base of bacteriorhodopsin is obligate in light-induced proton pumping. *Biochemistry* 26:6107-6113.

96. Ohno, K., R. Govindjee, and T. G. Ebrey. **1983**. Blue-light effect on proton pumping by bacteriorhodopsin. *Biophysical Journal* 43:251-254.

97. Rothschild, K. J., P. Roepe, P. L. Ahl, T. N. Earnest, R. A. Bogomolni, S. K. Dasgupta, C. M. Mulliken, and J. Herzfeld. **1986**. Evidence for a tyrosine protonation change during the primary phototransition of bacteriorhodopsin at low-temperature. *Proceedings of the National Academy of Sciences of the United States of America* 83:347-351.

98. Stockburger, M., W. Klusmann, H. Gattermann, G. Massig, and R. Peters. **1979**. Photochemical cycle of bacteriorhodopsin studied by resonance Raman spectroscopy. *Biochemistry* 18:4886-4900.

99. Stoeckenius, W., and R. A. Bogomolni. **1982**. Bacteriorhodopsin and related pigments of halobacteria. *Annual Review of Biochemistry* 51:587-616.

100. Alshuth, T., and M. Stockburger. **1981**. Structural-changes in the retinal chromophore of bacteriorhodopsin studied by resonance Raman-spectroscopy. *Berichte Der Bunsen-Gesellschaft-Physical Chemistry Chemical Physics* 85:484-489.

101. Alshuth, T., and M. Stockburger. **1986**. Time-resolved resonance Raman studies on the photochemical cycle of bacteriorhodopsin. *Photochemistry and Photobiology* 43:55-66.

102. Braiman, M., and R. Mathies. **1982**. Resonance Raman-spectra of bacteriorhodopsins primary photoproduct - evidence for a distorted 13-cis retinal chromophore. *Proceedings of the National Academy of Sciences of the United States of America-Biological Sciences* 79:403-407.

103. Deng, H. **1985**. A detailed resonance Raman-study of the m412 intermediate in the bacteriorhodopsin photocycle. *Photochemistry and Photobiology* 41:467-470.

104. Hildebrandt, P., and M. Stockburger. **1984**. Role of water in bacteriorhodopsins chromophore - resonance Raman-study. *Biochemistry* 23:5539-5548.

105. Hsieh, C. L., M. Nagumo, M. Nicol, and M. A. Elsayed. **1981**. Picosecond and nanosecond resonance Raman studies of bacteriorhodopsin - do configurational changes of retinal occur in picoseconds. *Journal of Physical Chemistry* 85:2714-2717.

106. Mathies, R. **1982**. Resonance Raman-spectroscopy of rhodopsin and bacteriorhodopsin isotopic analogs. *Methods in Enzymology* 88:633-643.

107. Rothschild, K. J., P. V. Argade, T. N. Earnest, K. S. Huang, E. London, M. J. Liao, H. Bayley, H. G. Khorana, and J. Herzfeld. **1982**. The site of attachment of retinal in bacteriorhodopsin - a resonance Raman-study. *Journal of Biological Chemistry* 257:8592-8595.

108. Smith, S. O., J. Lugtenburg, and R. A. Mathies. **1985**. Determination of retinal chromophore structure in bacteriorhodopsin with resonance Raman-spectroscopy. *Journal of Membrane Biology* 85:95-109.

109. Terner, J., C. L. Hsieh, A. R. Burns, and M. A. El-Sayed. **1979**. Time-resolved resonance Raman spectroscopy of intermediates of bacteriorhodopsin: The bK590 intermediate. *Proceedings of the National Academy of Sciences of the United States of America* 76:3046-3050.

110. Degrip, W. J., D. Gray, J. Gillespie, P. H. M. Bovee, E. M. M. Vandenberg, J. Lugtenburg, and K. J. Rothschild. **1988**. Photoexcitation of rhodopsin - conformation changes in the chromophore, protein and associated lipids as determined by FTIR difference spectroscopy. *Photochemistry and Photobiology* 48:497-504.

111. Earnest, T. N., P. Roepe, M. S. Braiman, J. Gillespie, and K. J. Rothschild. **1986**. Orientation of the bacteriorhodopsin chromophore probed by polarized Fourier-transform infrared difference spectroscopy. *Biochemistry* 25:7793-7798.

112. Roepe, P., P. L. Ahl, S. K. Dasgupta, J. Herzfeld, and K. J. Rothschild. **1987**. Tyrosine and carboxyl protonation changes in the bacteriorhodopsin photocycle.1. M412 and L550 intermediates. *Biochemistry* 26:6696-6707.

113. Roepe, P., D. Gray, J. Lugtenburg, E. M. M. Vandenberg, J. Herzfeld, and K. J. Rothschild. **1988**. FTIR evidence for tryptophan perturbations during the bacteriorhodopsin photocycle. *Journal of the American Chemical Society* 110:7223-7224.

114. Roepe, P. D., P. L. Ahl, J. Herzfeld, J. Lugtenburg, and K. J. Rothschild. **1988**. Tyrosine protonation changes in bacteriorhodopsin - a Fourier-transform infrared study of bR548 and its primary photoproduct. *Journal of Biological Chemistry* 263:5110-5117.

115. Rothschild, K. J., W. A. Cantore, and H. Marrero. **1983**. Fourier-transform infrared difference spectra of intermediates in rhodopsin bleaching. *Science* 219:1333-1335.

116. Siebert, F., W. Mantele, and K. Gerwert. **1983**. Fourier-transform infrared-spectroscopy applied to rhodopsin - the problem of the protonation state of the retinylidene schiff-base re-investigated. *European Journal of Biochemistry* 136:119-127.

117. Varo, G., and J. K. Lanyi. **1991**. Kinetic and Spectroscopic Evidence for an Irreversible Step between Deprotonation and Reprotonation of the Schiff-Base in the Bacteriorhodopsin Photocycle. *Biochemistry* 30:5008-5015.

118. Zimanyi, L., Y. Cao, M. Chang, B. F. Ni, R. Needleman, and J. K. Lanyi. **1992**. The 2 consecutive M-substates in the photocycle of bacteriorhodopsin are affected specifically by the D85n and D96n residue replacements. *Photochemistry and Photobiology* 56:1049-1055.

119. Miller, A., and D. Oesterhelt. **1990**. Kinetic optimization of bacteriorhodopsin by aspartic acid-96 as an internal proton donor. *Biochimica Et Biophysica Acta* 1020:57-64.

120. Neutze, R., E. Pebay-Peyroula, K. Edman, A. Royant, J. Navarro, and E. M. Landau. **2002**. Bacteriorhodopsin: a high-resolution structural view of vectorial proton transport. *Biochimica Et Biophysica Acta-Biomembranes* 1565:144-167.

121. Birge, R. R., N. B. Gillespie, E. W. Izaguirre, A. Kusnetzow, A. F. Lawrence, D. Singh, Q. W. Song, E. Schmidt, J. A. Stuart, S. Seetharaman, and K. J. Wise. **1999**. Biomolecular electronics: Protein-based associative processors and volumetric memories. *Journal of Physical Chemistry B* 103:10746-10766.

122. Hampp, N. A. **2000**. Bacteriorhodopsin: mutating a biomaterial into an optoelectronic material. *Applied Microbiology and Biotechnology* 53:633-639.

123. Khodonov, A. A., O. V. Demina, L. V. Khitrina, A. D. Kaulen, P. Silfsten, S. Parkkinen, J. Parkkinen, and T. Jaaskelainen. **1997**. Modified bacteriorhodopsins as a basis for new optical devices. *Sensors and Actuators B-Chemical* 39:218-221.

124. Vsevolodov, N. N., and T. V. Dyukova. **1994**. Retinal-protein complexes as optoelectronic components. *Trends in Biotechnology* 12:81-88.

125. Oesterhelt, D. **1976**. Bacteriorhodopsin as a light-drive ion exchanger. *FEBS Letters* 64:20-22.

126. Miyasaka, T., and K. Koyama. **1992**. Rectified photocurrents from purple membrane Langmuir-Blodgett films at the electrode-electrolyte interface. *Thin Solid Films* 210-211:146-149.

127. Miyasaka, T., K. Koyama, and I. Itoh. **1992**. Quantum conversion and image detection by a bacteriorhodopsin-based artificial photoreceptor. *Science* 255:342-344.

128. Chen, Z. P., and R. R. Birge. **1993**. Protein-based artificial retinas. *Trends in Biotechnology* 11:292-300.

129. Rayfield George, W. **1994**. Photodiodes Based on Bacteriorhodopsin. In: Molecular and biomolecular electronics. R. R. Birge, editor (ed) (eds). American Chemical Society, Washington, DC. 561-575.

130. Haronian, D., and A. Lewis. **1991**. Elements of a unique bacteriorhodopsin neural network architecture. *Applied Optics* 30:597-608.

131. Boyer, A., M. Dery, P. Selles, C. Arbour, and F. Boucher. **1995**. Color discrimination by forward and reverse photocurrents in bacteriorhodopsin-based photosensor. *Biosensors & Bioelectronics* 10:415-422.

132. Trissl, H. W. **1990**. Photoelectric Measurements of Purple Membranes. *Photochemistry and Photobiology* 51:793-818.

133. Miyasaka, T., and K. Koyama. **1993**. Image sensing and processing by a bacteriorhodopsin-based artificial photoreceptor. *Applied Optics* 32:6371-6379.

134. Hong, F. T. **1997**. Molecular sensors based on the photoelectric effect of bacteriorhodopsin: Origin of differential responsivity. *Materials Science and Engineering: C* 4:267-285.

135. Birge, R. R. **1990**. Photophysics and molecular electronic applications of the rhodopsins. *Annual Review of Physical Chemistry* 41:683–733.

136. Birge, R. R. **1992**. Protein-based optical computing and memories. *Computer* 25:56-67.

137. Hampp, N., C. Brauchle, and D. Oesterhelt. **1992**. Mutated bacteriorhodopsins - competitive materials for optical information-processing. *Mrs Bulletin* 17:56-60.

138. Hampp, N., and A. Silber. **1996**. Functional dyes from nature: Potentials for technical applications. *Pure and Applied Chemistry* 68:1361-1366.

139. Oesterhelt, D., C. Brauchle, and N. Hampp. **1991**. Bacteriorhodopsin - a biological-material for information-processing. *Quarterly Reviews of Biophysics* 24:425-478.

140. Caplan, S. R., and G. Fischer. **1983**. Photovoltaic behavior of bacteriorhodopsin-loaded cation-exchange membranes. *Journal of Membrane Science* 16:391-405.

141. Thavasi, V., T. Lazarova, S. Filipek, M. Kolinski, E. Querol, A. Kumar, S. Ramakrishna, E. Padros, and V. Renugopalakrishnan. **2009**. Study on the feasibility of bacteriorhodopsin as bio-photosensitizer in excitonic solar cell: A first report. *Journal of Nanoscience and Nanotechnology* 9:1679-1687.

142. Lee, K.-H., and F. Boucher. **1997**. Further characterization of anesthetic-treated purple membranes by time-resolved photoelectric measurements. *Bulletin of Korean Chemistry Society* 18:103-105.

143. Maccioni, E., G. Radicchi, V. Erokhin, S. Paddeu, P. Facci, and C. Nicolini. **1996**. Bacteriorhodopsin thin film as a sensitive layer for an anaesthetic sensor. *Thin Solid Films* 284 898-900.

144. Pandey, P. C., S. Singh, B. Upadhyay, H. H. Weetall, and P. K. Chen. **1996**. Reversal in the kinetics of the M state decay of D96N bacteriorhodopsin: Probing of enzyme catalyzed reactions. *Sensors and Actuators B-Chemical* 36:470-474.

145. Tien, H. T. **1968**. Light-induced Phenomena in Black Lipid Membranes constituted from Photosynthetic Pigments. *Nature* 219:272-274.

146. Robertson, B., and E. P. Lukashev. **1995**. Rapid pH change due to bacteriorhodopsin measured with a tin-oxide electrode. *Biophysical Journal* 68:1507-1517.

147. Wang, J. P., L. Song, S. K. Yoo, and M. A. ElSayed. **1997**. A comparison of the photoelectric current responses resulting from the proton pumping process of bacteriorhodopsin under pulsed and CW laser excitations. *Journal of Physical Chemistry B* 101:10599-10604.

148. Wang, J. P., S. K. Yoo, L. Song, and M. A. ElSayed. **1997**. Molecular mechanism of the differential photoelectric response of bacteriorhodopsin. *Journal of Physical Chemistry B* 101:3420-3423.

149. Laitinen, H. A., and T. M. Hseu. **1979**. Chemically treated tin oxide electrodes responsive to pH and sulfide. *Analytical Chemistry* 51:1550-1552.

150. Fog, A., and R. P. Buck. **1984**. Electronic semiconducting oxides as pH sensors. *Sensors and Actuators* 5:137-146.

151. Koyama, K., N. Yamaguchi, and T. Miyasaka. **1994**. Antibody-mediated bacteriorhodopsin orientation for molecular device architectures. *Science* 265:762-765

152. Hong, F. T. **1997**. Molecular sensors based on the photoelectric effect of bacteriorhodopsin: Origin of differential responsivity (vol 4, pg 267, 1997). *Materials science & engineering c-biomimetic materials sensors and systems* 5:61-79.

153. Miyasaka, T., and K. Koyama. **1991**. Photoelectrochemical behavior of purple membrane Langmuir-Blodgett-films at the electrode-electrolyte interface. *Chemistry Letters*:1645-1648.

154. Hong, F. T., and M. Montal. **1979**. Bacteriorhodopsin in model membranes - new component of the displacement photocurrent in the microsecond time scale. *Biophysical Journal* 25:465-472.

155. Hong, F. T. **1980**. Bacteriorhodopsin model membrane - simple photo-bioenergetic system. *Journal of the Electrochemical Society* 127:C120-C120.

156. Hong, F. T. **1983**. Interpretation of the fast photoelectric signal from bacteriorhodopsin-containing membranes. *Abstracts of Papers of the American Chemical Society* 186:105-COLL.

157. Hong, F. T. **1986**. The bacteriorhodopsin model membrane system as a prototype molecular computing element. *BioSystems* 19:223-236.

158. Hong, F. T. **1994**. Electrochemical processes in membranes that contain bacteriorhodopsin. *Biomembrane electrochemistry* 235:531-560.

159. Hong, F. T. **1994**. Photovoltaic effects in biomembranes - reverse-engineering naturally-occurring molecular optoelectronic devices. *IEEE Engineering in Medicine and Biology Magazine* 13:75-93.

160. Michaile, S., and F. T. Hong. **1994**. Component analysis of the fast photoelectric signal from model bacteriorhodopsin membranes.1. effect of multilayer stacking and prolonged drying. *Bioelectrochemistry and Bioenergetics* 33:135-142.

161. Okajima, T. L., S. Michaile, L. E. McCoy, and F. T. Hong. **1994**. Component analysis of the fast photoelectric signal from model bacteriorhodopsin membranes.2. effect of fluorescamine treatment. *Bioelectrochemistry and Bioenergetics* 33:143-149.

162. Hong, F. H., and F. T. Hong. **1995**. Component analysis of the fast photoelectric signal from model bacteriorhodopsin membranes.4. a method for isolating the b2 component and the evidence for its polarity reversal at low ph. *Bioelectrochemistry and Bioenergetics* 37:91-99.

163. Hong, F. T. **1995**. Fundamentals of photoelectric effects in molecular electronic thin-film devices: applications to bacteriorhodopsin-based devices. *BioSystems* 35:117-121.

164. Hong, F. T. **1999**. Interfacial photochemistry of retinal proteins. *Progress in Surface Science* 62:1-237.

165. Hong, F. T. **1987**. Effect of local conditions on heterogeneous reactions in the bacteriorhodopsin membrane - an electrochemical view. *Journal of the Electrochemical Society* 134:3044-3052.

166. Saga, Y., T. Watanabe, K. Koyama, and T. Miyasaka. **1999**. Mechanism of photocurrent generation from bacteriorhodopsin on gold electrodes. *Journal of Physical Chemistry B* 103:234-238.

167. Chu, J. F., X. C. Li, and J. Tang. **2005**. Studies on poly(ethylenimine)/purple membrane multilayer films fabricated by layer-by-layer self-assembly. *Colloids and Surfaces a-Physicochemical and Engineering Aspects* 257-58:41-45.

168. Chu, J. F., X. C. Li, J. P. Zhang, and J. Tang. **2003**. Fabrication and photoelectric response of poly(allylamine hydrochloride)/PM thin films by layer-by-layer deposition technique. *Biochemical and Biophysical Research Communications* 305:116-121.

169. He, J. A., L. Samuelson, L. Li, J. Kumar, and S. K. Tripathy. **1998**. Photoelectric properties of oriented bacteriorhodopsin/polycation multilayers by electrostatic layer-by-layer assembly. *Journal of Physical Chemistry B* 102:7067-7072.

170. He, J. A., L. Samuelson, L. Li, J. Kumar, and S. K. Tripathy. **1998**. Oriented bacteriorhodopsin/polycation multilayers by electrostatic layer-by-layer assembly. *Langmuir* 14:1674-1679.

171. Furuno, T., K. Takimoto, T. Kouyama, A. Ikegami, and H. Sasabe. **1988**. Photovoltaic properties of purple membrane Langmuir-Blodgett films. *Thin Solid Films* 160:145-151.

172. Ikonen, M., J. Peltonen, E. Vuorimaa, and H. Lemmetyinen. **1992**. Study of photocycle and spectral properties of bacteriorhodopsin in Langmuir-Blodgett films. *Thin Solid Films* 213:277-284.

173. Weetall, H. H., and L. A. Samuelson. **1998**. Optical and electrical properties of bacteriorhodopsin Langmuir-Blodgett films. *Thin Solid Films* 312:306-312.

174. Keszthelyi, L. **1980**. Orientation of membrane fragments by electric field. *Biochim Biophys Acta.* 598:429-436.

175. Brizzolara, R. A. **1995**. A method for patterning purple membrane using self-assembled monolayers. *BioSystems* 35:137-140.

176. Brizzolara, R. A., and B. C. Beard. **1994**. Control of purple membrane adsorption to a glass-surface using self-assembled monolayers. *Journal of Vacuum Science & Technology a-Vacuum Surfaces and Films* 12:2981-2987.

177. Koyama, K., N. Yamaguchi, and T. Miyasaka. **1995**. Molecular organization of bacteriorhodopsin films in optoelectronic devices. *Advanced Materials* 7:590-594.

178. Weetall, H. H. **1994**. D96N mutant bacteriorhodopsin immobilized in sol-gel glass characterization. *Applied Biochemistry and Biotechnology* 49:241-256.

179. Wu, S. G., L. M. Ellerby, J. S. Cohan, B. Dunn, M. A. Elsayed, J. S. Valentine, and J. I. Zink. **1993**. Bacteriorhodopsin encapsulated in transparent sol-gel glass - a new biomaterial. *Chemistry of Materials* 5:115-120.

180. Chen, Z., K. G. Chittibabu, K. A. Marx, J. Kumar, S. K. Tripathy, L. A. Samuelson, J. A. Akkara, and D. L. Kaplan. **1994**. Photodynamic protein incorporated in conducting polymer and sol-gel matrices: Toward smart materials for information storage and processing. *Proceedings of SPIE* 218:105-115

181. Chen, Z., A. Lewis, H. Takei, and I. Nebenzahl. **1991**. Bacteriorhodopsin oriented in polyvinyl alcohol films as an erasable optical storage medium *Applied Optics* 30:5188-5196.

182. Lewis, A., Y. Albeck, Z. Lange, J. Benchowski, and G. Weizman. **1997**. Optical computation with negative light intensity with a plastic bacteriorhodopsin film. *Science* 275:1462-1464.

183. Petty, M. C. **1996**. Langmuir-Blodgett Films: An Introduction. Cambridge University Press, Cambridge.558

184. Wang, X. Y., Y. Zhang, C. E. Banks, Q. Y. Chen, and X. B. Ji. **2010**. Non-enzymatic amperometric glucose biosensor based on nickel hexacyanoferrate nanoparticle film modified electrodes. *Colloids and Surfaces B-Biointerfaces* 78:363-366.

185. He, J. A., L. Samuelson, L. Li, J. Kumar, and S. K. Tripathy. **1999**. Bacteriorhodopsin thin film assemblies - Immobilization, properties, and applications. *Advanced Materials* 11:435-446.

186. Hwang, S. B., J. I. Korenbrot, and W. Stoeckenius. **1977**. Structural and Spectroscopic Characteristics of Bacteriorhodopsin in Air-Water-Interface Films. *Journal of Membrane Biology* 36:115-135.

187. Hwang, S. B., J. I. Korenbrot, and W. Stoeckenius. **1977**. Proton Transport by Bacteriorhodopsin through an Interface Film. *Journal of Membrane Biology* 36:137-158.

188. Yamaguchi, N., Y. Jinbo, M. Arai, and K. Koyama. **1993**. Visualization of the Morphology of Purple Membrane Surfaces by Monoclonal-Antibody Techniques. *FEBS Letters* 324:287-292.

189. Kates, M., S. C. Kushwaha, G. D. Sprott, and P. Lester. **1982**. Lipids of purple membrane from extreme halophiles and of methanogenic bacteria. In: Methods in Enzymology. Academic Press. 98-111.

190. Jonas, R., Y. Koutalos, and T. G. Ebrey. **1990**. Purple Membrane - Surface-Charge Density and the Multiple Effect of Ph and Cations. *Photochemistry and Photobiology* 52:1163-1177.

191. Kimura, Y., M. Fujiwara, and A. Ikegami. **1984**. Anisotropic Electric Properties of Purple Membrane and Their Change During the Photoreaction Cycle. *Biophysical Journal* 45:615-625.

192. Decher, G., J. D. Hong, and J. Schmitt. **1992**. Buildup of Ultrathin Multilayer Films by a Self-Assembly Process.3. Consecutively Alternating Adsorption of Anionic and Cationic Polyelectrolytes on Charged Surfaces. *Thin Solid Films* 210:831-835.

193. Cheung, J. H., A. F. Fou, and M. F. Rubner. **1994**. Molecular self-assembly of conducting polymers. *Thin Solid Films* 224:985-989.

194. Ferreira, M., J. H. Cheung, and M. F. Rubner. **1994**. Molecular self-assembly of conjugated polyions: a new process for fabricating multilayer thin film heterostructures. *Thin Solid Films* 244:806-809.

195. Balasubramanian, S., X. G. Wang, H. C. Wang, K. Yang, J. Kumar, S. K. Tripathy, and L. Li. **1998**. Azochromophore-functionalized polyelectrolytes. 2. Acentric self-assembly through a layer-by-layer deposition process. *Chemistry of Materials* 10:1554-1560.

196. Ferreira, M., and M. F. Rubner. **1995**. Molecular-Level Processing of Conjugated Polymers.1. Layer-by-Layer Manipulation of Conjugated Polyions. *Macromolecules* 28:7107-7114.

197. Fou, A. C., O. Onitsuka, M. Ferreira, M. F. Rubner, and B. R. Hsieh. **1996**. Fabrication and properties of light-emitting diodes based on self-assembled multilayers of poly(phenylene vinylene). *Journal of Applied Physics* 79:7501-7509.

198. Watanabe, S., and S. L. Regen. **1994**. Dendrimers as Building-Blocks for Multilayer Construction. *Journal of the American Chemical Society* 116:8855-8856.

199. Fendler, J. H. **1996**. Self-assembled nanostructured materials. *Chemistry of Materials* 8:1616-1624.

200. Lvov, Y., K. Ariga, M. Onda, I. Ichinose, and T. Kunitake. **1997**. Alternate assembly of ordered multilayers of SiO2 and other nanoparticles and polyions. *Langmuir* 13:6195-6203.

201. Tripathy, S. K., H. Katagi, H. Kasai, S. Balasubramanian, H. Oshikiri, J. Kumar, H. Oikawa, S. Okada, and H. Nakanishi. **1998**. Self assembly of organic microcrystals 1: Electrostatic attachment of polydiacetylene microcrystals on a polyelectrolyte surface. *Japanese Journal of Applied Physics Part 2-Letters & Express Letters* 37:L343-L345.

202. Ariga, K., Y. Lvov, and T. Kunitake. **1997**. Assembling alternate dye-polyion molecular films by electrostatic layer-by-layer adsorption. *Journal of the American Chemical Society* 119:2224-2231.

203. Fang, M. M., D. M. Kaschak, A. C. Sutorik, and T. E. Mallouk. **1997**. A "mix and match" ionic-covalent strategy for self-assembly of inorganic multilayer films. *Journal of the American Chemical Society* 119:12184-12191.

204. Caruso, F., K. Niikura, D. N. Furlong, and Y. Okahata. **1997**. Assembly of alternating polyelectrolyte and protein multilayer films for immunosensing.2. *Langmuir* 13:3427-3433.

205. Lvov, Y., K. Ariga, I. Ichinose, and T. Kunitake. **1995**. Assembly of Multicomponent Protein Films by Means of Electrostatic Layer-by-Layer Adsorption. *Journal of the American Chemical Society* 117:6117-6123.

206. Lvov, Y., G. Decher, and G. Sukhorukov. **1993**. Assembly of Thin-Films by Means of Successive Deposition of Alternate Layers of DNA and Poly(Allylamine). *Macromolecules* 26:5396-5399.

207. Lvov, Y., H. Haas, G. Decher, H. Mohwald, A. Mikhailov, B. Mtchedlishvily, E. Morgunova, and B. Vainshtein. **1994**. Successive Deposition of Alternate Layers of Polyelectrolytes and a Charged Virus. *Langmuir* 10:4232-4236.

208. Onda, M., Y. Lvov, K. Ariga, and T. Kunitake. **1996**. Sequential actions of glucose oxidase and peroxidase in molecular films assembled by layer-by-layer alternate adsorption. *Biotechnology and Bioengineering* 51:163-167.

209. Alexiev, U., T. Marti, M. P. Heyn, H. G. Khorana, and P. Scherrer. **1994**. Surface-charge of bacteriorhodopsin detected with covalently bound pH indicators at selected extracellular and cytoplasmic sites. *Biochemistry* 33:298-306.

210. Min, J. H., H. G. Choi, J. W. Choi, W. H. Lee, and U. R. Kim. **1998**. Optimal fabrication condition of bacteriorhodopsin films by electrophoretic sedimentation technique. *Supramolecular Science* 5:687-690.

211. Min, J. H., H. G. Choi, J. W. Choi, W. H. Lee, and U. R. Kim. **1998**. Photocurrent of bacteriorhodopsin films deposited by electrophoretic method. *Thin Solid Films* 327:698-702.

212. Min, J. H., J. W. Choi, W. H. Lee, and U. R. Kim. **1998**. Photoreceptor consisting of spiropyran-bacteriorhodopsin films for photosignal enhancement. *Biosensors & Bioelectronics* 13:1151-1155.

213. Choi, H. G., J. Min, K. K. Han, Y. K. Kim, W. H. Lee, and J. W. Choi. **2000**. Optimal fabrication condition of bacteriorhodopsin thin films onto modified self-assembled monolayers. *Molecular Crystals and Liquid Crystals* 349:303-306.

214. Choi, H. G., J. H. Min, K. K. Han, J. W. Choi, and W. H. Lee. **2001**. Photoelectric conversion of bacteriorhodopsin films fabricated by self-assembly technique. *Synthetic Metals* 117:141-143.

215. Choi, H. G., J. H. Min, W. H. Lee, and J. W. Choi. **2002**. Adsorption behavior and photoelectric response characteristics of bacteriorhodopsin thin films fabricated by self-assembly technique. *Colloids and Surfaces B-Biointerfaces* 23:327-337.

216. Choi, H. G., W. C. Jung, J. H. Min, W. H. Lee, and J. W. Choi. **2001**. Color image detection by biomolecular photoreceptor using bacteriorhodopsin-based complex LB films. *Biosensors & Bioelectronics* 16:925-935.

217. Choi, H. G., J. H. Min, J. W. Choi, and W. H. Lee. **1998**. Molecular photoreceptor consisting of bacteriorhodopsin/flavin complex Langmuir-Blodgett films. *Biosensors & Bioelectronics* 13:1069-1075.

218. He, J.-A., L. Samuelson, L. Li, J. Kumar, and S. K. Tripathy. **1999**. Bacteriorhodopsin Thin-Film Assemblies - Immobilization, Properties, and Applications. *Advanced Materials* 11 435-446.

219. Jin, Y. D., N. Friedman, M. Sheves, and D. Cahen. **2007**. Bacteriorhodopsin-monolayer-based planar metal-insulator-metal junctions via biomimetic vesicle fusion: Preparation, characterization, and bio-optoelectronic characteristics. *Advanced Functional Materials* 17:1417-1428.

220. Jin, Y. D., N. Friedman, M. Sheves, T. He, and D. Cahen. **2006**. Bacteriorhodopsin (bR) as an electronic conduction medium: Current transport through bR-containing monolayers. *Proceedings of the National Academy of Sciences of the United States of America* 103:8601-8606.

221. Jin, Y. D., N. Friedman, D. Cahen, and M. Sheves. **2006**. Chemically induced enhancement of the opto-electronic response of Halobacterium purple membrane monolayer. *Chemical Communications*:1310-1312.

222. Horn, C., and C. Steinem. **2005**. Photocurrents generated by bacteriorhodopsin adsorbed on nano-black lipid membranes. *Biophysical Journal* 89:1046-1054.

223. Bromley, K. M., A. J. Patil, A. M. Seddon, P. Booth, and S. Mann. **2007**. Bio-functional mesolamellar nanocomposites based on inorganic/polymer intercalation in purple membrane (bacteriorhodopsin) films. *Advanced Materials* 19:2433-2438.

224. Twellmeyer, J., A. Wende, J. Wolfertz, F. Pfeiffer, M. Panhuysen, A. Zaigler, J. Soppa, G. Welzl, and D. Oesterhelt. **2007**. Microarray Analysis in the Archaeon Halobacterium salinarum Strain R1. *PLoS one* 2:e1064.

225. Nomura, S., N. Kajimura, K. Matoba, T. Miyata, R. Ortenberg, M. Mevarech, H. Kamikubo, M. Kataoka, and Y. Harada. **1999**. Ordered structure formation of bacteriorhodopsin-hDHFR in a plasma membrane. *Langmuir* 15:214-220.

226. Oesterhelt, D., and W. Stoeckenius. **1974**. Isolation of the cell membrane of *Halobacterium halobium* and its fractionation into red and purple membrane. In: Methods in Enzymology. S. F. a. L. Packer, editor (ed) (eds). Academic Press, San Diego, CA. 667-678.

227. He, J. A., L. Samuelson, L. Li, J. Kumar, and S. K. Tripathy. **1998**. Oriented bacteriorhodopsin (nanosized PM fragments) polycation films by electrostatic layer-by-layer assembly. *Abstracts of Papers of the American Chemical Society* 216:U312-U313.

228. Chu, J. F., X. C. Li, and J. Tang. **2005**. Studies on poly(ethylenimine)/purple membrane multilayer films fabricated by layer-by-layer self-assembly. *Colloids and Surfaces, A: Physicochemical and Engineering Aspects* 257-58:41-45.

229. Cai, D., K. Kempa, Z. Ren, D. Carnahan, and T. C. Chiles. **2008**. Nanospearing – Biomolecule Delivery and Its Biocompatibility In: Nanomaterials for Application in Medicine and Biology. M. Giersig, and G. B. Khomutov, editor editors (eds). Springer Netherlands, Dordrecht. 81.

230. Mezo, G., J. Remenyi, J. Kajtar, K. Barna, D. Gaal, and F. Hudecz. **2000**. Synthesis and conformational studies of poly(L-lysine) based branched polypeptides with Ser and Glu/Leu in the side chains. *Journal of Controlled Release* 63:81-95.

231. Picart, C., P. Lavalle, P. Hubert, F. J. G. Cuisinier, G. Decher, P. Schaaf, and J. C. Voegel. **2001**. Buildup mechanism for poly(L-lysine)/hyaluronic acid films onto a solid surface. *Langmuir* 17:7414-7424.

232. Khademhosseini, A., K. Y. Suh, J. M. Yang, G. Eng, J. Yeh, S. Levenberg, and R. Langer. **2004**. Layer-by-layer deposition of hyaluronic acid and poly-L-lysine for patterned cell co-cultures. *Biomaterials* 25:3583-3592.

233. Peng, H., Y. Xiao, X. L. Mao, L. Chen, R. Crawford, and A. K. Whittaker. **2009**. Amphiphilic Triblock Copolymers of Methoxy-poly(ethylene glycol)-b-poly(L-lactide)-b-poly(L-lysine) for Enhancement of Osteoblast Attachment and Growth. *Biomacromolecules* 10:95-104.

234. Zauner, W., M. Ogris, and E. Wagner. **1998**. Polylysine-based transfection systems utilizing receptor-mediated delivery. *Advanced Drug Delivery Reviews* 30:97-113.

235. Smith, L. C., J. Duguid, M. S. Wadhwa, M. J. Logan, C. H. Tung, V. Edwards, and J. T. Sparrow. **1998**. Synthetic peptide-based DNA complexes for nonviral gene delivery. *Advanced Drug Delivery Reviews* 30:115-131.

236. Orive, G., S. K. Tam, J. L. Pedraz, and J. P. Halle. **2006**. Biocompatibility of alginate-poly-L-lysine microcapsules for cell therapy. *Biomaterials* 27:3691-3700.

237. Leblond, F. A., G. Simard, N. Henley, B. Rocheleau, P. M. Huet, and J. P. Halle. **1999**. Studies on smaller (similar to 315 mu M) microcapsules: IV. Feasibility and safety of intrahepatic implantations of small alginate poly-L-lysine microcapsules. *Cell Transplantation* 8:327-337.

238. Wu, Q., W. Ma, R. Shi, B. Zhang, X. Mao, and W. Zheng. **2005**. An activated GOPS-poly-L-lysine-coated glass surface for the immobilization of 60mer oligonucleotides. *Engineering in Life Sciences* 5:466-470.

239. Kusnezow, W., and J. D. Hoheisel. **2003**. Solid supports for microarray immunoassays. *Journal of Molecular Recognition* 16:165-176.

240. Mjahed, H., C. Porcel, B. Senger, A. Chassepot, P. Netter, P. Gillet, G. Decher, J. C. Voegel, P. Schaaf, N. Benkirane-Jessel, and F. Boulmedais. **2008**. Micro-stratified architectures based on successive stacking of alginate gel layers and poly(L-lysine)-hyaluronic acid multilayer films aimed at tissue engineering. *Soft Matter* 4:1422-1429.

241. Crompton, K. E., J. D. Goud, R. V. Bellamkonda, T. R. Gengenbach, D. I. Finkelstein, M. K. Horne, and J. S. Forsythe. **2007**. Polylysine-functionalised thermoresponsive chitosan hydrogel for neural tissue engineering. *Biomaterials* 28:441-449.

242. Shi, X. Y., R. J. Sanedrin, and F. M. Zhou. **2002**. Structural characterization of multilayered DNA and polylysine composite films: Influence of ionic strength of DNA solutions on the extent of DNA incorporation. *Journal of Physical Chemistry B* 106:1173-1180.

243. Gergely, C., S. Bahi, B. Szalontai, H. Flores, P. Schaaf, J. C. Voegel, and F. J. G. Cuisinier. **2004**. Human serum albumin self-assembly on weak polyelectrolyte multilayer films structurally modified by pH changes. *Langmuir* 20:5575-5582.

244. Zhao, W. H., B. Zheng, and D. T. Haynie. **2006**. A molecular dynamics study of the physical basis of stability of polypeptide multilayer nanofilms. *Langmuir* 22:6668-6675.

245. Ji, J., J. H. Fu, and J. C. Shen. **2006**. Fabrication of a superhydrophobic surface from the amplified exponential growth of a multilayer. *Advanced Materials* 18:1441-1444.

246. Shiratori, S. S., and M. F. Rubner. **2000**. pH-dependent thickness behavior of sequentially adsorbed layers of weak polyelectrolytes. *Macromolecules* 33:4213-4219.

247. Matsumura, H., F. Mori, K. Kawahara, C. Obata, and K. Furusawa. **1994**. Effect of amino-acids, polypeptides and proteins on electrophoretic mobilities of phospholipid liposomes. *Colloids and Surfaces, A: Physicochemical and Engineering Aspects* 92:87-93.

248. Cui, X. Q., C. M. Li, H. F. Bao, X. T. Zheng, and Z. S. Lu. **2008**. In situ fabrication of silver nanoarrays in hyaluronan/PDDA layer-by-layer assembled structure. *Journal of Colloid and Interface Science* 327:459-465.

249. Hu, W. H., C. M. Li, X. Q. Cui, H. Dong, and Q. Zhou. **2007**. In situ studies of protein adsorptions on poly(pyrrole-co-pyrrole propylic acid) film by electrochemical surface plasmon resonance. *Langmuir* 23:2761-2767.

250. Lu, Z. S., C. M. Li, Q. Zhou, Q. L. Bao, and X. Q. Cui. **2007**. Covalently linked DNA/protein multilayered film for controlled DNA release. *Journal of Colloid and Interface Science* 314:80-88.

251. Yuan, W. Y., H. Dong, C. M. Li, X. Q. Cui, L. Yu, Z. S. Lu, and Q. Zhou. **2007**. pH-Controlled construction of chitosan/alginate multilayer film: Characterization and application for antibody immobilization. *Langmuir* 23:13046-13052.

252. Liedberg, B., I. Lundström, and E. Stenberg. **1993**. Principles of biosensing with an extended coupling matrix and surface plasmon resonance. *Sensors and Actuators B: Chemical* 11:63-72.

253. Debruijn, H. E., B. S. F. Altenburg, R. P. H. Kooyman, and J. Greve. **1991**. Determination of thickness and dielectric-constant of thin transparent dielectric layers using surface-plasmon resonance. *Optics Communications* 82:425-432.

254. Yu, J. C. C., and E. P. C. Lai. **2004**. Polypyrrole film on miniaturized surface plasmon resonance sensor for ochratoxin A detection. *Synthetic Metals* 143:253-258.

255. Zhang, C. P., Q. W. Song, C. Y. Ku, R. B. Gross, and R. R. Birge. **1994**. Determination of the refractive-index of a bacteriorhodopsin film. *Optics Letters* 19:1409-1411.

256. Yu, Y., Y. Y. Zhuang, and Z. H. Wang. **2001**. Adsorption of water-soluble dye onto functionalized resin. *Journal of Colloid and Interface Science* 242:288-293.

257. Ogawa, Y., Y. Arikawa, T. Kida, and M. Akashi. **2008**. Fabrication of novel layer-by-layer assembly films composed of poly(lactic acid) and polylysine through cation-dipole interactions. *Langmuir* 24:8606-8609.

258. Koyama, K., N. Yamaguchi, and T. Miyasaka. **1995**. Molecular organization of bacterio-rhodopsin films in optoelectronic devices. *Advanced Materials* 7:590-594.

259. Li, R., X. Cui, W. Hu, Z. Lu, and C. M. Li. **2010**. Fabrication of Oriented Poly-L-lysine/Bacteriorhodopsin-embedded Purple Membrane Multilayer Structure for Enhanced Photoelectric Response. *Journal of Colloid and Interface Science* in press.

260. Bao, S. J., C. M. Li, J. F. Zang, X. Q. Cui, Y. Qiao, and J. Guo. **2008**. New nanostructured TiO2 for direct electrochemistry and glucose sensor applications. *Advanced Functional Materials* 18:591-599.

261. Qiao, Y., C. M. Li, S. J. Bao, Z. S. Lu, and Y. H. Hong. **2008**. Direct electrochemistry and electrocatalytic mechanism of evolved Escherichia coli cells in microbial fuel cells. *Chemical Communications*:1290-1292.

262. Bromley, K. M., A. J. Patil, A. M. Seddon, P. Booth, and S. Mann. **2007**. Bio-functional mesolamellar nanocomposites based on inorganic/polymer intercalation in purple membrane (bacteriorhodopsin) films. *Advanced Materials* 19:2433-2438.

263. Li, R., C. M. Li, H. F. Bao, Q. L. Bao, and V. S. Lee. **2007**. Stationary current generated from photocycle of a hybrid bacteriorhodopsin/quantum dot bionanosystem. *Applied Physics Letters* 91:223901.

264. Yang, J. Y., Y. L. Li, Y. Q. Huang, J. Y. Liang, and P. K. Shen. **2008**. Dynamic conducting effect of WO3/PFSA membranes on the performance of proton exchange membrane fuel cells. *Journal of Power Sources* 177:56-60.

265. Habazaki, H., Y. Hayashi, and H. Konno. **2002**. Characterization of electrodeposited WO3 films and its application to electrochemical wastewater treatment. *Electrochimica Acta* 47:4181-4188.

266. Klug, H., and L. Alexander. **1962**. X-ray diffraction procedure. Wiley, New York.491

267. Li, Y. M., M. Hibino, M. Miyayania, and T. Kudo. **2000**. Proton conductivity of tungsten trioxide hydrates at intermediate temperature. *Solid State Ionics* 134:271-279.

268. Conner, W. C., and J. L. Falconer. **1995**. Spillover in heterogeneous catalysis. *Chemical Reviews* 95:759-788.

269. Sermon, P. A., and G. C. Bond. **1976**. Studies of hydrogen spillover.1. Study of rate, extent and products of hydrogen spillover from platinum to trioxides of tungsten and molybdenum. *Journal of the Chemical Society-Faraday Transactions I* 72:730-744.

270. Weidlich, O., B. Schalt, N. Friedman, M. Sheves, J. K. Lanyi, L. S. Brown, and F. Siebert. **1996**. Steric interaction between the 9-methyl group of the retinal and tryptophan 182 controls 13-cis to all-trans reisomerization and proton uptake in the bacteriorhodopsin photocycle. *Biochemistry* 35:10807-10814.

271. Doig, S. J., P. J. Reid, and R. A. Mathies. **1991**. Picosecond Time-Resolved Resonance Raman-Spectroscopy of Bacteriorhodopsin-J, Bacterlorhodopsin-K, Bacterlorhodopsin-Kl Intermediates. *Journal of Physical Chemistry* 95:6372-6379.

272. Metz, G., F. Siebert, and M. Engelhard. **1992**. Asp(85) Is the Only Internal Aspartic-Acid That Gets Protonated in the M-Intermediate and the Purple-to-Blue Transition of Bacteriorhodopsin - a Solid-State C-13 Cp-Mas Nmr Investigation. *FEBS Letters* 303:237-241.

273. Edman, K., P. Nollert, A. Royant, H. Belrhali, E. Pebay-Peyroula, J. Hajdu, R. Neutze, and E. M. Landau. **1999**. High-resolution X-ray structure of an early intermediate in the bacteriorhodopsin photocycle. *Nature* 401:822-826.

274. Sass, H. J., G. Buldt, R. Gessenich, D. Hehn, D. Neff, R. Schlesinger, J. Berendzen, and P. Ormos. **2000**. Structural alterations for proton translocation in the M state of wild-type bacteriorhodopsin. *Nature* 406:649-653.

275. Schertler, G. F. X., R. Lozier, H. Michel, and D. Oesterhelt. **1991**. Chromophore Motion During the Bacteriorhodopsin Photocycle - Polarized Absorption-Spectroscopy of Bacteriorhodopsin and Its M-State in Bacteriorhodopsin Crystals. *EMBO Journal* 10:2353-2361.

276. Muller, K. H., H. J. Butt, E. Bamberg, K. Fendler, B. Hess, F. Siebert, and M. Engelhard. **1991**. The Reaction Cycle of Bacteriorhodopsin - an Analysis Using Visible Absorption, Photocurrent and Infrared Techniques. *European biophysics journal* 19:241-251.

277. Tittor, J., U. Schweiger, D. Oesterhelt, and E. Bamberg. **1994**. Inversion of Proton Translocation in Bacteriorhodopsin Mutants D85n, D85t, and D85,96n. *Biophysical Journal* 67:1682-1690.

278. Bao, H. F., E. K. Wang, and S. J. Dong. **2006**. One-pot synthesis of CdTe nanocrystals and shape control of luminescent CdTe-cystine nanocomposites. *Small* 2:476-480.

279. Nagy, K. **1978**. Photoelectric activity of dried, oriented layers of purple membrane from halobacterium halobium. *Biochemical and Biophysical Research Communications* 85:383-390.

280. Hess, B. **1976**. Technology of biomolecular design, with experimets on light cotrol of the photochemical cycle in *Halobacterium halobium*. *FEBS Letters* 64:26-28.

281. Oesterhelt, D., and B. Hess. **1973**. Reversible Photolysis of the Purple Complex in the Purple Membrane of *Halobacterium halobium. European Journal of Biochemistry* 37:316-326.

282. Subramaniam, S., I. Lindahl, P. Bullough, A. R. Faruqi, J. Tittor, D. Oesterhelt, L. Brown, J. Lanyi, and R. Henderson. **1999**. Protein conformational changes in the bacteriorhodopsin photocycle. *Journal of Molecular Biology* 287:145-161.

283. Dancsházy, Z., L. A. Drachev, P. Ormos, K. Nagy, and V. P. Skulachev. **1978**. Kinetics of the blue light-induced inhibition of photoelectric activity of bacteriorhodopsin. *FEBS Letters* 96:59-63.

284. Dancsházy, Z., and Z. Tokaji. **2000**. Blue light regeneration of bacteriorhodopsin bleached by continuous light. *FEBS Letters* 476:171-173.

285. Dickopf, S., and M. P. Heyn. **1997**. Evidence for the first phase of the reprotonation switch of bacteriorhodopsin from time-resolved photovoltage and flash photolysis experiments on the photoreversal of the M-intermediate. *Biophysical Journal* 73:3171-3181.

286. Yelleswarapu, C. S., P. F. Wu, S. R. Kothapalli, and D. Rao. **2006**. Nonlinear optical image processing with bacteriorhodopsin polymer films. *Molecular Crystals and Liquid Crystals* 446:273-294.

287. Petrak, M. R., and F. T. Hong. **1998**. Component analysis of the fast photoelectric signal from model bacteriorhodopsin membranes: V. Effects of chloride ion transport blockers and divalent cation chelators. *Bioelectrochemistry and Bioenergetics* 45:193-201.

288. Uehara, K., K. Kawai, and T. Kouyama. **1993**. Photoelectric response of oriented purple membrane electrodeposited onto poly(vinyl alcohol) film. *Thin Solid Films* 232:271-277.

289. He, T., N. Friedman, D. Cahen, and M. Sheves. **2005**. Bacteriorhodopsin monolayers for optoelectronics: Orientation and photoelectric response on solid supports. *Advanced Materials* 17:1023-1027.

290. Huang, Y. H., G. Siganakis, M. G. Moharam, and S. T. Wu. **2004**. Broadband optical limiter based on nonlinear photoinduced anisotropy in bacteriorhodopsin film. *Applied Physics Letters* 85:5445-5447.

291. Schulten, K., and P. Tavan. **1978**. A mechanism for the light-driven proton pump of Halobacterium halobium. *Nature* 272:85-86.

292. Hu, J. T., L. S. Li, W. D. Yang, L. Manna, L. W. Wang, and A. P. Alivisatos. **2001**. Linearly polarized emission from colloidal semiconductor quantum rods. *Science* 292:2060-2063.

293. Peng, X. G., L. Manna, W. D. Yang, J. Wickham, E. Scher, A. Kadavanich, and A. P. Alivisatos. **2000**. Shape control of CdSe nanocrystals. *Nature* 404:59-61.

294. Kazes, M., D. Y. Lewis, Y. Ebenstein, T. Mokari, and U. Banin. **2002**. Lasing from semiconductor quantum rods in a cylindrical microcavity. *Advanced Materials* 14:317-321.

295. Pui, T.-S., A. Agarwal, F. Ye, Z.-Q. Tou, Y. Huang, and P. Chen. **2009**. Ultra-sensitive detection of adipocytokines with CMOS-compatible silicon nanowire arrays. *Nanoscale* 1:159-163.

296. Law, M., L. E. Greene, J. C. Johnson, R. Saykally, and P. D. Yang. **2005**. Nanowire dye-sensitized solar cells. *Nature Materials* 4:455-459.

297. Stern, E., J. F. Klemic, D. A. Routenberg, P. N. Wyrembak, D. B. Turner-Evans, A. D. Hamilton, D. A. LaVan, T. M. Fahmy, and M. A. Reed. **2007**. Label-free immunodetection with CMOS-compatible semiconducting nanowires. *Nature* 445:519-522.

298. Huang, M. H., S. Mao, H. Feick, H. Q. Yan, Y. Y. Wu, H. Kind, E. Weber, R. Russo, and P. D. Yang. **2001**. Room-temperature ultraviolet nanowire nanolasers. *Science* 292:1897-1899.

299. Chen, X., and S. S. Mao. **2007**. Titanium dioxide nanomaterials: Synthesis, properties, modifications, and applications. *Chemical Reviews* 107:2891-2959.

300. Bao, S. J., Q. L. Bao, C. M. Li, and Z. L. Dong. **2007**. Novel porous anatase TiO2 nanorods and their high lithium electroactivity. *Electrochemistry Communications* 9:1233-1238.

301. Qiao, Y., S. J. Bao, C. M. Li, X. Q. Cui, Z. S. Lu, and J. Guo. **2008**. Nanostructured polyanifine/titanium dioxide composite anode for microbial fuel cells. *Acs Nano* 2:113-119.

302. Baik, J. M., M. H. Kim, C. Larson, X. H. Chen, S. J. Guo, A. M. Wodtke, and M. Moskovits. **2008**. High-yield TiO2 nanowire synthesis and single nanowire field-effect transistor fabrication. *Applied Physics Letters* 92.

303. Lee, Y. H., J. M. Yoo, D. H. Park, D. H. Kim, and B. K. Ju. **2005**. Co-doped TiO2 nanowire electric field-effect transistors fabricated by suspended molecular template method. *Applied Physics Letters* 86.

304. Bogomolni, R. A., S. B. Hwang, Y. W. Tseng, G. I. King, and W. Stoeckenius. **1977**. Orientation of bacteriorhodopsin transition dipole. *Biophysical Journal* 17:A98-A98.

305. Xu, D., C. Martin, and K. Schulten. **1996**. Molecular dynamics study of early picosecond events in the bacteriorhodopsin photocycle: Dielectric response, vibrational cooling and the J, K intermediates. *Biophysical Journal* 70:453-460.

306. Bradley, K., A. Davis, J. C. P. Gabriel, and G. Gruner. **2005**. Integration of cell membranes and nanotube transistors. *Nano Letters* 5:841-845.

307. Ermolina, I., A. Lewis, and Y. Feldman. **2003**. Dielectric Properties of the bR Membrane. *The Journal of Physical Chemistry B* 107:14537-14544.

308. Wang, G., and D. Porschke. **2003**. Dipole Reversal in Bacteriorhodopsin and Separation of Dipole Components. *The Journal of Physical Chemistry B* 107:4632-4638.

309. Chen, J. S., C. M. Li, W. W. Zhou, Q. Y. Yan, L. A. Archer, and X. W. Lou. **2009**. One-pot formation of SnO2 hollow nanospheres and -Fe2O3@SnO2 nanorattles with large void space and their lithium storage properties. *Nanoscale* 1:280-285.

310. Chu, Y. M., C. C. Lin, J. J. Wu, and H. C. Chang. **2008**. A rapid and simple method for parallel the TiO2 nanowires and the aligned-substrate surface: Characterization of nanowires. In: 3rd IEEE International Conference of Nano/Micro Engineered and Molecular Systems, Sanya, PEOPLES R CHINA. 539-542.

311. Cai, Q. J., M. B. Chan-Park, Z. S. Lu, C. M. Li, and B. S. Ong. **2008**. Bottom-Contact Poly(3,3 '''-didodecylquaterthiophene) Thin-Film Transistors with Gold Source-Drain Electrodes Modified by Alkanethiol Monolayers. *Langmuir* 24:11889-11894.

312. Gan, Y., Q. J. Cai, C. M. Li, H. Bin Yang, Z. S. Lu, C. Gong, and M. B. Chan-Park. **2009**. Solution-Prepared Hybrid-Nanoparticle Dielectrics for High-Performance Low-Voltage Thin-Film Transistors. *Acs Applied Materials & Interfaces* 1:2230-2236.

313. Suzuki, S., T. Yamanashi, S. Tazawa, O. Kurosawa, and M. Washizu. **1998**. Quantitative analysis of DNA orientation in stationary AC electric fields using fluorescence anisotropy. *IEEE Transactions on Industry Applications* 34:75-83.

314. Smith, P. A., C. D. Nordquist, T. N. Jackson, T. S. Mayer, B. R. Martin, J. Mbindyo, and T. E. Mallouk. **2000**. Electric-field assisted assembly and alignment of metallic nanowires. *Applied Physics Letters* 77:1399-1401.

315. Krupke, R., F. Hennrich, H. von Lohneysen, and M. M. Kappes. **2003**. Separation of metallic from semiconducting single-walled carbon nanotubes. *Science* 301:344-347.

316. Krupke, R., F. Hennrich, H. B. Weber, D. Beckmann, O. Hampe, S. Malik, M. M. Kappes, and H. V. Lohneysen. **2003**. Contacting single bundles of carbon nanotubes with alternating electric fields. *Applied Physics a-Materials Science & Processing* 76:397-400.

317. Bezryadin, A., C. Dekker, and G. Schmid. **1997**. Electrostatic trapping of single conducting nanoparticles between nanoelectrodes. *Applied Physics Letters* 71:1273-1275.

318. Harnack, O., C. Pacholski, H. Weller, A. Yasuda, and J. M. Wessels. **2003**. Rectifying behavior of electrically aligned ZnO nanorods. *Nano Letters* 3:1097-1101.

319. Liu, H. M., W. S. Yang, Y. Ma, Y. Cao, J. N. Yao, J. Zhang, and T. D. Hu. **2003**. Synthesis and characterization of titania prepared by using a photoassisted sol-gel method. *Langmuir* 19:3001-3005.

320. Park, J. S., and W. Choi. **2004**. Enhanced remote photocatalytic oxidation on surface-fluorinated TiO2. *Langmuir* 20:11523-11527.

Publications

1. **Li, R.**, C. M. Li*, H. F. Bao, Q. L. Bao, and V. S. Lee. **2007**. Stationary current generated from photocycle of a hybrid bacteriorhodopsin/quantum dot bionanosystem. *Appl. Phys. Lett.* **91**:223901 (selected for the December 1, 2007 issue of *Virtual Journal of Biological Physics Research* which is published by the American Physical Society and the American Institute of Physics and can be accessed at www.vjbio.org).

2. **Li, R.**, F. P. Hu, Q. L. Bao, S. J. Bao, Y. Qiao, S. C. Yu, J. Guo. and C. M. Li*. **2010**. Enhancement of photoelectric response of bacteriorhodopsin by multilayered $WO_3 \cdot H_2O$ nanocrystals/PVA membrane. *Chemical Communications*, **46**(5): 689 - 691(news item about this article is published in the magazine Highlights in Chemical Science which can be accessed at www.rsc.org/highlightschemsci since Feb. 23, 2010).

3. **Li, R.**, X. Q. Cui, W. H. Hu, Z. S. Lu and C. M. Li*. **2010**. Fabrication of Oriented Poly-L-lysine/ Bacteriorhodopsin-embedded Purple Membrane Multilayer Structure for Enhanced Photoelectric Response. *Journal of Colloid and Interface Science,* **344**(1): 150-157.

4. **Li, R.**, Y. Gan, Q. L. Song, Z. H. Zhu, J. Shi, H. Yang, W. Wang, P. Chen and C. M. Li∗. **2010**. Bidirectional Mediation of TiO_2 Nanowires Field Effect Transistor by Dipole Moment from Purple Membrane. *Nanoscale*, **2**(8): 1474-1479.

5. **Li, R.**, C. M. Li*, H. F. Bao, F. P. Hu, and Q. L. Bao. **2008**. Different photoelectric responses generated from integrated bionanosystems based on purple membrane. *Proceedings of the 15th Regional Symposium on Chemical Engineering in conjunction with the 22nd Symposium of Malaysian -hemical Engineers*, volume II, pp. 107-112, Kuala Lumpur, Malaysia, 2-3 December 2008.